



## Theoretical and Experimental Investigation of Transient Temperature Distribution in Friction Stir Welding of AA 7020-T53

**Dr. Muhsin Jaber Jweeg**Nahrain University/College of Engineering  
Mechanical engineering department  
[muhsinnah\\_eng@nahrainuniv.edu.iq](mailto:muhsinnah_eng@nahrainuniv.edu.iq)**Dr. Moneer Hameed Tolephih**Foundation of technical education  
Technical College-Baghdad  
[monerht@yahoo.com](mailto:monerht@yahoo.com)**Muhammed Abdul-Sattar**Nahrain University/College of Engineering  
Mechanical engineering department  
[m1976sjn@yahoo.com](mailto:m1976sjn@yahoo.com)**Abstract:**

Finite element modeling of transient temperature distribution is used to understand physical phenomena occurring during the dwell (penetration) phase and moving of welding tool in friction stir welding (FSW) of 5mm plate made of 7020-T53 aluminum alloy at 1400rpm and 40mm/min.

Thermocouples are used in locations near to the pin and under shoulder surface to study the welding tool penetration in the workpiece in advance and retreat sides along welding line in three positions (penetrate (start welding), mid, pullout (end welding)).

Numerical results of ANSYS 12.0 package are compared to experimental data including axial load measurements at different tool rotational speeds (710rpm, 900rpm, 1120rpm and 1400rpm). Based on the experimental records of transient temperature at several specific locations of thermocouples during the friction stir welding process the temperatures are higher on the advancing side ( $629.2^{\circ}\text{K}$ ) than the retreating side ( $605^{\circ}\text{K}$ ) along welding line and temperature in the top of workpiece under tool shoulder is higher ( $645^{\circ}\text{K}$ ) than bottom ( $635.79^{\circ}\text{K}$ ). The results of the simulation are in good agreement with that of experimental results. The peak temperature obtained was 70% of the melting point of parent metal.

**الخلاصة**

موديل رياضي بطريقة العناصر المحددة استخدم لتمثيل التوزيع الحراري العابر وفهم الظواهر الفيزيائية التي تحدث اثناء عملية الغرز (دخول) و حركة اداة اللحام في عملية اللحام بطريقة الخلط الاحتكاك لصفيحة من سبيكة الالمونيوم (7020-T53) بسمك 5 ملم عند (سرعة دورانية 1400rpm ، سرعة خطية 40mm/min). النتائج النظرية باستخدام ANSYS 12.0 (قورنت مع النتائج العملية متضمنة قياس الحمل العمودي عملياً لعدة سرع دورانية (710rpm, 900rpm, 1120rpm, 1400rpm).

في هذا العمل تم استخدام مزدوجات حرارية وضعت في موقع قريبة من رأس اداة اللحام (pin) وتحت (shoulder) لغرض دراسة عملية دخول وكيفية توزيع الحرارة على جانبي وتحت اداة اللحام وثلاث مناطق من الصفيحة (منطقة الغرز، ووسط، نهاية اللحام (خروج اداة اللحام)).

بالاعتماد على النتائج العملية المسجلة للتوزيع الحراري العابر عند مواقع مختلفة للمزدوجات الحرارية على جانبي اداة اللحام خلال عملية اللحام الخلط الاحتكاك وجد ان درجة الحرارة في منطقة ( $629.2^{\circ}\text{K}$  advance) هي اعلى من منطقة ( $605^{\circ}\text{K}$  retreat) على طول خط اللحام كما ان الحرارة عند سطح العينة تحت (shoulder) هي اعلى من اسفل العينة ( $635.79^{\circ}\text{K}$ )، اقصى حرارة سجلت كانت  $70\%$  من درجة الانصهار للسبائك الالمونيوم. نتائج الموديل الرياضي كانت متوافقة مع النتائج العملية .

**Keywords** Friction stir welding, Transient temperature, Temperature distribution, FE-simulation, 7020-T53 Aluminum alloy.

## Introduction:

Friction stir welding (FSW) is a relatively contemporary solid-state process introduced back in 1991 by TWI [1]. Based on its advantages, this welding procedure has become more popular recently. Some of these advantages include however, not limited to the following: low shrinkage and distortion, desired mechanical properties, producing less fumes, and ability in welding of alloys otherwise difficult with other melting procedures, alloys such as 2xxx and 7xxx series of aluminum [2]. It could safely be stated that most if not all abovementioned advantages are due to the fact that the generated heat produced by the process remains below melting temperature of the metal. Consequently, undesired parameters resulted from typical welding processes will not materialize. Some of these parameters are solidification cracking, liquidation cracking, and porosity.

Friction stir welding fundamental is depicted in Fig. 1. In this procedure, two plates are firmly clamped on the backing plate. Spinning tool slowly lowers into the connecting plates until tool shoulder touches the upper surfaces of the plates. While spinning, the moving displaces forward on the piece and this causes heat due to the friction between them. The tool starts to move after pausing for warm-up of the plates. While forward moving, the tool forges the materials by spinning and as result, a strong connection will take place between the plates. In some cases, in order to provide more effective forge due to better string of the materials, the tool is somewhat angled from its vertical position.

There are many variations in the process of FSW that makes it difficult to conduct a thrill investigation. Major, independent variables are: rotational speed of the tool, tool advancing speed, magnitude of downward force to hold the touch between tool and piece steady, tool geometry, and tilt angle and type of material (thermophysical properties). These variables affect heat distribution as well as residual stress and mechanical properties of the connection. A portion of the generated heat disseminated through work piece, will affect distortion, residual stress distribution as well as weld quality of the piece. Chao et al. [4] investigated the variations of heat energy and temperature produced by the FSW they point that only about 5% of the heat generated by the

friction process flows to the tool and the rest flows to the work piece.

They formulated a boundary value problem for tool and workpiece in order to study the heat transfer in friction stir welding. They determined the frictional heat flux from the measured transient temperature fields obtained in the finite element analyses.

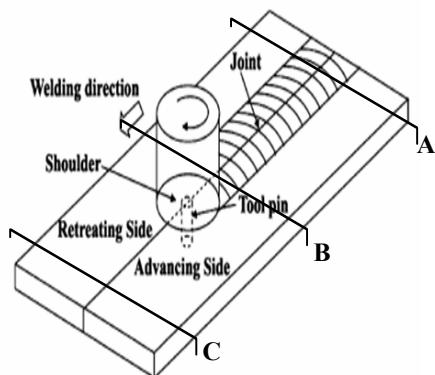


Fig. 1 Schematic illustrations of the friction stir welding process [3].

Schmidt et al. [5] proposed a general analytical model for heat generation based on two contact conditions at the tool/matrix interface, namely full sliding and full sticking condition. Mandal et al. [6] provided a theoretical framework for developing a thermo-mechanical hot channel approach for augmenting the FSW process. Song et al. [7] used a three dimensional heat transfer model to predict the temperature distributions in FSW. They assume that heat generated at the tool shoulder/work piece interface is frictional heat and the plastic strain is negligible. Zhang et al. [8–10] used the two- and three-dimensional thermo-mechanical model to analyze the material flows, temperature history and mechanical features in the FSW process. Nandan et al. [11, 12] have modeled a Three-dimensional visco-plastic flow of metals and the temperature fields in friction stir welding of 6061 aluminum alloy and 304L austenitic stainless steel. Chen and Kovacevic [13] used a three-dimensional model based on finite element analysis to study the thermal history and thermo-mechanical process in the butt-welding of aluminum alloy 6061-T6. Their model was symmetry along the weld line and incorporated the mechanical reaction of the tool and thermo-mechanical process of the welded material [14, 15].



Peel et al. [16] reported the results of microstructural, mechanical property, and residual stress investigations produced under varying conditions. They concluded that the weld properties were dominated by the thermal input rather than the mechanical deformation by the tool. Also, it was found out that the weld zone in FSW is in tension in both the longitudinal (parallel to tool travel) and transverse (perpendicular to tool travel) directions.

A simple three-dimensional thermomechanical model for friction stir welding (FSW) is presented. It is developed from the model proposed by Heurtier et al. (2006) [17] based on a combination of fluid mechanics numerical and analytical velocity fields. Mohamed assidi [18] used simplified numerical models and approaches the recent development of more accurate 3D simulation software which allows modeling the entire complexity of the FSW process, makes it possible to follow a much more rigorous inverse analysis (or calibration) approach ,FSW trials are conducted on an Al 6061 aluminum plate with an unthreaded concave tool. Force and tool temperature are accurately recorded at steady welding state for different welding speeds, the numerical simulations were based on an Arbitrary Lagrangian Eulerian (ALE) formulation that has been implemented in the Forge3 F.E. Software.Mohammad R. [19] investigated; three-dimensional numerical simulation of friction stir welding concerning the impact of tool moving speed in relation with heat distribution as well as residual stress.

Objective of this study was to predict numerical transient temperature distribution in Al7020-T53 plates that were welded by friction stir welding method for advancing speed of 40mm/min and rotational speed of 1400rpm. The model chosen for this task was the thermal model developed by Nandan [12] for FSW of aluminum alloy. The developed model was validating according experimental thermocouples data recorded; the thermal model was used to simulate the process. The model was then extrapolated to perform parametric studies in order to investigate effects of various process parameters on temperature distribution in the workpiece.

### Model Description:

The welding process is shown in fig. (1) where travel speed is 40mm/min and rotational speed 1400rpm. The friction stir welding tool was fabricated from a tool steel labeled as X12M [20](density  $\rho=7800\text{kg/m}^3$ ,specific heat  $C_p=500\text{J/kg}^\circ\text{C}$  and thermal conductivity  $k=40\text{W/m}^\circ\text{C}$ ) and is heat treatment includes heating the metal to  $1020^\circ\text{C}$  for 30 min and then air cooling to room temperature. The tool had a concaved shoulder ( $2^\circ$ ), while the cylindrical tool pin has a right hand threads of (1)mm pitch with a round bottom .the overall height of the pin is (4.7mm), made slightly shorter than the sheet thickness with shoulder diameter (18mm) and pin diameter (6mm) as shown fig.2.

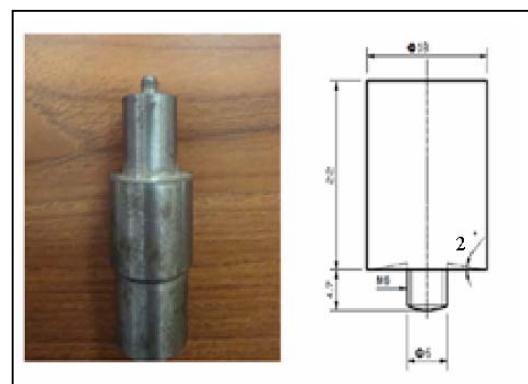


Fig. 2 the configuration of the tool used

The welded plate are AA 7020-T53 Al alloy, each is in rectangular shape with a size of (153\*95\*5 mm). The tool is considered a rigid solid, and the work piece is considered a ductile material characterized with elasticity, plasticity and kinetic hardening effect. The temperature-dependent properties of 7020-T53 Al alloy at various temperatures are given in table (1) [21], a piece of this alloy was analyzed to find its chemical composition by Spectro device in Specialized Institute for Engineering Industries (SIEI), table (2) shows the chemical composition.

The FSW process is divided into the following three phases: (a). the penetration phase, (b). the welding phase and (c). the tool pull-out phase. The heat is generated due to friction and plastic deformation at the tool and work piece interface during the process. During the welding period, the tool is moving at constant travel speed (40mm/min) and rotating speed (1400rpm) along the joint line.

Table 1: Thermal material properties of AA 7020-T53 Al alloy [21]

Temp.(k)	$\rho(\text{kg/m}^3)$	$C_p (\text{J/Kg K})$	K(W/m.K)
300	2780	875	148
373	2770	910	159
473	2755	960	164
573	2740	980	173
673	2720	1040	182
733	2700	1100	196

Table (2) Chemical composition of AA 7020-T53

Si	Fe	Cu	Mn	Mg
0.166	0.256	0.142	0.111	1.29
Ni	Zn	Ti	Be	Pb
0.0037	4.61	0.0424	0.00062	0.0066
V	Zr	Al	Cr	Sn
0.0081	0.140	balance	0.213	$\leq 0.0010$

ANSYS® 12.0 was used for numerical simulation of friction stir welding process the thermal and mechanical responses of the material during friction stir welding process are investigated by finite element simulations. The finite element models are parametrically built using APDL (ANSYS Parametric Design Language) provided by ANSYS® [23]. Non-linearity of this model is because of the material nonlinearity. Material nonlinearities occur because of the nonlinear relationship between stress and strain; that is, the stress is a nonlinear function of the strain. Non-linear relations appear because of temperature dependent mechanical properties [22].

### Thermal Model:

The purpose of the thermal model is to calculate the transient temperature fields developed in the workpiece during friction stir welding.

In the thermal analysis, the transient temperature field  $T$  which is a function of time  $t$  and the spatial coordinates  $(x,y,z)$ , is estimated by the three dimensional nonlinear heat transfer equation (1).

$$\left( \frac{\partial}{\partial}(k_x(T)(\frac{\partial T}{\partial x}) + \frac{\partial}{\partial}(k_y(T)(\frac{\partial T}{\partial y}) + \frac{\partial}{\partial}(k_z(T)(\frac{\partial T}{\partial z})) \right) + Q_{int} = \frac{\partial(c(T)\rho(T)T)}{\partial t} \quad (1)$$

where  $k(T)$  is the coefficient of thermal conductivity ,  $Q_{int}$  is the internal heat source rate,  $c_p(T)$  is the mass-specific heat capacity, and  $\rho(T)$  is the density of the materials. The heat transfer model developed for the thermal analysis is described in the following section.

**Assumptions:** A number of assumptions have been made in developing the finite element thermal model, which includes:

- Workpiece material is isotropic and homogeneous.
- No melting occurs during the welding process.
- Thermal boundary conditions are symmetrical across the weld centerline.
- Heat transfer from the workpiece to the clamp is negligible.
- Two symmetry planes are applied on lateral sides of the workpiece.

**Elements Used** In the present thermal analysis, the workpiece is meshed using a brick element called SOLID70. The element is defined by eight nodes with temperature as single degree of freedom at each node and by the orthotropic material properties.

### Boundary Condition

Boundary condition for FSW thermal model were specified as surface loads through ANSYS® codes. Assumptions were made for various boundary conditions based on data collected from various published research papers [24, 25]. Convective and radiative heat losses to the ambient occurs across all



free surfaces of the workpiece and conduction losses occur from the workpiece bottom surface to the backing plate. To consider convection and radiation on all workpiece surfaces except for the bottom, the heat loss  $q_s$  is calculated by:

$$q_s = \beta (T - T_o) + \varepsilon F \sigma (T^4 - T_o^4) \quad (2)$$

where  $T$  is absolute temperature of the workpiece,  $T_o$  is the ambient temperature,  $\beta$  is the convection coefficient,  $\varepsilon$  is the emissivity of the plate surfaces, and  $\sigma = 5.67 \times 10^{-8} \text{ W/m}^2 \text{ K}^4$  is the Stefan-Boltzmann constant. In the current model, a typical value of  $\beta$  was taken to be  $30 \text{ W/m}^2\text{K}$  at ambient temperature of  $300 \text{ K}$  [30] and  $\varepsilon$  was taken to be  $(0.5)$  for aluminum alloy  $F$  is radiation view factors ( $F=1$ ). In order to account for the conductive heat loss through the bottom surface of weld plates, a high overall heat transfer coefficient has been assumed. This assumption is based on the previous studies [4, 26]. The heat loss was modeled approximately by using heat flux loss by convection  $q_b$  given by ;

$$q_b = \beta_b (T - T_o) \quad (3)$$

where  $\beta_b$  is a fictitious convection coefficient. Due to the complexity involved in estimating the contact condition between the welded plate and the backing plate, the value of  $\beta_b$  had to be estimated by assuming different values through reverse analysis approach. In this study, the optimized value of  $\beta_b$  was found to be  $(100-300) \text{ W/cm}^2\text{C}$ .

The heat transfer coefficient at the bottom face depends on the local temperature and is given by following relation [31]:

$$\beta_b = \beta_{bo} (T - T_o)^{0.25} \quad (4)$$

Where  $\beta_{bo}$  is the heat transfer parameter for the bottom surface.

Figure (3) shows the schematic representation of boundary conditions that were used for thermal analysis.

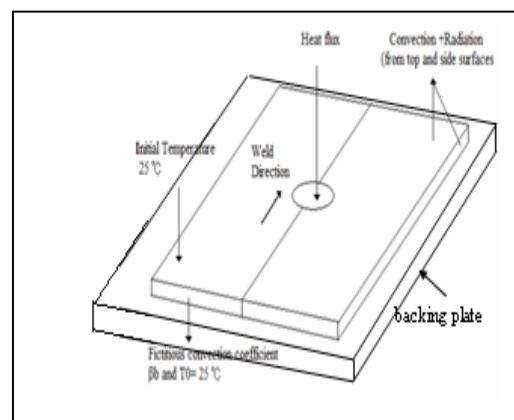


Fig. 3 Schematic representation of boundary condition for thermal analysis

Heat generation during friction-stir welding arises from two main sources: deformation of the material around the tool pin and the friction at the surface of the tool shoulder. A major difficulty is determining suitable values for the friction coefficient. The conditions under the tool are both extreme and very difficult to measure. To date, these parameters have been used as 'fitting parameters' where the model works back from measured thermal data to obtain a reasonable simulated thermal field. While this approach is useful for creating process models to predict, for example, residual stresses it is less useful for providing insights into the process itself. Mathematical approximations for the total heat generated by the tool shoulder may be used to compensate for deformation heat generation; this could be done by an adjusting coefficient of friction. Friction is a complex physical phenomenon that depends on parameters like material, surface roughness, lubrication, temperature and pressure. The effects of friction in metal forming simulations are commonly accounted for by Coulomb friction models [27]. Assuming slipping conditions, the friction coefficient is adjusted in order to calibrate the model. A wide range of published values for friction coefficient is within  $0.3-0.85$  [28], which reflect the experimental conditions.

Total frictional heat of shoulder at rubbing angular speed of  $(1-\delta)\omega$ , will be:

$$Q_s = \frac{2}{3} \pi (1-\delta) \omega \mu P R_s \quad (5)$$

where  $Q_s$  heat generation by shoulder,  $\omega$  rotational speed rps,  $\mu$  coefficient of friction,  $P$  pressure ,  $R_s$  radius of shoulder and  $\delta$  is the slip factor that

compensate for tool/material relative velocity.

Typical values for slip factor found in literature ranges between 0.6, 0.85 [29].

In similar concept, heat generated by lateral surface of the pin is:

$$Q_p = 2\pi(1-\delta)\omega\mu PL_p R_p^2 \quad (6)$$

where  $Q_p$  heat generation by pin surface,  $\omega$  rotational speed rps,  $\mu$  friction coefficient,  $P$  axial pressure N/m<sup>2</sup>,  $L_p$  pin length and  $R_p$  pin radius. Total frictional heat generated by the tool is the summation of equations (5) and (6) which is:

$$Q_T = 2\pi(1-\delta)\omega\mu P((R_i^3/3) + L_p R_p^2) \quad (7)$$

During the process the tool travels at a constant speed ( $V_t$ ). This motion was simulated by changing heat source location, as shown in figure (4), according to the following equation:

$$X_{i+1} = X_i + V_t \Delta t \quad \text{for } L_i \leq X \leq L_w$$

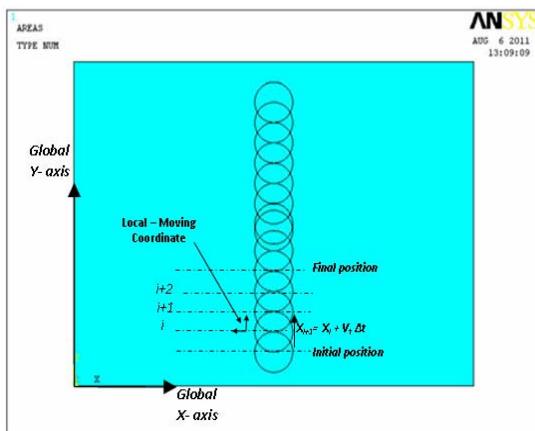


Fig. 4 Modeling of Heat Source Movement at Different Time Steps.

Where  $\Delta t$  is the time required for the tool to travel from location  $X_i$  to  $X_{i+1}$ , (i.e. element size) and  $V_t$  is the tool traveling speed.

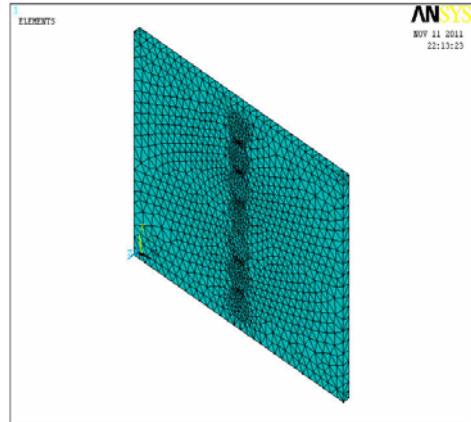


Fig. 5 Finite Element Model and Mesh.

The finite element equation after applying boundary condition can be expressed in matrix form[;

$$T^e(x,y,z,t) = [N(x,y,z,t)] \{T^e\} \quad (8)$$

$$[N(x,y,z)] = [N_i(x,y,z) \quad N_j(x,y,z) \quad N_p(x,y,z)] \quad (9)$$

$$\{T^e\} = \begin{Bmatrix} T_i(t) \\ T_j(t) \\ T_p(t) \end{Bmatrix} \quad (10)$$

$$\frac{\partial T^e}{\partial x} = \left[ \frac{\partial N_i}{\partial x} \frac{\partial N_j}{\partial x} \frac{\partial N_p}{\partial x} \right] \{T^e\} \quad (11)$$

$$\frac{\partial}{\partial T_m} \left( \frac{\partial T^e}{\partial x} \right) = \frac{\partial N_m}{\partial x} \quad (12)$$

$$\frac{\partial T^e}{\partial T_m} = N_m \quad (13)$$

$$\frac{\partial T^e}{\partial t} = [N] \{\dot{T}\} \quad (14)$$

Where

$$\{\dot{T}^e\} = \begin{Bmatrix} \frac{\partial T_i}{\partial t} \\ \frac{\partial T_j}{\partial t} \\ \frac{\partial T_p}{\partial t} \end{Bmatrix} \quad (15)$$



$$[k]\{T\} + \dot{[k]}\left\{\dot{T}\right\} = \{F\} \quad (16)$$

Where

$$[k] = \sum_{e=1}^{ne} [k_1^e] + [k_2^e] \quad (20)$$

$$\left[\dot{k}\right] = \sum_{e=1}^{ne} [k_3^e] \quad (21)$$

And

$$\{F\} = \sum_{e=1}^{ne} \{F^e\} \quad (22)$$

The expression for  $K_1$ ,  $K_2$ ,  $K_3$  and  $F$  can be stated using matrix notation

$$[K_1] = \iiint_v [B]^T [D][B]dv \quad (23)$$

$$[K_2] = \iiint_s h[N]^T [N]dS \quad (24)$$

$$[K_3] = \iiint_v \rho c[N]^T [N]dv \quad (25)$$

$$\{F^e\} = \int_{ve} Q[N]^T dv + \int_{s_2e} hT_\infty[N]^T ds_2 - \int_{s_3e} q[N]^T ds_3 \quad (26)$$

$$D = \begin{bmatrix} K_x & 0 & 0 \\ 0 & K_y & 0 \\ 0 & 0 & K_z \end{bmatrix} \quad (27)$$

$$[B] = \begin{bmatrix} \frac{\partial N_1}{\partial x} & \frac{\partial N_2}{\partial x} & \frac{\partial N_3}{\partial x} & \dots & \frac{\partial N_8}{\partial x} \\ \frac{\partial N_1}{\partial y} & \frac{\partial N_2}{\partial y} & \frac{\partial N_3}{\partial y} & \dots & \frac{\partial N_8}{\partial y} \\ \frac{\partial N_1}{\partial z} & \frac{\partial N_2}{\partial z} & \frac{\partial N_3}{\partial z} & \dots & \frac{\partial N_8}{\partial z} \end{bmatrix} \quad (28)$$

$N_1$ ,  $N_2$ ,  $N_3$ .....  $N_8$  are shape functions in natural coordinate system for brick element.

$$N_i = \frac{(1+\xi_i)(1+\eta_i)(1+\zeta_i)}{8} \quad (29)$$

With  $\xi_i, \eta_i, \zeta_i = \pm 1$  and  $i=1,2,3,\dots,8$

## Simulation

The thermal modeling was carried out in transient thermal analysis. Its main features are an Arbitrary Lagrangian Eulerian (ALE) formulation. To build the model a title was specified for the analysis and preferences were set for the options to display (thermal). Then ANSYS preprocessor (PREP7) was used to do these tasks:

- Define element types and options.
- Define material properties.
- Create model geometry.
- Mesh the model geometry.

The transient analysis was managed either by defining multiple load steps (for stepped or ramped boundary conditions) or by using a single load step and tabular boundary conditions (for arbitrary time-varying conditions) with an array parameter to define the time points. To use the load step method, this procedure was followed:

- Specify the time at the end of the load step.
- Specify whether the loads are step or ramp.
- Specify the load values at the end of the load step.
- Write information to a load step file.
- Repeat these steps for the next load step, and so on until finishing all load step data.
- Since the problem involves nonlinear analysis, full Newton-Raphson option was used to solve the nonlinear equations.

## Force and temperature measurements:

Experiments are conducted under different welding rotational speeds, four cases are considered with differing tool rotational speeds (710rpm, 900rpm, 1120rpm and 1400rpm) a component dynamometer based on load cell (SEWHA, 2000kg capacity, R.O:2.0008mV/V) is used for measuring the vertical force during the FSW process for penetration time 60sec after that tool is moved with constant travel speed. This load cell for vertical force measurement is fixed on the rotating tool, and transmitter is used for transmitting the analog force data to the weight indicator capacity (2000kg) (SEWHA, SI4010) fig. (6) and fig. (7) Show the vertical force measured from FSW process for different tool rotational speed. The sampling frequency of data for force measurement is 10Hz.



Fig.6 Vertical load cell measuring sensors.

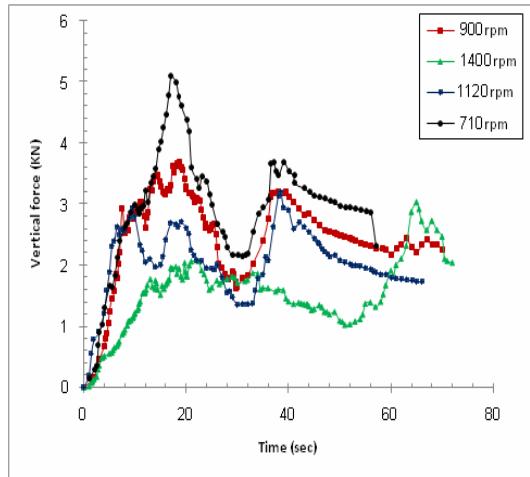


Fig. 7 Vertical force penetration of tool on the workpiece during the FSW process.

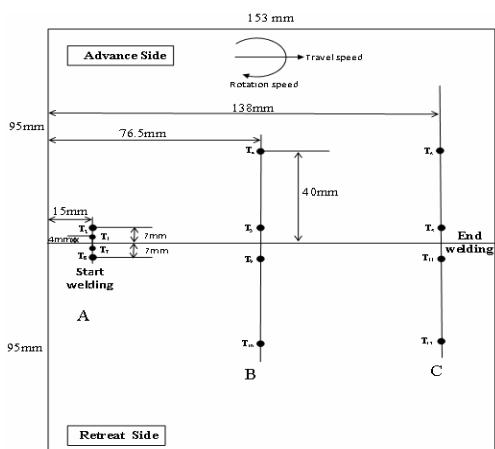


Fig. 8 thermocouple positions on the workpiece

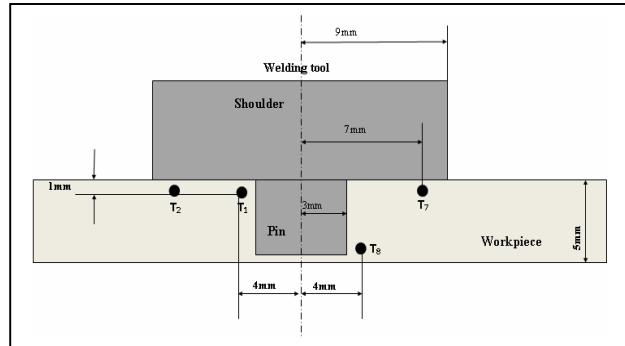


Fig. 9 Thermocouples position at tool penetration on workpiece at section A-A.



Fig. 10 Temperature recorder and hole drill thermocouple position on workpiece.

the plates are prepared to measure the temperature at (12 locations using k type thermocouples at three sections (A, B and C) as shown in fig.(1) calibrated in central organization for standardization quality control, The locations of thermocouples in the workpiece are shown in fig.(8). Thermocouples connected to the 12 channels reader, Transient temperatures are recorded in the 12channels during FSW process; thermocouples are attached to SD card data logger temperature recorder (BTM-4208SD), range (-100 to 1100 °C).

For section (A) in fig. (8), four thermocouples (channels 1, 2, 7 and 8) are located in heat affected zone (HAZ) for (channels 2 and 7 in advance and retreat side respectively) and the other thermocouples (channels are located in nugget zone NZ) as shown in fig. (9).



### Results and discussion:

During the penetration phase, the rotating tool pin penetrates into the workpiece until the tool shoulder comes in contact with the workpiece. The penetration speed is chosen to be (0.0783mm/sec) in the model, and the corresponding penetration time is approximately (80sec).

convection heat transfer coefficient with backing plate ( $300\text{W/m}^2\text{k}$ ) , convection heat transfer coefficient( $30\text{W/m}^2\text{k}$ ), ambient and initial temperature ( $T_0=293\text{K}$ ), slip factor ( $\delta=0.6$ ), friction coefficient ( $\mu=0.41$ ), (axial load= $2\text{kN}$ ) , Heat generation( $Q=331\text{watt}$ ) used as input welding parameters in the finite element calculation with their corresponding vertical force in the workpiece predicted in fig.(7) the plasticization of material under the tool increases with increasing rotational speed and with decrease in tool traverse speed resulting the reduction of vertical force.

The finite element simulation couples the moving tool with the workpiece and also considers the thermal effect of the initial tool pin penetration before start of the weld

Fig. (11) Present cross-sectional views of the calculated temperature contours in the workpiece and tool at different time during the penetration. This figure graphically illustrates the temperature history of the workpiece and the tool during the pin penetration. The highest temperature is observed in the centre of the weld region extending down from the crown surface to the probe root side, since the rotation of the shoulder and the probe (pin) contributes the highest heat flux in this region. The relatively higher heat dissipation through the contact surface between the welded plate and the backing plate as compared with the top surface the top surface of the plate causes the temperature contour in the weld nugget area the follow a "V" shape .This is because of the relatively higher convection coefficient at the bottom surface of plate as compared with the top surface. It is believed that the described "V" -type distribution of the temperature in the weld zone contributes to the grain coarsening in the TMAZ and the HAZ.

Fig. (12) and fig. (13) show the experimentally thermocouples reading and FEM result for (channel T1) that located 4.5mm from joint line and at

(channel T8) located 1mm in the bottom of workpiece as shown in fig.(9).

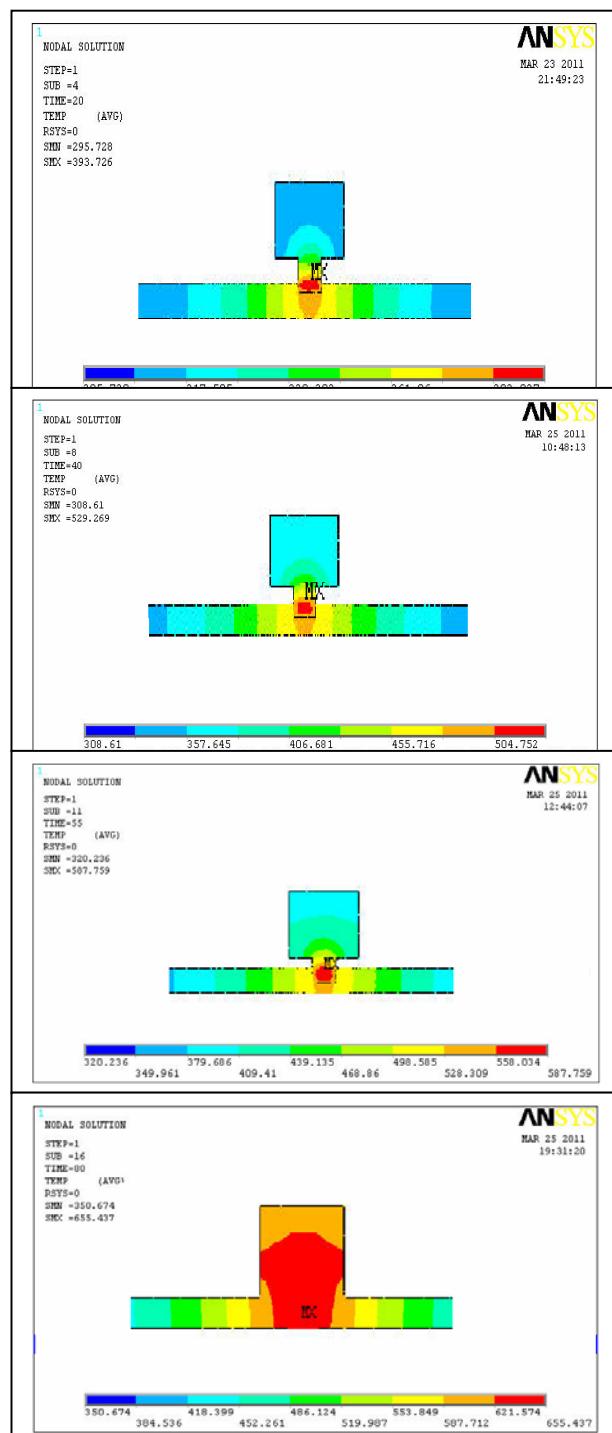


Fig. 11 Temperature-Time history for tool and workpiece during tool pin penetration  
( $V_t=40\text{mm/min}$ ,  $\omega=1400\text{rpm}$ )

Fig. (14) shows the effect of thermocouple position where (T1) at the top and (T8) at the bottom, (T1; 645 °K) is higher than (T8; 635.79°K), initially T1 increase with pin penetrate in the work piece while the pin continue of penetrate action T8 sense increasing in temperature but T1 still higher than T8 due to contact of shoulder which increased the temperature that increase by stirring and friction around the pin.

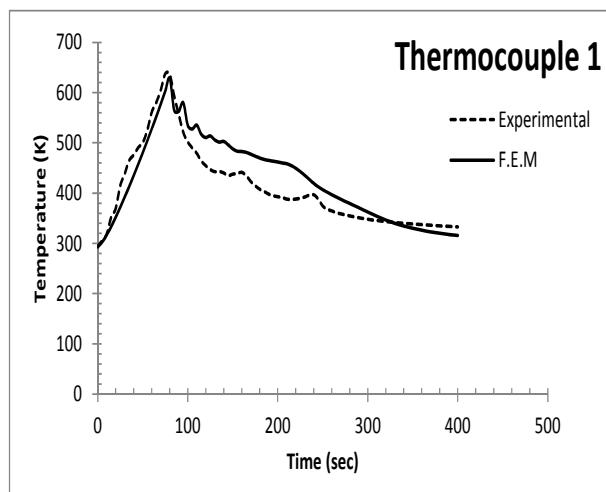


Fig. 12 Comparison of the modeled and measured temperature history for thermocouple T1

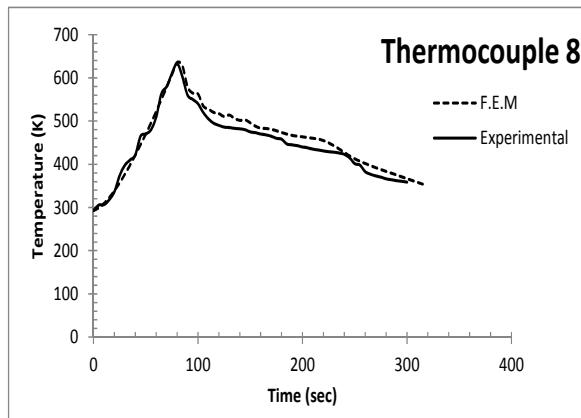


Fig. 13 Comparison of the modeled and measured temperature history for thermocouple T8

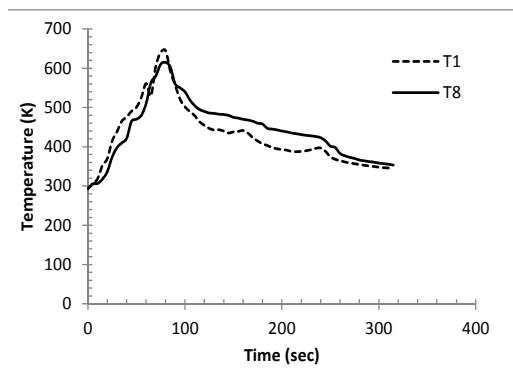


Fig. 14 Comparison measured temperature history for thermocouple location 4mm from joint line at top (T1) and bottom (T8)

Fig.15; shows temperature recorded by thermocouple T2(629K) in advance side at location 7mm from joint centre line fig.(9), in retreat side thermocouple T7(605K) at location 7mm from joint centre line fig.(9). Experimentally result shows the temperature in advance side is higher than retreat side because material flow and plastic deformation around tool moving from advance side to retreat side additional to friction heat under the shoulder that gives higher temperature the computational results show that the material flows on the retreating and the front sides are higher. So, the slipping rates on the retreating and the front sides are lower than the ones on the trailing and advancing sides. This is the reason that the heat fluxes on the trailing and the advancing sides are higher, which leads to the fact that the temperatures are higher in this region for both thin plates [32].

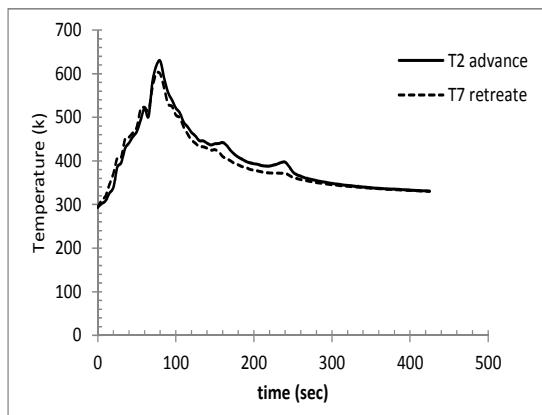


Fig. 15 shows thermocouples measured value in advance T1 and retreat side T7 at section A-A

Fig.16 shows the maximum temperature while the tool ending the penetration (80sec) ,shoulder is in contact with the surface of workpiece so that in section A-A thermocouple T1 in advance side at location 4mm from joint centre line recorded maximum temperature (645K), thermocouple T2 in advance side at location 4mm from joint centre line recorded maximum temperature (637K) and thermocouple T7 in advance side at location 4mm from joint centre line recorded maximum temperature (605K) it noticeable that temperature difference along two sides (advance and retreat ) of welding centre line, but in simulation the temperature is symmetric along welding centre line at each side [31].

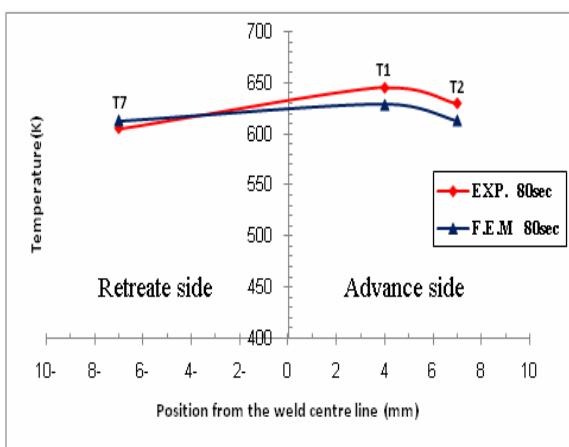


Fig. 16 comparison of simulated and measured temperature along transverse direction at section A-A (end of penetration)

Fig. (17); shows numerical simulation of the temperature history at 7mm along welding line in advance side where (TEMP-2) at section A-A with time 80sec welding tool ending penetration phase (dwell), (TEMP-3) at section B-B with time 160sec welding tool at mid position of welding line and (TEMP-5) at section C-C with time 240sec welding tool pullout at end of welding line.

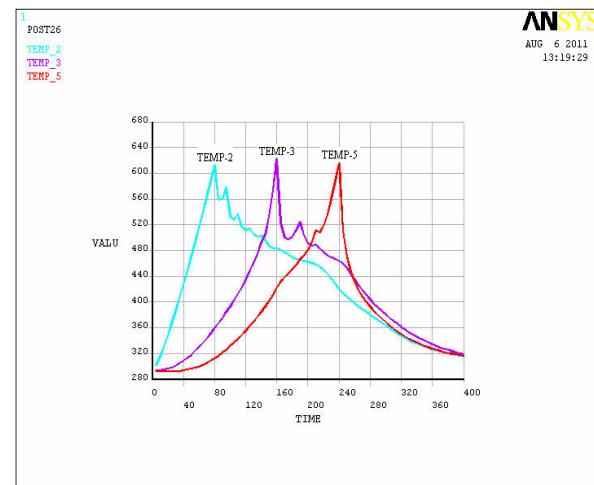


Fig.(17) Temperature-time profile for F.E.M value at location 7mm from joint line in advance side  
( $V_t=40\text{mm/min}$ ,  $\omega=1400\text{rpm}$ )

Fig. (18) Shows a comparison of experimental value and F.E modeled value for thermocouple T3 at section B-B while the tool traveled at mid position along tool movement in welding line at time 160sec.

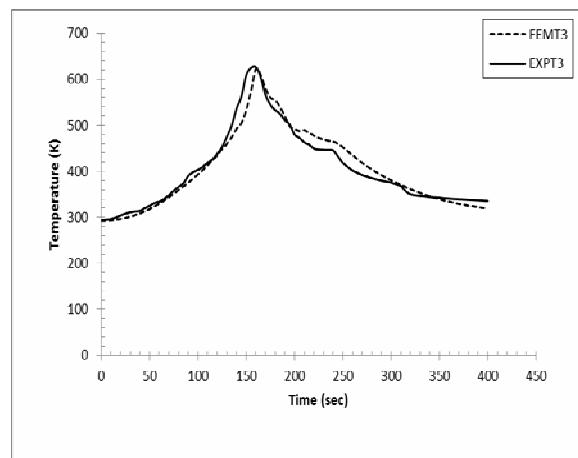


Fig. 18 Comparison of the modeled and measured temperature history for thermocouple T3 location 7mm from joint line on advance side in section B-B

Fig. (19) Shows comparison of experimental value and F.E modeled value for thermocouple T5 in section C-C while the tool traveled at end welding line at time 240sec.

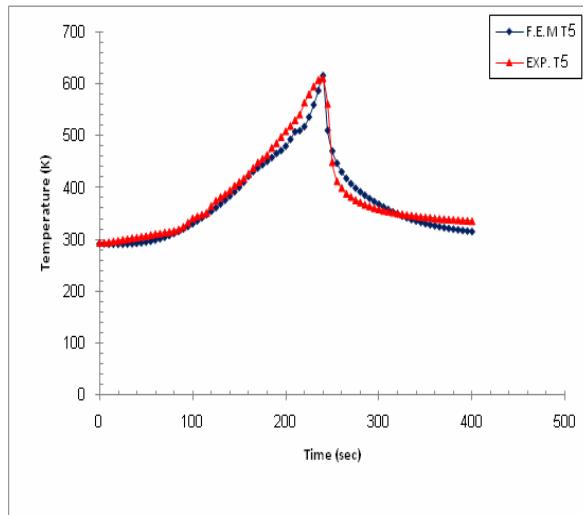


Fig. 19 Comparison of the modeled and measured temperature history for thermocouple T5 location 7mm from joint line on advance side in section C-C.

Fig. (20) shows modeling temperature contour distribution when the tool moving along welding line at mid position of the workpiece at time 160sec ,the temperature distribution effected by heat conduction between the work piece with fixture and by convection, radiation ambient travel speed also has influence on temperature distributions travel speed and rotating speed on transient temperature distribution.

Fig. (21) shows finite element modeling of the distribution of temperature in the transverse direction of welding line in the section B-B when welding tool at mid position of workpiece and according to assumption symmetric value in advance and retreat side  $T_{max}=642K$  for (1400rpm-40mm/min).

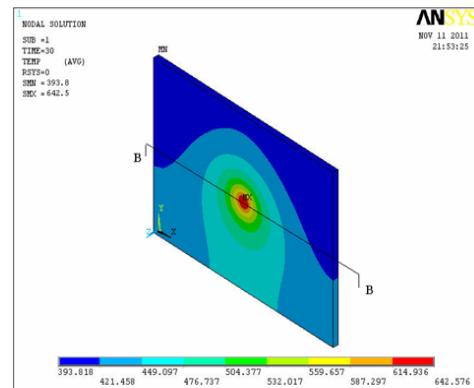


Fig. 20 temperature gradient contour in the top surface of the workpiece at the movement the tool moves to the middle point of the plate ( $\omega=1400\text{rpm}$  and  $V_t=40$ )

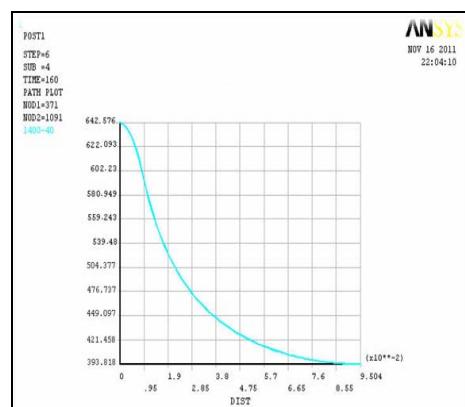


Fig. 21 Finite element temperature distribution in mid position in work piece sec B-B in direction perpendicular to welding line at welding parameter ( $\omega=1400\text{rpm}$  and

Fig. (22) shows temperature modeled and measured at section B-B when tool position at mid welding line with time 160sec, thermocouples T3, T4 in

advance side and T9, T10 in retreat side (the letter T refer to thermocouple number and position), the thermocouples placed at depths 0.5mm below the top surface thermocouple reading shows temperature in advance (T3=626.6K) is larger than retreat side (T9=609.1K).

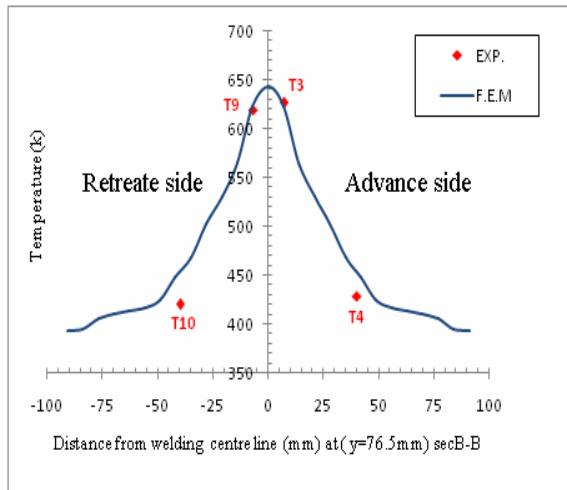


Fig. 22 comparison of F.E.M value and measured temperature distribution of along transverse direction welding line at sec.B-B ( $\omega=1400\text{rpm}$  and  $V_t=40\text{mm/min}$ ).

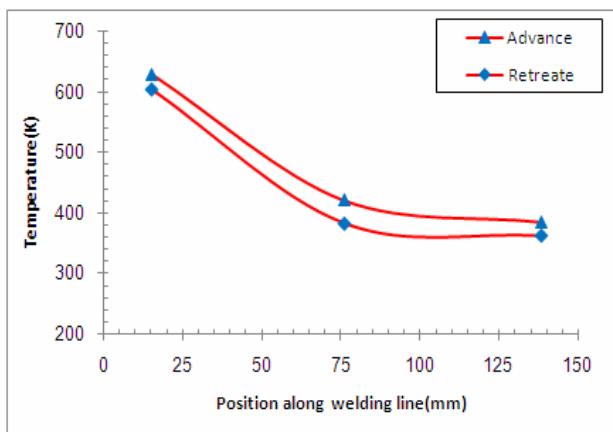


Fig.23 Measured temperature along welding line at starting tool moving (80sec) ( $V_t=40\text{mm/min}$ ,  $\omega=1400\text{rpm}$ )

Fig. (23), fig.(24) and fig.(25) show thermocouples measured temperature when tool moving along welding line at three position start, mid and end moving figures show the difference reading between advance side and retreating side.

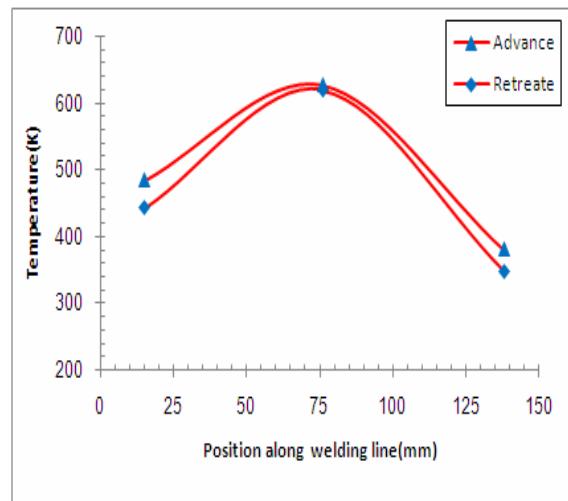


Fig. 24 Measured temperature along welding line at mid tool moving (160sec) ( $V_t=40\text{mm/min}$ ,  $\omega=1400\text{rpm}$ )

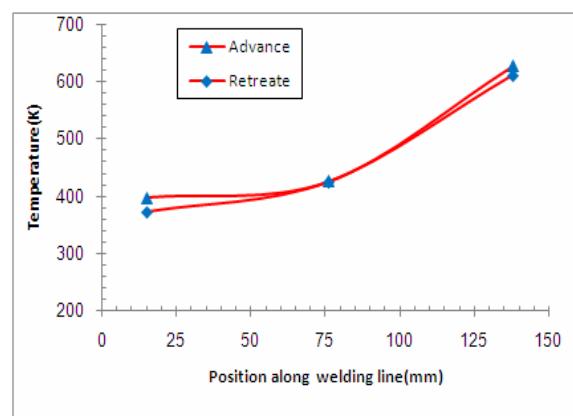


Fig. 25 Measured temperature along welding line at end tool moving (240sec) ( $V_t=40\text{mm/min}$ ,  $\omega=1400\text{rpm}$ )

Fig.26 and fig.27 shows temperature contours when penetration of welding tool in the workpiece, temperature increases with increase tool penetration with two stages: first stage when tool pin penetrate into the workpiece when the tool moving axially with constant axial speed and second stage when tool shoulder contact with workpiece in this time end dwell and then the welding tool moving at constant travel speed 40mm/min. A figure shows that the maximum temperature gradient happens in the region formed by the edge of the shoulder. This event is attributed to the fact that the highest heat generation in this region and the highest heat

radiation and convection dissipations of the region occur just beyond the shoulder edge [25].

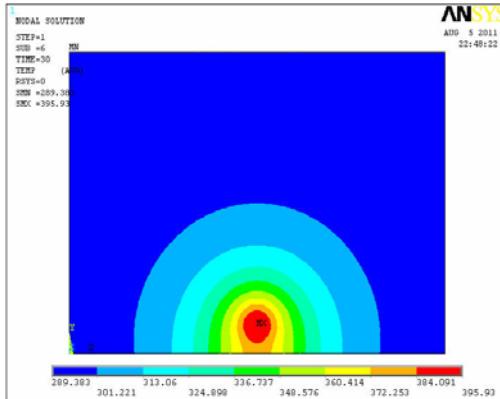


Fig.26 Temperature Distribution at time 30 sec

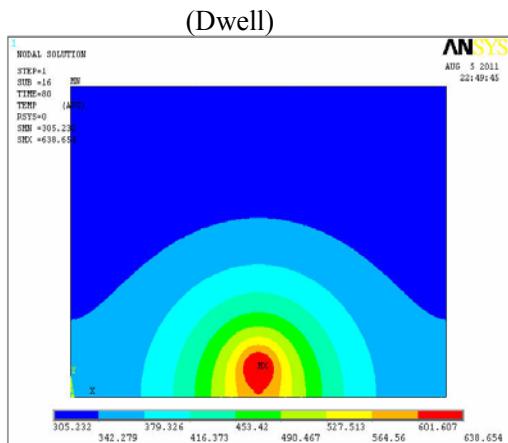


Fig.27 Temperature Distribution at time 80 sec (end of Dwell)

Fig.28 to fig.32 shows thermal distribution when the tool penetrates in workpiece (beginning the welding process) at time 80sec, then start moving of the tool along welding line to mid position of the workpiece at time 160sec and the end position of welding tool at time 240sec after that welding tool pullout from workpiece and then work piece cooled as shown in

fig.31. The temperature distribution effected by heat conduction between the work piece with fixture and by convection, radiation ambient travel speed also has influence on temperature distributions increase travel speed decrease temperature history [25].

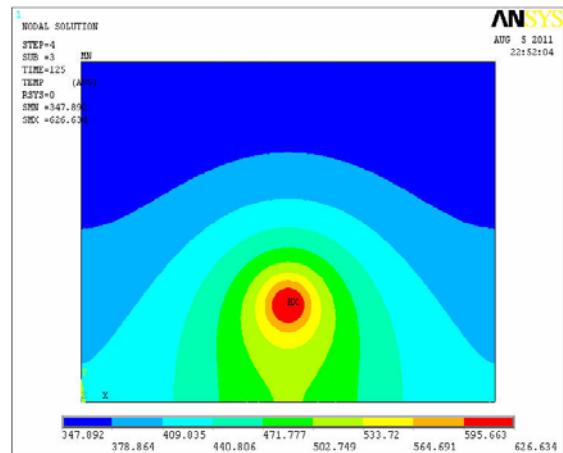


Fig.28 Temperature Distribution at time 125 sec (welding tool moving along welding line)

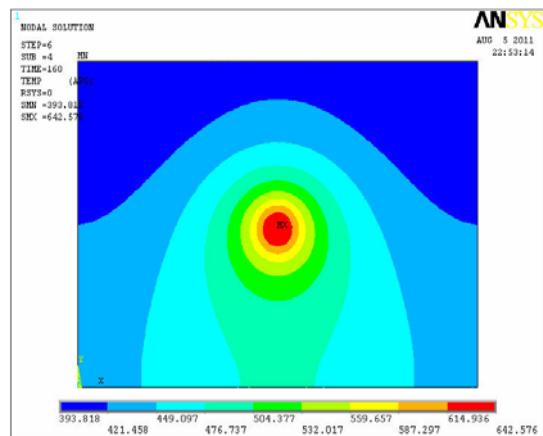


Fig.29 Temperature Distribution at time 160 sec moving welding tool at mid position of welding line

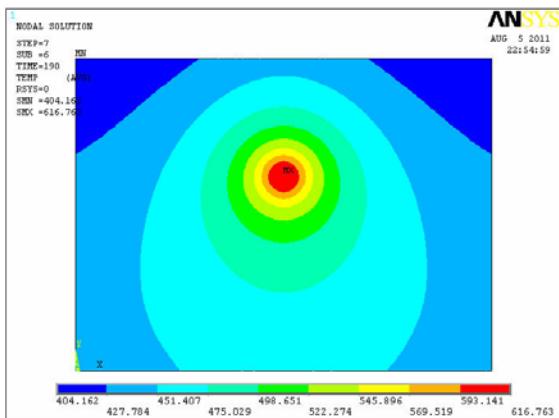


Fig.30 Temperature Distribution at time 190 sec  
(welding tool moving along welding line)

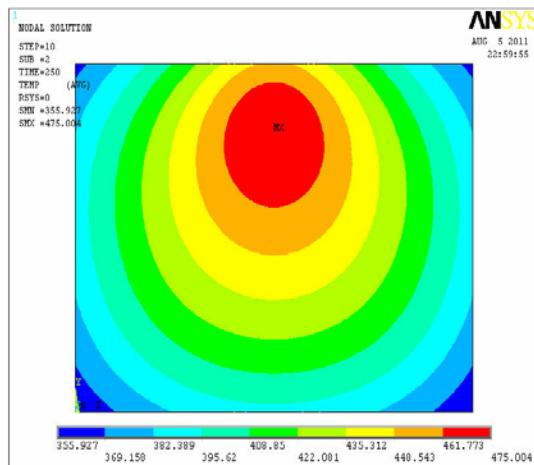


Fig.32 Temperature Distribution at time 250 sec  
(Cooling)

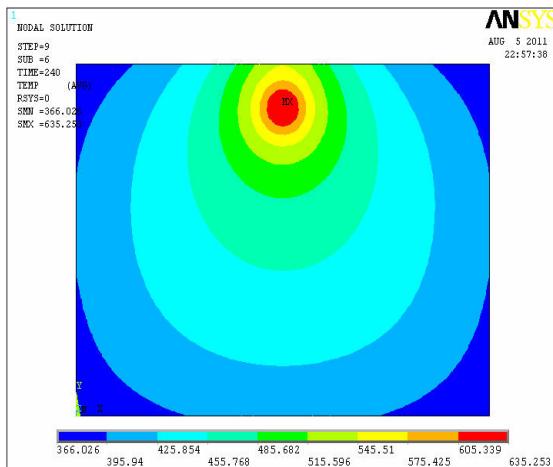


Fig.31 Temperature Distribution at time 240 sec  
(End of Moving) tool pullout

### Conclusion:

To study the variations of transient temperature in friction stir welding of AA 7020-T53 plates, detailed three-dimensional nonlinear thermal simulations are performed for the FSW process using the finite element analysis ANSYS. 40 mm/min travel speed with tool rotational speeds of 1400 rpm is considered. From the analyses, we can summarize the results as follows:

- Axial load measured from experimental work decreases with increasing rotational speed because that decrease in strength due to temperature increases in penetration position.
- The experimental data show the maximum temperature measured during FSW at mid position 629k and numerically value from the simulation is 642K<sup>o</sup>, which is significantly less than the melting temperature of 7020-T53 aluminum alloy at 916K<sup>o</sup>.
- The temperature measured at advance side (629k) is higher than retreat side (605k).
- Numerical results (Tmax =642K) agreement with measured data (Tmax=629k) (error 2%).
- The computational results show that the material flows on the retreating and the front sides are higher. So, the slipping rates on the retreating and the front sides are lower than the ones on the trailing and advancing sides. This is the reason that the heat fluxes on the trailing and the advancing sides are higher, which leads to the fact that the temperatures are higher in this region for both thin plates.

**Reference:**

1. Zhang Z; Zhang HW (2008) "A fully Coupled Thermo-Mechanical Model Of Friction Stir Welding". *Int. J. Adv. Manuf. Technol.* 37:279–293.
2. Cho JH, Boyce DE, Dawson PR. (2005)."Modeling Strain Hardening and Texture Evolution in Friction Stir Welding of Stainless Steel". *Mater. Sci. Eng.* 398:146–163.
3. Nandan R. DebRoy T. Bhadeshia HKDH (2008). "Recent Advances in Friction-Atir Welding Process, Weldment Structure and Properties". *Prog. Mater. Sci.* 53:980–1023.
4. Chao YJ. Qi X. Tang W. (2003) "Heat transfer in Friction Stir Welding Experimental and Numerical Studies". *J. Manuf. Sci. Eng.* 125:138–145.
5. Schmidt HB. Hattel JH. (2008)." Thermal Modeling of Friction Stir Welding". *Scr. Mater.* 58:332–337.
6. Mandal S, Williamson K (2006)." A thermo-Mechanical Hot Channel Approach For Friction Stir Welding". *J. Mater. Process. Technol.* 174:190–194.
7. Song M. Kovacevic R. (2003)." Thermal Modelings of Friction Stir Welding in A moving Coordinate System and Its Validation". *Int. J. Mach. Tools. Manuf.* 43:605–615.
8. Zhang HW. Zhang Z. Chen JT. (2005)." The finite Element Simulations of The friction Stir Welding Process". *Mater. Sci. Eng.* 403:340–348.
9. Zhang Z. Zhang HW. (2007)." Material behaviors and Mechanical Features in Friction Stir Welding Process". *Int. J. Adv. Manuf. Technol.* 35:86–100.
10. Zhang Z. Zhang HW. (2009)." Numerical studies on Controlling of Process Parameters in Friction Stir Welding". *J. Mater. Process. Technol.* 209:241–270.
11. Nandan R. Roy GG. Debroy T. (2006)." Numerical Simulation of Three-dimensional Heat Transfer and Plastic Flow During Friction Stir Welding". *Metall. Mater. Trans.* 37A:1247–1259.
12. Nandan R. Roy GG. Lienert TJ. Debroy T. (2006)." Numerical Modeling of 3D plastic flow and Heat Transfer During Friction Stir Welding of Stainless Steel". *Sci. Technol. Weld. Joining* 11:526–537.
13. Chen CM. Kovacevic R. (2003)." Finite Element Modeling of Friction Stir Welding Thermal and Thermomechanical Analysis". *Int. J. Mach. Tools Manuf.* 43:1319–1326.
14. Buffa G, Hua J, Shivpuri R, Fratini L (2006)." A Continuum Based FEM Model for Friction Stir Welding Model Development". *Mater. Sci. Eng* 419:389–396.
15. Rajesh SR. Bang HS. Chang WS. Kim HJ. Bang HS. Oh CI. Chu. JS. (2007)." Numerical Determination of Residual Stress in Friction Stir Weld Using 3D-analytical Model of Stir Zone". *J. Mater. Process. Technol.* 187–188:224–226.
16. Peel M. Steuwer A. Preuss M. Withers. PJ. (2003) "Microstructure, Mechanical Properties and Residual Stresses as A function of Welding Speed in Aluminum AA5083 Friction Stir Welds". *Acta. Mater.* 51:4791–4801.
17. Heurtier et al., 2006 P. Heurtier, M.J. Jones, C. Desrayaud, F. Montheillet, D. Alleaux and J. Driver, (2006) "Mechanical and thermal modeling of friction stir welding", *J. Mater. Process. Technol.* 172, pp. 152–158.1
18. Mohamed Assidi, Lionel Fourment, Simon Guerdoux, Tracy Nelson (2010)" Friction Model for Friction Stir Welding Process Simulation: Calibration From Welding Experiments" *International Journal of Machine Tool Manufacture* (50) 143–155.
19. Mohammad R. & Hamidreza N. (2011) "Analysis of Transient Temperature and Residual Thermal Stresses in Friction Stir Welding of Aluminum Alloy 6061-T6 Via Numerical Simulation" *Int. J. Adv. Manuf. Technol.* 55:143–152.
20. Key to steel data base version (2007.5).
- 21."Properties and Selection: Non-Ferrous Alloys and Special Purposes Materials", ASM Handbook, American Society for Metals, Vol. 2, 1992.
22. Manthan Malde (2009)" Thermomechanical Modeling and Optimization of Friction Stir Welding" MS.c Thesis, Osmania University, Hyderabad, India.
23. ANSYS® Release 12.0 Documentation, ANSYS Inc, 2009.
24. Yousif, Mohammed Akab, (2006) "Investigation of Mechanical and Microstructural Characteristic of Friction Stir Welded Joints." Ph.D. Thesis, University of Baghdad.
25. Muhsin Jabir Jweeg ,Sarmad Dhia Ridha (2010) "An investigation of friction stir welding and stress relief by vibration of 6061-T6 aluminum alloy" Ph.D. Thesis, University of Baghdad.
26. Zhu, X.K. and Chao, Y.J., (2004) "Numerical Simulation of Transient Temperature and Residual Stresses in Friction Stir Welding of 304L Stainless Steel", *Journal of Materials Processing Technology*, 146(2): p. 263-272.
28. Hansson, Sofia, "Simulation of Stainless Steel Tube Extrusion" Luleå University of Technology,



- Sweden, 2006.
28. Dixon, John, Burkes, Douglas and Medvedev, Pavel, (2007) "Thermal Modeling of A Friction Bonding Process" Proceedings of the COMSOL Conference ,Boston,.
29. Seidel, T.U. and Reynolds, A.P. (2001) "Visualization of the Material Flow in AA2195 Friction-Stir Welds Using a Marker Insert Technique." Metallurgical and Materials Transactions A, Vol. 32A, pp 2879-2884.
30. Nandan, R., Roy, G.G., and Debroy, T., (2006) "Numerical Simulation of Three-Dimensional Heat Transfer and Plastic Flow during Friction Stir Welding." Metallurgical and Materials Transactions A Vol. 37A, pp 1247-1269.
31. A. Arora, R. Nandan, A.P. Reynolds and T. Debroy. (2009)" Torque, power requirement and stir zone geometry in friction stir welding through modeling and experiments" Scripta Materialia (60) 13-16.
32. H. Jamshidi Aval & S. Serajzadeh & A. H. Kokabi (2011) "Theoretical and experimental investigation into friction stir welding of AA 5086 "Int. J. Adv. Manuf. Technol. 52:531–544.

**Nomenclature** $\rho$  Density ( $\text{kg}/\text{m}^3$ ) $c_p$  Specific heat capacity ( $\text{J}/\text{kg}^\circ\text{k}$ ) $k$  Thermal conductivity ( $\text{w}/\text{m}^\circ\text{k}$ ) $T$  Temperature ( $^\circ\text{k}$ ) $T_o$  Ambient temperature ( $^\circ\text{k}$ ) $\epsilon$  emissivity $\sigma$  Stefan –Boltzmann ( $\text{w}/\text{m}^2 \text{ }^\circ\text{k}^4$ ) $\mu$  Friction coefficient $P$  Contact pressure ( $\text{N}/\text{m}^2$ ) $\omega$  rotation speed (rpm) $V_t$  travel speed (mm/min) $\delta$  Slip factor $R_s$  shoulder radius (mm) $R_p$  pin radius (mm) $L_p$  pin length (mm) $Q_s$  Friction heat shoulder (w) $Q_p$  Friction heat pin (w) $Q_T$  Total heat generation (w) $i$  Time step $t$  Time (s) $\Delta t$  Time change (s) $Q_{int}$  Heat generation ( $\text{w}/\text{m}^3$ ) $F$  radiative view factor $\beta$  convection coefficient $\beta_b$  fictitious convection coefficient $\beta_{bo}$  is the heat transfer parameter for the bottom surface



## The Identity of Future Cities

( )

( )

## Scenarios of the City Future

### ABSTRACT:

In order to determine The Identity of Future Cities, the architecture does not provide us with one of the most basic needs (shelter), but also tangible evidence of the past and present as part of the communication, and best is an indicator of the future. Most of the narratives of the transformations of urban in twenty one century agreed that the city changed from an industrial society, the dominant over the previous century, to a pattern dominated by knowledge, information and communications, especially those that are remote and penetrated into the urban fabric, which produced the perceptions about the nature of identity, urban cities of the future, focusing Alternative research efforts of the city's future on the role of modern communications, transportation, and the structure of intelligence in the formation of new cities and an end to the old cities, this is one of the main problems faced by our cities, including present day Baghdad specifically.

This study aims to provide schematic design study of what should be the city of Baghdad as an Arab Islamic future and determine its dimensions and the strategic requirements. The city is formed according to the current strategy, based on traditional concepts, the research indicates that this method of urban planning today, witnessed by the city did not meet the requirements of the city of tomorrow based on physical, social, religious, economic, fundamentals. Different human activities are concerned with production and use of information and knowledge in the development of an influential architectural style and structures that underlie the functions of urban lifestyles and social groups.

The research suggests reconsideration of strategic plans on which the cities (including schemes of Developed Baghdad), which aspires to be humanitarian cities present the new and the coming future. Through the adoption of strategic schemes stemming from the Islamic thought, dynamism is poised to accommodate future multi scenarios.

: \_\_\_\_\_  
: \_\_\_\_\_  
: \_\_\_\_\_

: ( ) - ) ( ...

( ) ) . (226 1981

) 1964 ( 1966  
1967 1968



(2009 ) .

:( ) -

1945

1947

1948

1966

2000 )  
(1967 600  
19662000 1990 )  
(2005

1982

2000

:(2009 )  
:( ) .1:( ) .2 )  
( ( ) - )

(2009 ) .

.(1981 6 ) . : ( ) -

.( )

.(1981 6 ) . )

: -4 .(

" " " " "  
" " " " "

**" Multidisciplinary "**

McLoughlin

Physical Planning

(1)

(2)

(McLoughlin, 1973, P.84)

(3)

(4)

(5)

Cyclic Processing

(6)

**Information collective** (1)  
: survey

**Information analysis** (2)  
**: Formulation of goals** (3)

:Feed back

(11

)

(

McLoughlin, 1973, )

.(P.103

**Identification of**

(4

**.objectives**

(5

Context Conditions

**Preparation of alternative expected  
:strategies**

:(2007

)

Enjoyability

\*

**Preparation of**

(6

**.alternative unexpected strategies**

**:Evaluation**

(7

Propensity to

\*

Internationalization

(

Training

\*

**Preparation of scenarios**

(8

(9

**:Implementation**

Interactivity

\*

Compatibility

\*

**Monitoring and**

(10

Dynamism

\*

**:review**

Flexibility

\*

(McLoughlin, 1973, PP.102-103)



-5

- )  
« » " : ١(

(2008 ) ! » : .«

( ) (2008 )

)

.(

.1

.2

.3

.1

.2

.3

.4

.5

.6

.1

**2040**

(2008 ) :

(2007 )  
.2

.(%10 ±)

.3

.4

(92 2001 ) .

.1 (%10 ±)

• (2007 )  
• :  
• ( ) .5

( )  
( )

.( )  
. ( )

(%10 ±)

(2007 ) .

(110 2009 ) .



.2

) "2020"

(2008

)

(110 2009

( )

.3

.4

.5

(2008 ) .

( )

-6

( )

• ) .  
(2008

• : .

( )

: (1 )

( )  
) .

(2008

•  
•  
•  
•  
• ) .  
• ( .  
•  
•  
•  
• (2008 ) .

) : .  
(2008

Strength - (SWOT)  
Weakness  
Threats Opportunities



) : ( : -7

) (

) ( )

(Alexander) ( )

(A City Is Not )  
A Tree) ( .( )

.(17 1998 ) .

(... )  
( )

(Broadbent, 1990, p144) .

( ) ( )  
: ( )  
: .1

: .2 : -

(Broadbent, 1990, p.143) .

## Metropolitan City

-8

.(1 ) (2 )

) : ( )  
(2007 ) 29.682 (

11.444

(2030 ) 63.025 )

A

# **Prediction for Baghdad City of the Future**

## **SWOT**

### **:Strength**

(Alexander)

### **:Weakness**

- .(Alexander, 1987, p93) ( )  
• : -



## SWOT

)

(

**:Opportunities**

Organizational Integration

)

(

)

GIS

**:Threats**

)

(2030

( )

**:City structure**

.1





Transportation & Movement Network	.5	(2050 )
Communication Network	.6	
City structure	.1	
Population densities	.7	
Environmental impact	.8	Urban sprawl – urban growth .2
Social life	.9	
Land uses	.3	
City management	.10	Urban structure .4

.1

**Infrastructure & energy**

.11

.2

**:Planning method**

.12

.3

**:Historical City Center**

.13

-9



( )

• )  
- - ( )  
• )  
- ( )  
• )  
- ( )  
• )  
- ( )

.2008 : \_\_\_\_\_ :

•

\_\_\_\_\_ :

•

http://www.alsabaah. 2009 \_\_\_\_\_  
com/paper. php? source= akbar&mlf=  
interpage&sid=10617

•

\_\_\_\_\_ :

.1998

\_\_\_\_\_ :

•

\_\_\_\_\_ :

263

\_\_\_\_\_ :

.2001

\_\_\_\_\_ :

•

.2008 : \_\_\_\_\_

•

\_\_\_\_\_ :

.2007

\_\_\_\_\_ :

•

.2008

\_\_\_\_\_ :

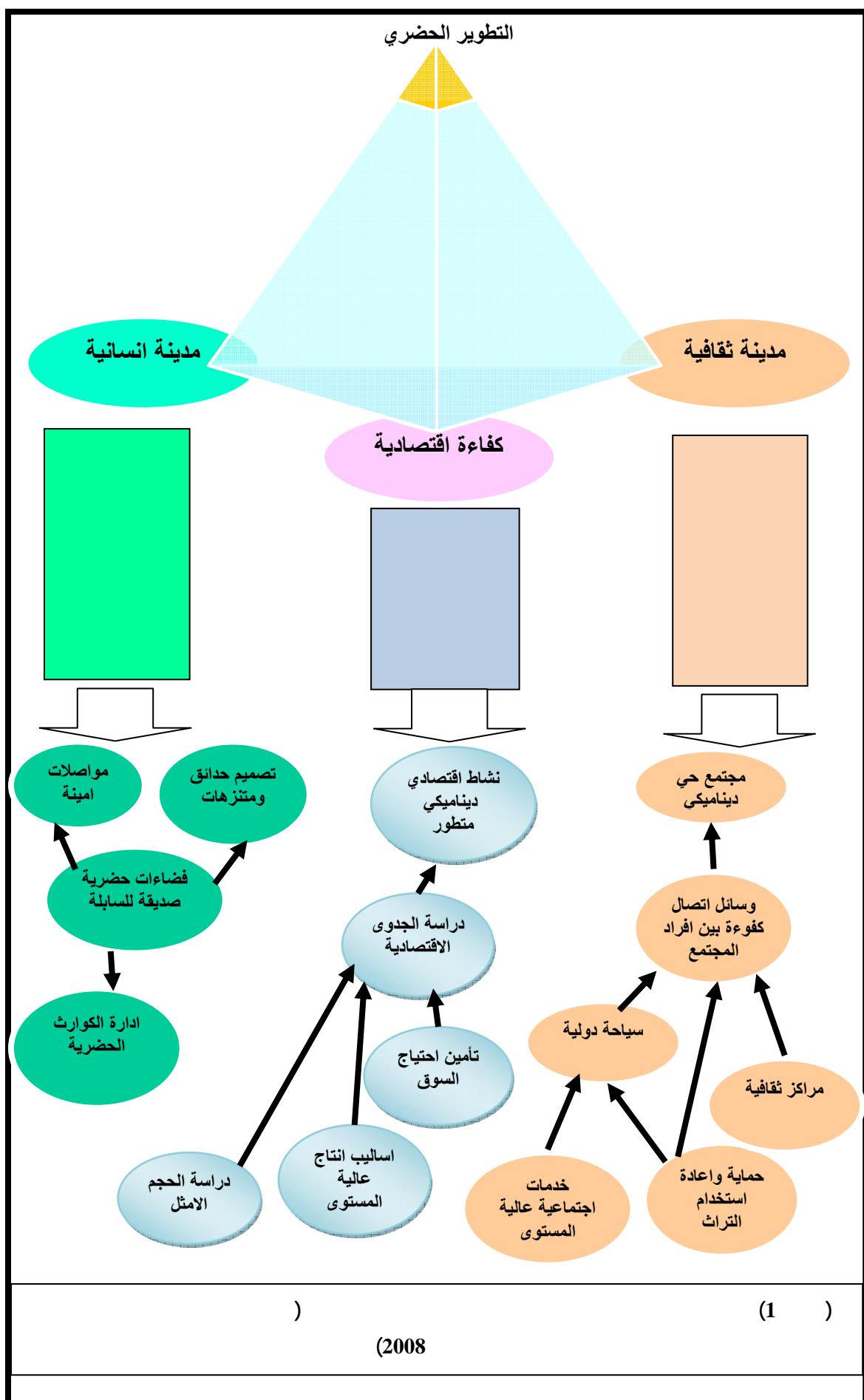
•

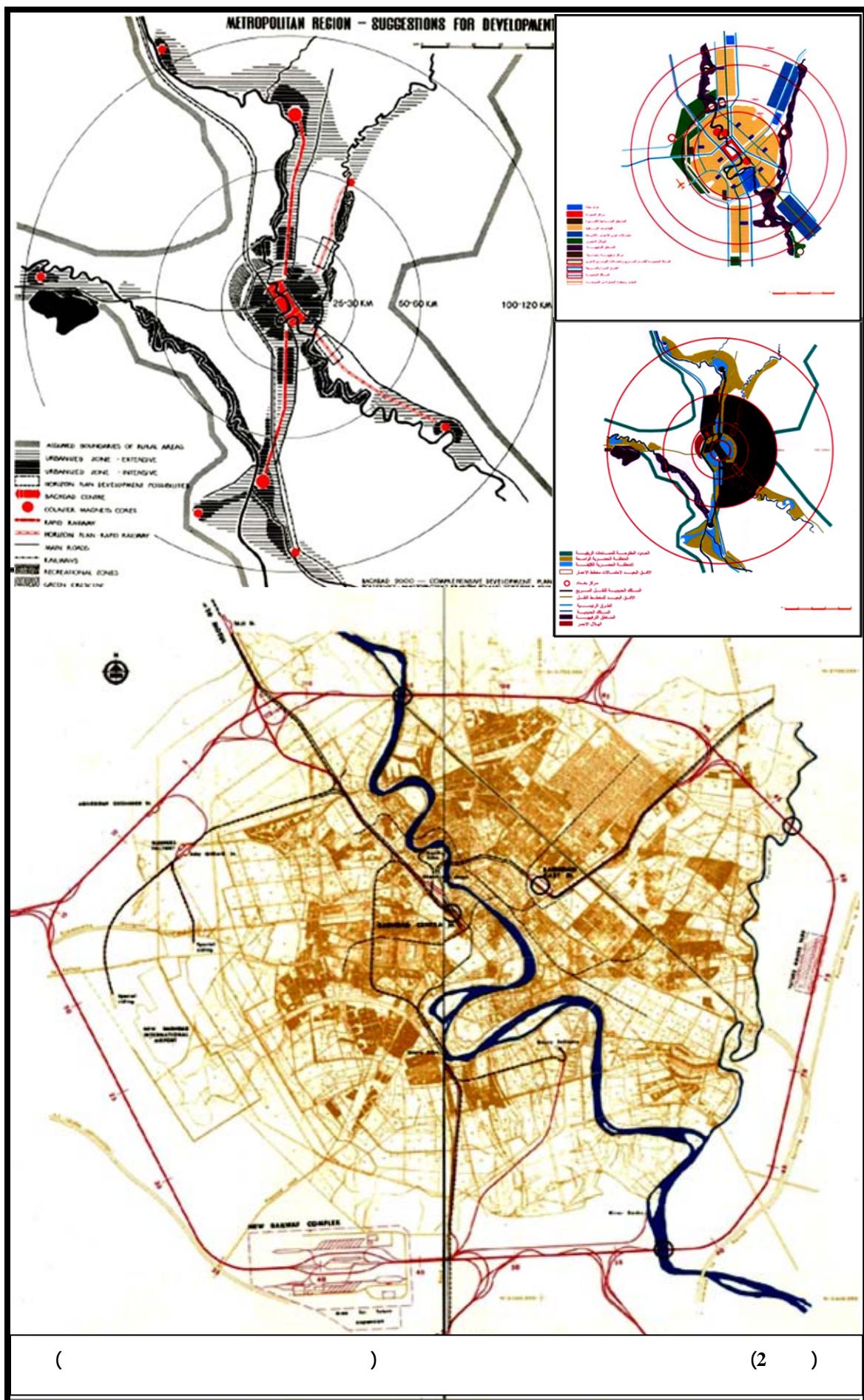
- Alexander, Christopher; **Anew Theory of Urban Design**; Oxford University Press; N.Y., USA, 1987.
- Broadbent, Geoffrey; **Emerging Concepts in Urban Space Design**; Van Nostrand Reinhold, London, 1990.
- McLouglin. J. B.; **Urban and Regional Planning- A system Approach**; Faber and Faber ltd, London, 1973.

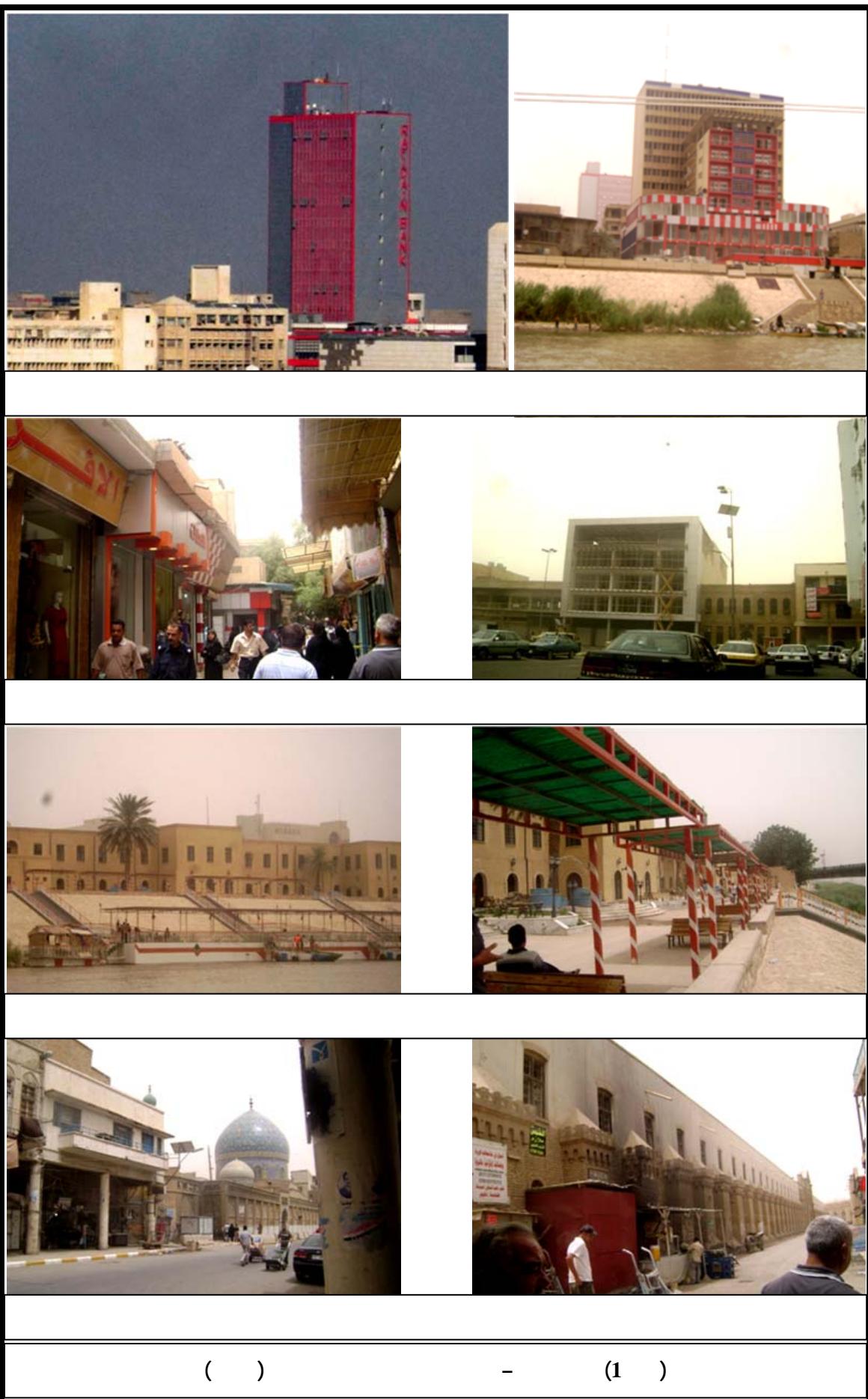
\_\_\_\_\_ :

•

.1981







( )

- (1 )



## Comparative Biosorption Of Pb(II), Cr(III) AND Cd(II) Ions In Single Component System By Live And Dead Anaerobic Biomass, Bath Study

Abbas H. Sulaymon,  
Baghdad University,

Shahlaa E. Ebrahim and  
College of Engineering,

Mohanad J. Mohammed Ridha  
Environmental Engineering Department

### ABSTRACT

In this study, dead and live anaerobic biomass was used in biosorption of Pb(II), Cr(III) and Cd(II) ions from a synthetic wastewater. The biosorption was investigated by batch adsorption experiments. It was found that, the biosorption capacities were significantly affected by biosorbent dosage. The process follows Langmuir isotherm (regression coefficient 0.995, 0.99 and 0.987 for Pb(II), Cr(III) and Cd(II) ions, respectively, onto dead anaerobic biomass) model with uniform distribution over the biomass surface. The experimental uptake capacity was 51.56, 29.2 and 28 mg/g for Pb(II), Cr(III) and Cd(II), respectively, onto dead anaerobic biomass, compared with 35, 13.6 and 11.8 mg/g for Pb(II), Cr(III) and Cd(II), respectively, onto live anaerobic biomass. The percentage reductions of live compared with dead anaerobic biomass in uptake capacity were 32.3, 53.4 and 57.8 for Pb(II), Cr(III) and Cd(II), respectively. The results indicated that, the dead anaerobic biomass is suitable as an efficient biosorbent for the removal of Pb(II), Cr(III) and Cd(II) ions from wastewater.

**Keywords:** Wastewater, Heavy metal, Live / dead anaerobic biomass, Biosorption, Isotherm

### الخلاصة

تم استخدام الكتلة الحيوية اللاهوائية الميتة والحياة في عملية الامتاز الحيوي لایونات عناصر الرصاص، الكروم الثلاثي والكادميوم من مياه الصرف. تم التحري عن الامتاز الحيوي بواسطة تجارب نظام الدفعة. وجد ان قابلية الامتاز الحيوي تتأثر بشكل واضح بواسطة كمية المادة الحيوية المستعملة. عمليات الامتاز الحيوي اتبعت موديل Langmuir مع معامل اندار 0.995، 0.99 و 0.987 لكل من ايونات الرصاص، الكروم الثلاثي والكادميوم على الكتلة الحيوية اللاهوائية الميتة مع توزيع منتظم على سطح الكتلة الحيوية. كانت قدرة الامتاز التجريبية 51.56، 29.2 و 28 mg/g لایونات الرصاص، الكروم الثلاثي والكادميوم على الكتلة اللاهوائية الميتة مقارنة مع 35، 13.6 و 11.8 mg/g لایونات الرصاص، الكروم الثلاثي والكادميوم على الكتلة اللاهوائية الحية. كانت النسبة المئوية لانخفاض قدرة الامتاز الكتلة اللاهوائية الحية مقارنة مع الكتلة اللاهوائية الميتة 32.3، 53.4 و 57.8 لایونات الرصاص، الكروم الثلاثي والكادميوم على التوالي. النتائج بينت انه الكتلة الحيوية اللاهوائية الميتة مناسبة بشكل فعال لازالة ايونات الرصاص، الكروم الثلاثي والكادميوم من مياه الفضلات.

**الكلمات الرئيسية:** مياه الصرف، معادن ثقيلة، كتلة حيوية اللاهوائية حية/ ميتة، الامتاز الحيوي، التمثيل الرياضي

## 1. INTRODUCTION

Presence of heavy metals in wastewaters causes significant environmental problems. High concentrations of heavy metals are known to be toxic and carcinogenic to living organisms. When heavy metals are present even in a very low concentration, their concentration may be elevated through bio-magnification to a level that they start to exhibit toxic characteristics. The metals which are of greatest environmental concern are cadmium, mercury, lead, chromium, cobalt, copper, nickel and zinc, (Sahmoune et al., 2009). Metals are non-renewable from the point of resource and recovery, and important from the point of contaminants in water and wastewater; Different methods are used for the removal and recovery of heavy metals, (Spearot and Peck, 1984). Chemical methods, to effectively decrease heavy metals to acceptable levels require a large excess of chemicals, which increase the costs because of generating the voluminous sludge, (Yun and Volesky, 2003). In the meantime, biosorption of heavy metals from aqueous solutions is a relatively new technology for the treatment of industrial wastewater. The major advantages of biosorption technology are their effectiveness in reducing the concentration of heavy metal ions to very low levels and the use of inexpensive biosorbent materials (Naja, and Volesky, 2006). It is important for a biosorption process to select the most available and reliable biosorbent, (Liu et al., 2003). Both live and dead biosorbent, is derived from suitable biomass can be used for the effective removal and recovery of heavy metal ions from wastewater streams; These include bacteria, fungi, yeast and marine algae (Huifen et al., 2010). Because of the many problems inherent in maintaining active microbial populations under highly variable conditions of wastewaters, living systems are often unreliable, while non-living form, can serve as a basis for development of biosorbent materials for the efficient removal of heavy metals (Puranik et al., 2005). The use of living organisms may not be an option for the continuous treatment of highly toxic organic/inorganic contaminants, once the toxicant concentration becomes too high or when the process is operated for a long time. The amount of toxicant accumulated inside the organisms will reach saturation, beyond this point; an organism's

metabolism may be interrupted, resulting in death of the organism (Vijayaraghavan and Yun, 2008). Another advantage of using dead biomass is, the sorbed metal ions can be easily desorbed and the biomass can be reused (Liu et al., 2003). The capacities of many biosorbent were found to be much higher than those of other types of adsorbents, activated carbon, natural zeolites and synthetic ion exchange resins, (Sheng, 2004), because the cell walls of these types of biosorbents contain polysaccharides and proteins having various functional groups such as amine, carboxyl, hydroxyl, sulphates, and phosphates responsible for interacting with the metals ions and dyes (Sahmoune et al., 2009). Das et al., 2007 investigated the removal of heavy metals by dead biomass in batch experiments at different pH values ranging from 3-8. The results indicated that, maximum adsorption of different metal species occurred at pH values of 4. Different models are to be developed from simple mathematical relationships, characterized by a limited number of adjustable parameters, which give a good description of the experimental behavior over a large range of operating conditions. The model used to describe the results should be capable of predicting heavy metal binding at both low and high concentrations (Vijayaraghavan and Yun, 2008). One of these models is the Langmuir isotherm model which can be represented as:

$$q_e = \frac{q_{\max} b C_e}{(1 + b C_e)} \quad (1)$$

Where:  $q_e$ (mg/g), the amount of adsorbate adsorbed per mass of adsorbent of component;  $q_{\max}$  (mg/g), corresponds to the maximum achievable uptake by a system;  $b$  (l/mg), is related to the affinity between the sorbate and sorbent, and  $C_e$ (mg/l) is the final metal ions concentrations in the solution. The Langmuir model assumes that the adsorption is limited to a monolayer. The important characteristic of the Langmuir isotherm can be expressed in terms of the dimensionless constant separation factor for equilibrium parameter  $R_L$ . This is defined by: (Sahmoune et al., 2009)

$$R_L = \frac{1}{b + C_e} \quad (2)$$



The parameter  $R_L$  indicates the shape of the isotherm as shown in **Table 1**.

Table 1 Constant parameter  $R_L$

Another model is the Freundlich isotherm model, represented as: (Vijayaraghavan and Yun, 2008)

$$q_e = KC_e^{1/n} \quad n > 1 \quad (3)$$

It incorporates two constants: K (mg/g)/(mg/l)<sup>1/n</sup>, which corresponds to the maximum binding capacity; and n, characterize the affinity between the sorbent and sorbate (adsorption intensity). The Freundlich isotherm model assumed that the adsorption is a multilayer, was originally empirical in nature, but was later interpreted as the sorption to heterogeneous surfaces or surfaces supporting sites with various affinities.

The Sips isotherm model can also represents the adsorption process:

$$q_e = \frac{K_s C_e^{\beta_s}}{1 + a_s C_e^{\beta_s}} \quad (4)$$

$K_s$ , is the Sips model isotherm constant;  $a_s$ , the Sips model constant; and  $\beta_s$ , the Sips model exponent Langmuir–Freundlich isotherm which derive from the limiting behavior of the equation (4), at low sorbate concentrations it effectively reduces to a Freundlich isotherm and thus does not obey Henry's law. While at high sorbate concentrations, it predicts the monolayer sorption capacity characteristics of the Langmuir isotherm (Huifen et al., 2010). The role of different physicochemical parameters associated with the sorption of lead, chromium and cadmium ions from aqueous solution by live/dead anaerobic biomass through batch method is described to compare between the biosorption capacity of dead and live anaerobic biomass for removal of these metals.

## 2. MATERIAL AND METHODS

### 2.1 Materials (Stock Solutions)

A stock solution of lead, chromium and cadmium ions with a concentration of (1000 mg/l) were prepared by using Pb(NO<sub>3</sub>)<sub>2</sub>, Cr(NO<sub>3</sub>)<sub>3</sub> and Cd(NO<sub>3</sub>)<sub>2</sub> ( BDH, England with minimum purity 99.5%). A 0.1599, 4.577 and 2.103 g of lead nitrate, chromium nitrate and cadmium nitrate, respectively were dissolved in 1000 ml distilled water. Dissolved metal concentrations in solution were determined by a flame atomic absorption spectrophotometer (AA) (Buck, USA).

## 2.2 Preparation of Biosorbent

Heterogeneous cultures including mostly anaerobic bacteria, yeast fungi and protozoa of sorbents were taken from Al-Rostomia'a third extension drying bed. Anaerobic and facultative anaerobic microorganisms (*Aeromonas species*, *E-coli*, *Pseudomonas aeruginosa*, *Clostridium*, *Staphylococcus sp* and *Salmonella sp*) were found in the sludge taken from the drying beds.

### 2.2.1 Live anaerobic biomass (LAB)

A mixed culture of anaerobic bacteria, yeast and fungi were grown in laboratory for 30 days. Nutrients were added as a soluble organic mixture. Growth media contains: 13.34, 4, 0.4, 12.5 and 37 g of Glucose, Peptone, K<sub>2</sub>HPO<sub>4</sub>, NaHCO<sub>3</sub>, and Na<sub>2</sub>SO<sub>4</sub>, respectively, trace metals 0.12, 0.78, 0.04, 0.04 and 0.045 g of CoCl<sub>2</sub>.6H<sub>2</sub>O, FeCl<sub>2</sub>.4H<sub>2</sub>O, MnCl<sub>2</sub>.4H<sub>2</sub>O, NaMoO<sub>4</sub>.2H<sub>2</sub>O and NiCl<sub>2</sub>.6H<sub>2</sub>O were dissolved in 5 liters of distilled water, pH was controlled to be neutral by adding 0.1M NaOH or 0.1M HNO<sub>3</sub>, temperature was fixed to be 37°C using a heater and thermostat.

### 2.2.2 Dead Anaerobic Biomass (DAB)

Heterogeneous culture of live anaerobic biomass (LAB) was dried at atmospheric temperature (37–45°C) for 5 days crushed, sieved, washed with distilled water and dried at 70°C for 6 h. The geometric mean diameter was obtained to be 0.775 mm.

## 2.3 Batch Biosorption Experiments

Different weights of live/dead anaerobic biomass were used, (0.05, 0.1, 0.15, 0.2, 0.25, 0.3, 0.35, 0.4, 0.45, 0.5, 0.55, and 0.6) g wet/dry basis by electronic balance (Sartorius BL 210S); biosorbents were placed in 12 volumetric flasks of 250 ml. A sample of 100 ml of measured concentration solution of 50 mg/l was added to each flask for single systems of Pb(II), Cr(III) and Cd(II) ions respectively. The experiment was performed at sufficiently high metal concentrations so that maximal uptake would be achieved. The pH of the metal solutions was adjusted to the desired value (pH=4) using 0.1M NaOH or 0.1M HNO<sub>3</sub>. The flasks were then placed on a shaker (HV-2 ORBTAL, Germany) and agitated continuously for 4 h at 200 rpm and (33±3°C). The samples were filtered by 42 Whatman filter paper, few drops of 0.1M HNO<sub>3</sub> were added to the samples to decrease the pH value below 2 in order to fix the concentration of the heavy metals during storage before analysis (APHA, 1995). The final equilibrium concentrations were measured by means of an atomic absorption device (AA). The adsorbed amount was then calculated by the following equation:

$$q_e = \frac{V(C_0 - C_e)}{W(\text{wet/dry base})} \quad (5)$$

$q_e$  (mg/g), is the amount of heavy metals ions uptake by (LAB/DAB),  $C_0$ (mg/l) and  $C_e$ (mg/l), are the respective initial and final metal ion concentrations in the solution, respectively,  $V$  (l), is the volume of solution and  $W(g)$ , is the weight of the biomass. The adsorption isotherms were obtained by plotting the weight of solute adsorbed per unit weight of biomass ( $q_e$ ) against the equilibrium concentration of the solute in the solution ( $C_e$ ) (Vijayaraghavan and Yun, 2008).

### 3. RESULTS AND DISCUSSION

The obtained data for single component systems were correlated with the Langmuir, Freundlich and Sips isotherm models. The parameters for each model obtained from non-linear statistical fit of the equation to the experimental data (Statistica-v6). **Table 2** shows parameters of single solute isotherm for Pb(II), Cr(III) and Cd(II) ions uptake onto live and dead anaerobic biomass. Biosorption capability

of dead and live anaerobic biomass (DAB/LAB) for the metal ions Pb(II), Cr(III) and Cd(II) were compared individually. **Fig.1** to **Fig. 3** show that the Langmuir isotherm model was found to be favorable,  $R_L$  was found between 0 and 1 for Pb(II), Cr(III) and Cd(II) ions for both dead and live anaerobic biomass.

Fig.1. Biosorption isotherm of lead ions onto dead and live anaerobic biomass

Fig.2. Biosorption isotherm of chromium ions onto dead and live anaerobic biomass

Fig.3. Biosorption isotherm of cadmium ions onto dead and live anaerobic biomass

Table 2 Parameters of single solute isotherm for Pb(II), Cr(III) and Cd(II) ions for live and dead anaerobic biomass.

**Fig.4**, shows the experimental uptake capacity was 51.56, 29.2 and 28 mg/g for Pb(II), Cr(III) and Cd(II), respectively, onto dead anaerobic biomass (DAB), compared with 35, 13.6 and 11.8 mg/g for Pb(II), Cr(III) and Cd(II), respectively, onto live anaerobic biomass (LAB). The percentage reductions of live compared with dead in uptake capacity were 32.3, 53.4 and 57.8 for Pb(II), Cr(III) and Cd(II), respectively.

Fig.4. Maximum experimental uptake capacity for Pb(II), Cr(III) and Cd(II) onto live and dead anaerobic biomass.

Results can be compared for the three adsorbates in terms of adsorption capacity parameters: Pb(II) > Cr(III) > Cd(II). Since lead nitrate salt is less soluble in water in comparison with chromium nitrate and cadmium nitrate salts (solubility of salts in water are 52, 81 and 136 g/100 ml for Pb(II), Cr(III) and Cd(II) ions). It will be expected to have a highest biosorption rate. The lead which has the highest affinity order for being adsorbed by the biomass, has the lowest hydration radius (4.01, 4.13 and 4.26 Å for Pb(II), Cr(III) and Cd(II)) while cadmium ion the least favorable by the biomass, has the highest hydration radius. This coincides with the fact that less hydrated ions radius are preferably accumulated at interface (Hawari and



Mulligan, 2006). Fig.5, shows that the removal efficiency was 99.14, 97.67 and 93.63 percent for Pb(II), Cr(III) and Cd(II) ions, respectively, onto dead anaerobic biomass, while it was 88.56, 79.8 and 78.56 percent for Pb(II), Cr(III) and Cd(II) ions, respectively, onto live anaerobic biomass. It was demonstrated that a concentration of 6 g/l of biomass for both dead and live anaerobic biomass could achieve very good removal efficiency when the solution concentration was 50 mg/l for Pb(II), Cr(III) and Cd(II) ions. These results encourage using the dead biomass in all the following experimental work as biosorbent.

Fig.5. Maximum removal efficiency for Pb(II), Cr(III) and Cd(II) onto live and dead anaerobic biomass

Similar results were found when dead biomass of different types to be a more efficient biosorbent of heavy metals (Huifen et al., 2010). The difference between live and dead anaerobic biomass can be explained on the basis of active metabolizing cells plasma membrane generating competing H<sup>+</sup> ions (Yun and Volesky, 2003). Alternatively, in dead state, the cells become more porous and allow the metal to enter and bind to the internal surfaces and functional groups as well, thus increasing metal biosorption (Liu et al., 2003). The uptake by live anaerobic biomass occurs by precipitation and transport across cell membrane and accumulation inside the cells, while by dead anaerobic biomass, it depends on precipitation, physical adsorption, ion exchange and complexation (Hawari and Mulligan, 2006). Another reason demonstrates the cause of uptake is higher by dead than live anaerobic biomass is due to the difference in surface area per unit mass of dead and live biomass. Dead biomass has higher surface area per unit mass compared with live biomass due to 70% total weight of the cell is water, thus by drying the biomass into pellets the surface area of a unit weight will increase. Therefore, to overcome the disadvantages of using live anaerobic biomass, dead biomass was recommended for heavy metals removal.

#### 4. CONCLUSIONS

Uptake capacity by dead anaerobic biomass (DAB) is greater than the uptake capacity of live anaerobic biomass (LAB) for Pb(II), Cr(III) and Cd(II) ions. In single system Pb(II) ions was the most favourable component rather than Cr(III) and Cd(II) ions. This is due to its physicochemical characteristics that makes it the most favourable adsorbed component, due to less solubility and highly molecular weight. Results for the three adsorbates in term of adsorption capacity parameters was: Pb(II) > Cr(III) > Cd(II).

#### 5. REFERENCES

- APHA, 1995, "Standard methods for the examination of water & wastewater", 19th Edition, American Public Health Association, Washington, DC.
- Das, N., Charumathi, D., Vimala, R., 2007, "Effect of pretreatment on Cd(II) biosorption by mycelial biomass of Pleurotus florida", African Journal of Biotechnology, 6 (22), 2555-2558.
- Hawari, H A., Mulligan N. C, 2006, "Biosorption of lead(II), cadmium(II), copper(II) and nickel(II) by anaerobic granular biomass", Bioresource technology, 97, 692-700.
- Huifen, L., Yanbing, L., Wumeng, G., Jiali C., Lin X., Junkang G., 2010, "Biosorption of Zn(II) by live and dead cells of Streptomyces cisaucasicus strain CCNWX 72-14", Journal of Hazardous Materials, 179, 151-159.
- Liu, Y., Yang, S., Xu H., Woon, K., Lin, Y., Tay, J., 2003, "Biosorption kinetics of cadmium (II) on aerobic granular sludge" Process Biochem., 38, 997–1002.
- Naja, G., and Volesky, B., 2006, "Behavior of the mass transfer zone in a biosorption column", Environ. Sci. Technol., 40, 3996-4003.
- Puranik, P., Modak, J., Paknikar, K., 2005, "A comparative study of the mass transfer kinetics of metal biosorption by microbial biomass", Hydrometallurgy, 52, 189–197.

Sahmoune, M., Louhab, K., Boukhiar, A., 2009, "Biosorption of Cr(III) from aqueous solutions using bacterium biomass *streptomyces rimosus*", Int. J. Environ. Res., 3(2), 229-238.

Sheng, P., 2004, "Sorption of Lead, Copper, Cadmium, Zinc and Nickel by Marine Algal Biomass: Characterization of Biosorption Capacity and Investigation of Mechanisms", Journal of Colloid and Interface Science, 275, 131-141.

Spearot, R. M., and Peck, J. V., 1984, "Recovery process for complexed copper-bearing rinse", Waters Environ. 3, 124-129.

Vijayaraghavan, K., Yun, Y-S., 2008, "Bacterial biosorbents and biosorption", Biotechnology Advances, 26, 266-291.

Yun, Y.S., and Volesky, B., 2003, "Modelling of lithium interference in cadmium biosorption", Environ. Sci. Technol., 37, 3601-3608.

Table 1 Constant parameter  $R_L$

$R_L$	Type of isotherm
$R_L > 1$	unfavorable
$R_L = 1$	linear
$R_L = 0$	irreversible
$0 < R_L < 1$	favorable

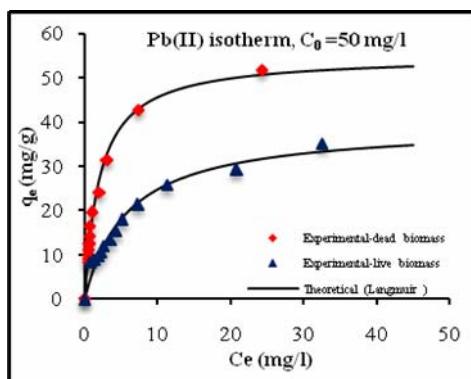


Fig.1. Biosorption isotherm of lead ions onto dead and live anaerobic biomass

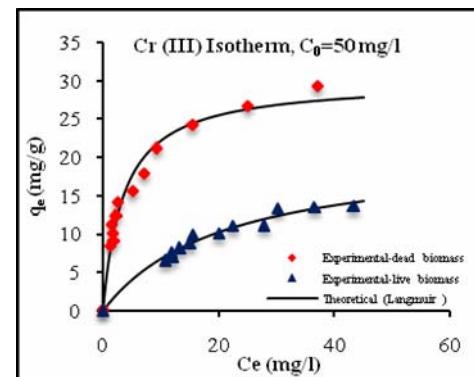


Fig.2. Biosorption isotherm of chromium ions onto dead and live anaerobic biomass

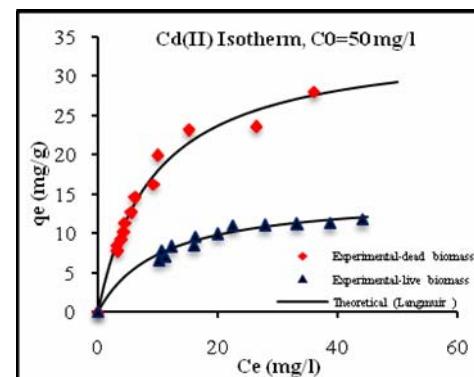


Fig.3. Biosorption isotherm of cadmium ions onto dead and live anaerobic biomass



Table 2 Parameters of single solute isotherm for Pb(II), Cr(III) and Cd(II) ions for live and dead anaerobic biomass

Model	Parameters	Pb(II)		Cr(III)		Cd(II)	
		Dead	Live	Dead	Live	Dead	Live
Langmuir	$q_{\max}$	54.92	39.3	34.78	20.32	29.99	14.9
	b	0.493	0.17	0.107	0.048	0.285	0.097
	$R_L$	0.036	0.13	0.212	0.506	0.104	0.409
	$R^2$	0.995	0.987	0.99	0.983	0.987	0.985
Freundlich	K	17.45	8.6	9.24	2.33	5.986	3.6
	n	2.73	2.43	3.02	2.06	2.26	3.07
	$R^2$	0.969	0.95	0.989	0.983	0.973	0.971
	$k_s$	25.89	8.54	10.02	0.663	2.45	0.773
Sips	$\beta_s$	0.895	0.63	0.594	1.199	1.317	1.13
	$a_s$	0.44	0.13	0.226	0.037	0.082	0.058
	$R^2$	0.986	0.98	0.984	0.981	0.982	0.891

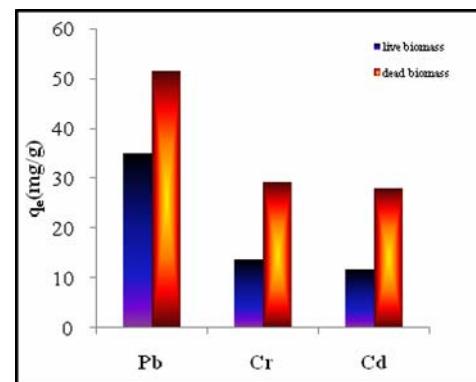


Fig.4. Maximum experimental uptake capacity for Pb(II), Cr(III) and Cd(II) onto live and dead anaerobic biomass

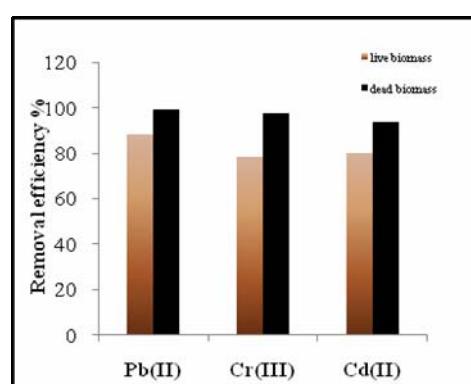
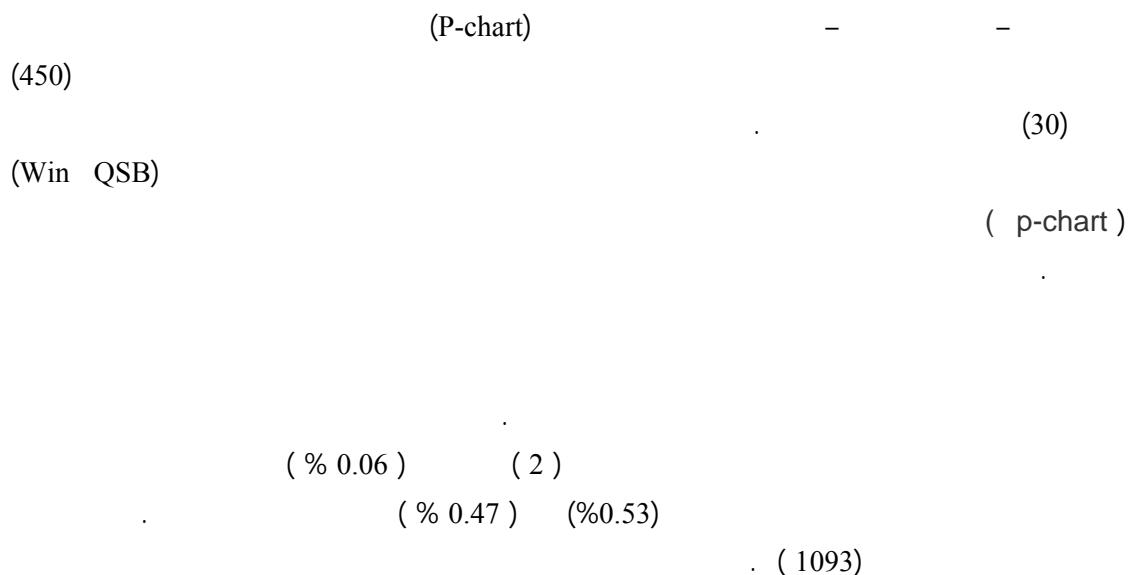


Fig.5. Maximum removal efficiency for Pb(II), Cr(III) and Cd(II) onto live and dead anaerobic biomass



- /



## Statistical Quality Control of Industrial Products at the General Company for Vegetable Oils

### Abstract

This research includes the using of statistical to improve the quality of can plastics which is produced at the state company for Vegetable oils (Almaamon factory) by using the percentage defective control chart ( p-chart ) of a fixed sample. A sample of size (450) cans daily for (30) days was selected to determine the rejected product. Operations research with a (win QSB) package for ( p-chart ) was used to determine test quality level required for product specification to justify that the process that is statistically controlled.

The results show high degree of accuracy by using the program and the mathematical operations (primary and secondary) which used to draw the control limits charts and to reject the statistically uncontrolled samples. Moreover a final chart was drawn to be used in the factory .

The research shows improvement of the can product by percentage (0.06 %), product defects percentage was lowered from ( 0.53 % to 0.47 % ) for the production process which becomes statistically controlled .Also it was found that it was within Iraqi specification (1093).

( D.H.Besterfield )

---

. [ 3 ]

( Frederick W.Taylor )

Scientific )

1911

( Maragement

. [ 4 ]

1924

( Walter A . Shewhart )

( )

. [ 5 ]

( Inspection Sampling Techniques )  
Acceptance )

( Sampling Plans

V.F.Dodge and H.G )

1944

( Roming

. [ 6 ]

Edward )

1950

( Deming

. [ 1 ]

( J.M.Juran 1999 )

. [ 2 ]  
Deming



[ 7 ]

. [ 10 ] ( Armand Fiegenbaum )  
( Total Quality Control )

. [ 8 ]

1961

(Xie and Goh. 1999 ) – 1 ( Quality Control Circles )

1980 1970

. ( )

Toquch ) Total )  
design of Experiments DoE ] ( Quality Management  
Failure Mode and ( ) . [ 6  
( FMEA ) Effects Analysis 1980  
Statistical ) ( Process Control

11 ] 1990

. [ ISO  
( Pankaj et al 2000 ) – 2 9000

Soft ware

. [ 9 3]

( Software )

Excel , Access , Sql Server , )

( Oracle , Text files

[ 16 ] Design of experiments

(        )

. [ 12 ] ( Web – Service )

( Oakland 2003      ) – 3

( Samipand Pandy 2010 )

[ 17 ]

. [ 14 13 ]

Chakraborti and Human ) – 4

( 2006

( P- Chart ) ( Parameter)

Random )

$f_{(P)}$  ( Variable

[ 18 6 ]

-1

P- Chart )

$f_{(P)}$

(

. [ 15 ]

( Judi et al 2009 ) – 5

-2

)

-3

-4

)

Quality function

six sigma

deployment

[ 20 19 ]



(30)

-

-1

(100)

-

(P)

-

)

(d)

:

( ...

. m

)

-

$$P_i = \frac{d}{m}$$

( x - chart

-

( R - chart )

-

)

-

P^-

-

( σ - chart

-2

$$P^- = \frac{\sum_{i=1}^n P_i}{n}, \quad P^- = CL$$

: m

( )

: n

:

: d

P

-

( Central Line )

: CL

. - chart

: P\_i

-

30 - 1

: i

. C - chart

-

:

. u- chart

3 ] (P-chart)

( Upper Control Limit )

[ 22 21

$$UCL(P^-) = P^- + 3 * \sqrt{\frac{P^- (1-P^-)}{m}}$$

P

( Lower Control Limit )

$$LCL(P^-) = P^- - 3 * \sqrt{\frac{P^- (1-P^-)}{m}}$$

)

.

$P_i$

( )

(3) ( 2 )  
 ) ( 30 ) ( p-chart )  
     ( 1  
     ( 450)  
 %100

2010 / 10 / 3 ) -1

) ( 2011 / 11 / 14 / \*  
     ( 3

[ 23 ] (1) 2

/ \_\_\_\_\_  
 1970 \_\_\_\_\_  
 . ( 2 ) : -  
 . ( 125 ) : -  
 . ( 5 ± ) : -  
 450 = -

)  
 )  
 / ( ) -1 (2) ( 4  
 / -2  
 / -3 ( ) -2  
 - -3

(Win QSB)

[ 25 24] P-chart

(Win QSB Package) ( 1 )



-3

-4

)

(

- 5

-

-4

[ 26 ] ( 1093)

---

[ 1 ] - Ganther , W.G 1977 , " Sampling  
Inspection in Statistic Quality control  
",charles ritten and Company Ltd ( -5  
London) .

(P- chart)

[ 2 ] - Joseph M.Juran and A.Blatan  
Godfrey 1999, "JURAN 'S QUALITY  
HAND BOOK ", 5<sup>th</sup> ed ,Mc Graw  
– Hill, INC .

[ 3 ] – Dale H.Besterfiel , 2009 , "Quality  
Control" ,8<sup>th</sup> ed Prentice- Hill , New Jersy .

-6

[ 4 ] – James R.Evans , 2011 , " Quality  
Management , Organization and Strategy ",  
6<sup>th</sup> ed South – Westen , Cengage Leaving  
International Offices (Canada )

---

[ 5 ] – V.A Kulkarni and A.K Bewoor ,  
2009 , " Quality Control " , 1<sup>st</sup> ed , Wiley  
India Pvt . Ltd , New delhi .

-1

-chart )

(P

[ 6 ] – B.Janakiraman and R.K.Gopal 2008  
, "Total Quality Management: Text and  
Cases " , Prentice – Hill of India Private  
limited, New Delhi .

[ 7 ] – V.K Khamna , prem , Vrat  
,B.S.Shahay and Ravi Shankay , 2008 ,  
"TQM Planning , Design and  
Implementation ",1<sup>st</sup> ed , New Age  
International (P) Ltd .

-2

(Win QSB)



[ 17 ] - Serope kalpagn , steven R. Schmid 2008 , " Manufacturing Processes for Engineering Materials " , 5<sup>th</sup> ed , prentice – Hill.

[ 18 ] – Doulges C. Montgomery 2005 , " Introduction to statistical quality control , 5<sup>th</sup> ed , USA – Willey .

[ 19 ] – William J, Steven son , 2007 , " Operations Management", 9<sup>th</sup> ed , Mc Graw – Hill, INC.

[ 20 ] – Marilyn K.Hart and Robert F.Hart 2007 , " Introduction to Statistical Process Control techniques " statit soft ware , Inc .

[ 21 ] – Vinay A.Kulkarni and Anand K . Bewoor . 2009 , " Quality control " , 1<sup>st</sup> ed , Wiley India Pvt.Ltd , New Delhi .

[ 22 ] – James R.Evans and William M . Lindsay 2011 , " The management and Control of Quality ", South – Westren , Cengage Learning ( Canada ).

[ 23 ] - دليل الشركة العامة للزيوت النباتية – مصنع المامون ، قسم المنظف السائل والشامبو – تعليمات العمل لقسم المنظف السائل ( الزاهي ) – آيار – 2006 .

[ 24 ] د. خالد ضاري الطائي ، مروان عبد الحميد العتيبي ، محمد ناصر العشاري ، 2009 "تطبيقات وتحليلات النظام الكمي للأعمال QSB-Win" -طبعة الذاكرة – بغداد .

[ 25 ] د. انعام عز الدين الصفار، صدى عبد الخالق الياسري ، 2009 "تحديد الانتاج الامثل في المعامل التشبيد (معمل سمنت الكوفة حالة دراسية) ، المؤتمر العلمي الثاني لكلية الهندسة – جامعة القادسية .

[ 26 ] المواصفة القياسية العراقية ( 1093 ) الصادرة عن وزارة التخطيط – الجهاز المركزي للتقدير والسيطرة النوعية . ( IQS 1093 : 1986 ) .

[ 8 ] – Feigenbaum A.V 1999 , "Total Quality Control " , 3<sup>th</sup> ed , Mc Gaw – Hill , Inc , NewYork .

[ 9 ] – N.S Sreenivasan and V.Narayana , 2005 , " managineg Quality Control Tasks " , 1<sup>st</sup> ed , New Age International (P)Ltd , New Delhi .

[ 10 ] – James R.Evans and William M . Lindsay 2011 " the management and Control of Quality ", South - Western Cengage learning .

[ 11 ] – Xie , m and T.N Goh , 1999 , " Statistical Techniques for Quality " the TQM magazine . vol 11 , no4 . pp234 -241 .

[ 12 ] – Pakaj Jalotc , Senior Member , IEEE and Ashish Aexena .2002 , "Optimum Control Limits for Employing Statistical Process Control in Soft ware Process " , IEEE Transactions on Soft ware Engineering . Vol ,28 , No.12 .

[ 13 ] – Oakland , J.S. 2003 , Statistical Process Control , 5<sup>th</sup> ed , oxford :Butter worth – Heine maun "

[ 14 ] – Shoh samip and shridher pandy , 2010 " Control Chart Astatistical process control tools in pharmacy " , Assian Journal of pharamaceutics , vol . 4 , no.3 , pp . 184 – 192 1

[ 15 ] – S.chakvabotriand and S.w Human , 2006 , " Parameter Estimation and Perofmane of the p-Chart for Attributes Data " , IEEE Transactions on reliability , vol . 55 , no.3 .

[ 16 ] - Hairulliza Mohamad Judi , Ruzzakian Jenal and Devendran 2009 , " Some Experiences of quality Control Implementaion in Malaysian Companies " , European Journal of Scientific Research , vol . 27 , no . 1 , pp .24 – 45 .

(

)

(

)

(

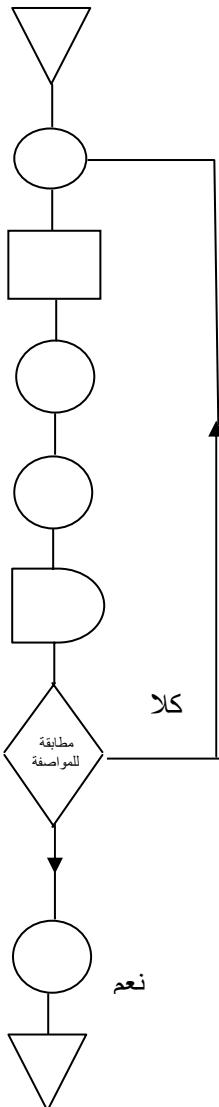
)

(

)

(

)



(1)

[ ] 2



(2)



(3)

الملاحظات	أنواع الفحوصات الفنية				المرفوض (d)	المقبول	حجم العينة	الوقت	تاريخها	رقم العينة
	المظهر	التشقق	النضوح	الوزن (غم)						
-	-	-	8	8	442	450	9:30-8:30	2010/10/3	1	
-	-	1	4	5	445	450	9:30-8:30	2010/10/4	2	
-	-	-	2	2	448	450	9:30-8:30	2010/10/5	3	
-	-	1	2	3	447	450	9:30-8:30	2010/10/6	4	
-	-	-	-	-	450	450	11:30-10:30	2010/10/7	5	
-	-	-	-	-	450	450	12:30-11:30	2010/10/10	6	
-	-	1	1	2	432	450	9:30-8:30	2010/10/11	7	
-	-	1	2	3	447	450	9:30-8:30	2010/10/12	8	
-	-	-	2	2	448	450	9:30-8:30	2010/10/13	9	
-	-	1	2	3	447	450	9:30-8:30	2010/10/14	10	
-	-	1	-	1	449	450	9:30-8:30	2010/10/17	11	
-	-	-	-	-	450	450	10:30-9:30	2010/10/18	12	
-	-	-	-	-	450	450	11:30-10:30	2010/10/19	13	
-	-	-	-	-	450	450	12:30-11:30	2010/10/20	14	
-	-	-	2	2	448	450	9:30-8:30	2010/10/21	15	
-	-	-	4	4	556	450	9:30-8:30	2010/10/24	16	
-	-	1	1	2	448	450	9:30-8:30	2010/10/25	17	
-	-	-	-	-	450	450	9:30-8:30	2010/10/26	18	
-	-	-	1	1	449	450	9:30-8:30	2010/10/27	19	
-	-	1	2	3	447	450	9:30-8:30	2010/10/28	20	
-	-	1	4	5	445	450	9:30-8:30	2010/11/1	21	
-	-	1	3	4	446	450	9:30-8:30	2010/11/2	22	
-	-	-	-	-	450	450	1:30-12:30	2010/11/3	23	
-	-	-	4	4	446	450	9:30-8:30	2010/11/4	24	
-	-	1	2	3	447	450	9:30-8:30	2010/11/7	25	
-	-	-	4	4	446	450	9:30-8:30	2010/11/8	26	
-	-	-	4	4	446	450	9:30-8:30	2010/11/9	27	
-	-	1	3	4	446	450	9:30-8:30	2010/11/10	28	
-	-	-	-	-	450	450	12:30-11:30	2010/11/11	29	
-	-	-	3	3	447	450	9:30-8:30	2010/11/14	30	



(2)

(3)

**QCC Problem Specification**

**Quality Characteristics**

Variable Data  
 Attribute Data

**Problem Title:** منتوج المنظف المائل

**Number of Qlty. Characteristics:** 4      **Size of Subgroups:** 450

**Number of Subgroups:** 30

Note: The above is the initial setup.  
You can modify it later.

**OK**      **Cancel**      **Help**

(4)

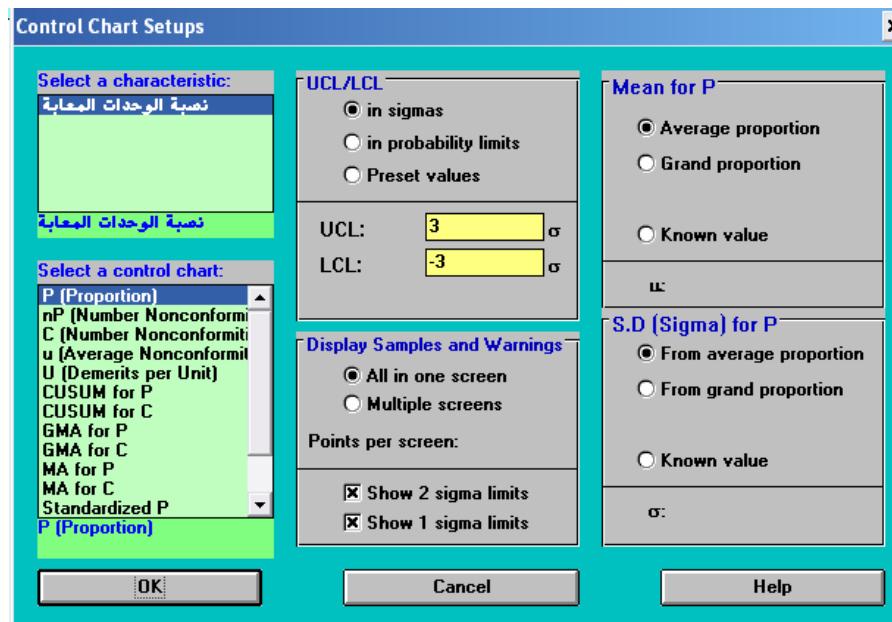


Subgroup	Date	Time	Size	الوزن	النضوج	التشقق	المظهر	Disabled	Cause	Action	Comment
1	3/10/2010	8.30:9.30	450	8	0	0	0	0			
2	4/10/2010	8.30:9.30	450	4	1	0	0	0			
3	5/10/2010	8.30:9.30	450	2	0	0	0	0			
4	6/10/2010	8.30:9.30	450	2	1	0	0	0			
5	7/10/2010	1.30:11.30	450	0	0	0	0	0			
6	8/10/2010	.30:12.30	450	0	0	0	0	0			
7	1/10/2010	8.30:9.30	450	1	1	0	0	0			
8	2/10/2010	8.30:9.30	450	2	1	0	0	0			
9	3/10/2010	8.30:9.30	450	2	0	0	0	0			
10	4/10/2010	8.30:9.30	450	2	1	0	0	0			
11	7/10/2010	8.30:9.30	450	0	1	0	0	0			
12	8/10/2010	1.30:10.30	450	0	0	0	0	0			
13	9/10/2010	1.30:11.30	450	0	0	0	0	0			
14	10/10/2010	.30:12.30	450	0	0	0	0	0			
15	11/10/2010	8.30:9.30	450	2	0	0	0	0			
16	12/10/2010	8.30:9.30	450	4	0	0	0	0			
17	13/10/2010	8.30:9.30	450	1	1	0	0	0			
18	14/10/2010	8.30:9.30	450	0	0	0	0	0			
19	15/10/2010	8.30:9.30	450	1	0	0	0	0			
20	16/10/2010	8.30:9.30	450	2	1	0	0	0			
21	17/10/2010	8.30:9.30	450	4	1	0	0	0			
22	18/10/2010	8.30:9.30	450	3	1	0	0	0			
23	19/10/2010	2.30:1.30	450	0	0	0	0	0			
24	20/10/2010	8.30:9.30	450	4	0	0	0	0			
25	21/10/2010	8.30:9.30	450	2	1	0	0	0			
26	22/10/2010	8.30:9.30	450	4	0	0	0	0			
27	23/10/2010	8.30:9.30	450	4	0	0	0	0			
28	24/10/2010	8.30:9.30	450	3	1	0	0	0			
29	25/10/2010	.30:12.30	450	0	0	0	0	0			
30	26/10/2010	8.30:9.30	450	3	0	0	0	0			

(5)

Subgroup	Date	Time	Size	نسبة الوحدات	Disabled	Cause	Action	Comment
1	3/10/2010	00:16:22	450	0.0178				
2	4/10/2010	8.30:9.30	450	0.0111				
3	5/10/2010	8.30:9.30	450	0.0044				
4	6/10/2010	8.30:9.30	450	0.0067				
5	7/10/2010	1.30:11.30	450	0				
6	8/10/2010	.30:12.30	450	0				
7	9/10/2010	8.30:9.30	450	0.0044				
8	10/10/2010	8.30:9.30	450	0.0067				
9	11/10/2010	8.30:9.30	450	0.0044				
10	12/10/2010	8.30:9.30	450	0.0067				
11	13/10/2010	8.30:9.30	450	0.0022				
12	14/10/2010	1.30:10.30	450	0				
13	15/10/2010	1.30:11.30	450	0				
14	16/10/2010	.30:12.30	450	0				
15	17/10/2010	8.30:9.30	450	0.0044				
16	18/10/2010	8.30:9.30	450	0.0088				
17	19/10/2010	8.30:9.30	450	0.0044				
18	20/10/2010	8.30:9.30	450	0				
19	21/10/2010	8.30:9.30	450	0.0022				
20	22/10/2010	8.30:9.30	450	0.0067				
21	23/10/2010	8.30:9.30	450	0.0111				
22	24/10/2010	8.30:9.30	450	0.0088				
23	25/10/2010	2.30:1.30	450	0				
24	26/10/2010	8.30:9.30	450	0.0088				
25	27/10/2010	8.30:9.30	450	0.0067				
26	28/10/2010	8.30:9.30	450	0.0088				
27	29/10/2010	8.30:9.30	450	0.0088				
28	30/10/2010	8.30:9.30	450	0.0088				
29	31/10/2010	.30:12.30	450	0				
30	1/11/2010	8.30:9.30	450	0.0067				

(6)



P – chart : (7)



P – chart : (8)



Subgroup	Date	Time	Size	نسبة الوحدات	Disabled	Cause	Action	Comment
1	4/10/2010	8.30:9.30	450	0.0111				
2	5/10/2010	8.30:9.30	450	0.0044				
3	6/10/2010	8.30:9.30	450	0.0067				
4	7/10/2010	8.30:11.30	450	0				
5	8/10/2010	8.30:12.30	450	0				
6	9/10/2010	8.30:9.30	450	0.0044				
7	10/10/2010	8.30:9.30	450	0.0067				
8	11/10/2010	8.30:9.30	450	0.0044				
9	12/10/2010	8.30:9.30	450	0.0067				
10	13/10/2010	8.30:9.30	450	0.0022				
11	14/10/2010	8.30:10.30	450	0				
12	15/10/2010	8.30:11.30	450	0				
13	16/10/2010	8.30:12.30	450	0				
14	17/10/2010	8.30:9.30	450	0.0044				
15	18/10/2010	8.30:9.30	450	0.0088				
16	19/10/2010	8.30:9.30	450	0.0044				
17	20/10/2010	8.30:9.30	450	0				
18	21/10/2010	8.30:9.30	450	0.0022				
19	22/10/2010	8.30:9.30	450	0.0067				
20	23/10/2010	8.30:9.30	450	0.0111				
21	24/10/2010	8.30:9.30	450	0.0088				
22	25/10/2010	8.30:11.30	450	0				
23	26/10/2010	8.30:9.30	450	0.0088				
24	27/10/2010	8.30:9.30	450	0.0067				
25	28/10/2010	8.30:9.30	450	0.0088				
26	29/10/2010	8.30:9.30	450	0.0088				
27	30/10/2010	8.30:9.30	450	0.0088				
28	31/10/2010	8.30:12.30	450	0				
29	1/11/2010	8.30:9.30	450	0.0067				

(1) : (9)



: (10)



# Experimental and numerical evaluation of friction stir welding of AA 2024-W aluminum alloy

Dr.Ayad M. Takhakh  
ayadmurad@nahrainuniv.edu.iq

Hamzah N. Shakir  
almohands4ever@gmail.com

## Abstract

Friction Stir Welding (FSW) is one of the most effective solid states joining process and has numerous potential applications in many industries. A FSW numerical tool, based on ANSYS F.E software, has been developed. The amount of the heat gone to the tool dictates the life of the tool and the capability of the tool to produce a good processed zone. Hence, understanding the heat transfer aspect of the friction stir welding is extremely important for improving the process. Many research works were carried out to simulate the friction stir welding using various softwares to determine the temperature distribution for a given set of welding conditions. The objective of this research is to develop a finite element simulation of friction stir welding of AA2024-W Aluminium alloy. Numerical simulations are developed for thermal conductivity, specific heat and density to know the relationship of these factors with peak temperature. Variation of temperature with input parameters is observed. The simulation model is tested with experimental results. The results of the simulation are in good agreement with that of experimental results.

## الحلول العملية والرقمية للحام الاحتاكي بالمزج (FSW) لسبائك المنيوم

### AA2024-W

م. حمزة نور الدين شاكر

أ.م.د. أياد مراد طخاخ

جامعة النهرين / كلية الهندسة

## الخلاصة

يعد اللحام الاحتاكي بالمزج (FSW) واحد من الطرق الفعالة للحام الحالة الصلبة ويدخل في الكثير من التطبيقات في مختلف الصناعات . تم تطوير حلول رقمية للحام الاحتاكي بالمزج بالاعتماد على برنامج ANSYS لحساب كمية الحرارة المتولدة خلال عملية اللحام والتي تؤثر على عمر وجودة منطقة اللحام والعدة، اذ ان من المهم معرفة كيفية انتقال الحرارة خلال اللحام الاحتاكي بالمزج. عدد من الباحثين درسو توزيع درجات الحرارة خلال هذا النوع من اللحام باستخدام برامجيات متعددة. الغرض من هذا البحث تطوير حلول رقمية باستخدام طريقة العناصر المحددة (FEM) بالاستناد على برنامج ANSYS لسبائك المنيوم نوع AA2024-W . تم تطوير هذه الحلول بالاعتماد على العلاقة التي تربط خواص التوصيل الحراري و الحرارة النوعية و الكثافة مع درجات الحرارة حيث تتغير هذه الخواص بتغير درجات الحرارة. المحاكاة التي تم الحصول عليها تم التحقق عملياً من نتائجها واظهرت نتائج المقارنة وجود توافق حيد .

**Keywords:** Friction stir welding, AA 2024-W, Temperature distribution, Simulation.

## Introduction

A method of solid phase welding, which permits a wide range of parts and geometries to be welded and called friction stir welding (FSW), was invented by W. Thomas and his colleagues of The Welding Institute (TWI), UK, in 1991. Friction stir welding can be used for joining many types of material and metal combinations, if tool material and designs can be found which operate at the forging temperature of the workpieces. The process has been used for manufacture of butt welds, overlap welds, T-sections and corner welds. For each of these joint geometries specific tool designs are required which are being further developed and optimized [1,2]. Friction stir welding is a relatively simple process as shown in Fig. 1.

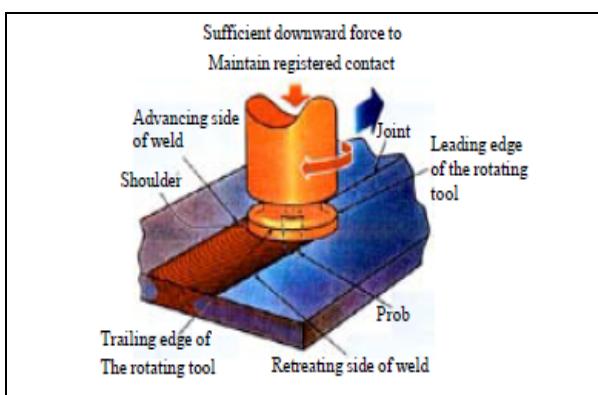


**Fig.1: Schematic diagram of FSW process [1].**

This process has been widely used in many industries such as space, aircraft, marine, transport and food processing. Low distortion, high quality, lower residual stresses, fewer weld defects and

low cost joints are the main advantages of this method [3]. Friction stir welding (FSW) is a solid-state joining process in which a rotating tool,

consisting of a shoulder and a (generally threaded) pin, moves along the butting surfaces of two rigidly clamped plates placed on a backing plate. The shoulder is in sustained contact with the top surface of the workpiece. Part of the heat is generated by the friction between the shoulder and the workpiece, and another part is generated by material stirring. This heat softens the material to be welded. Severe plastic deformation and flow of this plasticised metal occurs as the tool is translated along the welding direction. A FSW joint consists of various zones involving different microstructures and mechanical properties. The heat affected zone (HAZ) is the most distant from the joint centerline. It is not deformed during the process, but the microstructure evolves due to the welding thermal cycles, influencing the mechanical properties. The thermomechanically affected zone (TMAZ) and the weld nugget are highly deformed by the material rotational flow [4]. Due to the interesting features of FSW, lots of research activities have been carried out on different materials (aluminum alloys first of all, but also steel, titanium, magnesium, copper, polymers etc.) and on different weld geometries [5].

Consequently, numerical simulation could be a helpful device for predicting process behavior and its optimization .In friction stir welding, heat is generated first on the basis of friction between tool and work piece and then by shape change. A



portion of the generated heat disseminated through work piece, will affect distortion, residual stress distribution as well as weld quality of the during welding process, but also can save research time and cost [7]. Some studies of FSW on temperature field and residual stresses have been carried out through FEM software i. e. ANSYS® [8-9], ABAQUS [10-13], Forge® [14], DEFORM-3D™[15]. Finite element Methods also used to study the effect of FSW process parameters on mechanical properties of various welded alloys based on solid mechanics [16] or develop the mathematical model. [17].

Thus, much research has been done to study the simulation of temperature distribution during friction stir welding process. This was recognized in present study based on ANSYS software, the results obtained for simulation was comparison with that actual experiment.

piece [6]. Finite element analysis is an effective method in the investigation of welding, because it not only can obtain the instantaneous results

### **Experimental work**

Friction stir welds were made on the plate samples of 2024-Waluminum alloy on -W treatment which used to describe an as quench condition between solution heat treatment and artificial or room temperature aging.

The test plates of size 200 mm X 100 mm X 3.5 mm are prepared from aluminum alloy AA2024 plates Fig.2. The chemical composition and mechanical properties of the base material are presented in Table 1 and Table 2, respectively. The experiment is conducted using FSW machine developed by TAKSAN milling machine, as shown in Fig.3. The welding was done by single pass.

**Table 1: Chemical composition of Al 2024-W alloy.**

Element	Zn	Cu	Fe	Ni	Mn	Ti	Si	Mg	Cr	Al
Weight %measured	0.06	3.87	0.3	0.02	0.38	0.005	0.16	1.39	0.006	93.83
Standard [24]	-	4.4	-	-	-	-	0.18	1.5	-	-

**Table 2: Typical mechanical properties of wrought aluminum 2024-W alloy.**

	Ultimate strength(MPa)	Yield strength(MPa)	Percentage of elongation	Hardness HV
Measured	365	-	22%	105
Standard [25]	335		28%	110

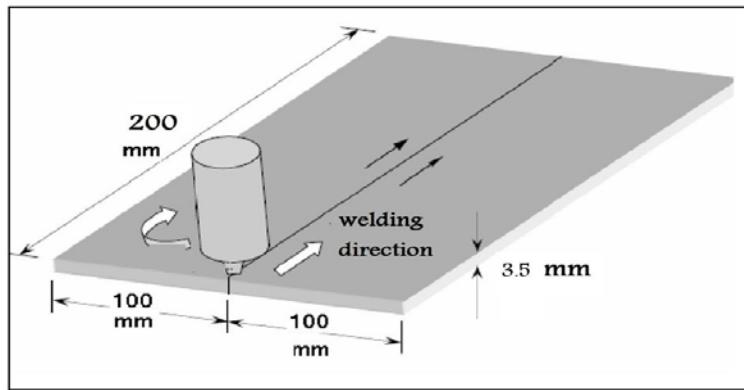


**Fig 2**  
**:Dimensio**  
**ns of weld**  
**ed plate**

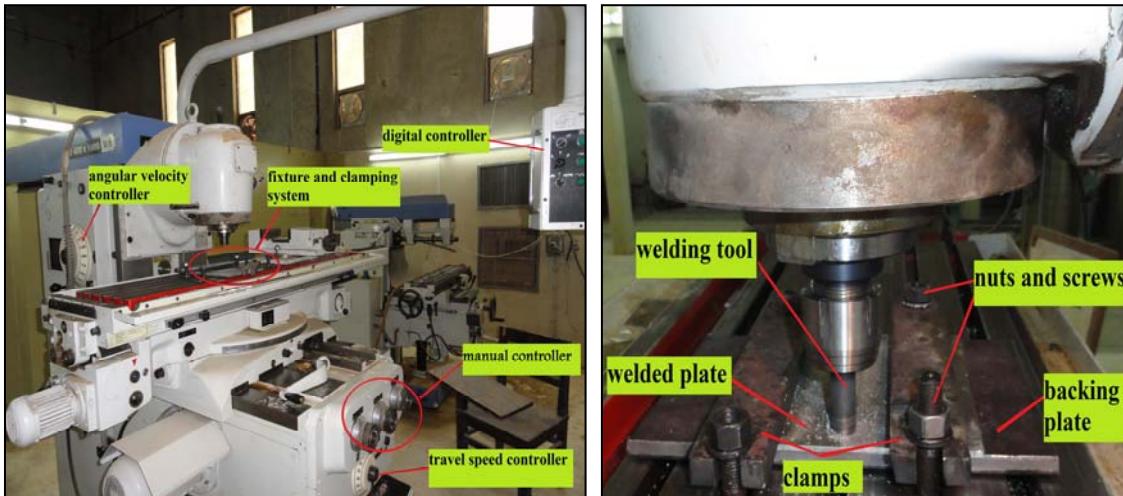


**Fig. 3: Taksan milling machine**

The FSW tools are manufactured using Turning machine. The configuration of the designed FSW Tool is:

- Tool pin profile of cylindrical without draft.
- Tools having ratio of shoulder diameter to pin diameter( $D/d$ ) is 3 has been chosen for this study because it is having good joining

properties among various pin configurations [17].The manufactured tool is shown in Fig. 4.

The research work was planned to be carried out in the following steps:

1. Identifying the important process parameter



2. Finding the upper and lower limits of the process parameter Viz. tool rotational speed and welding speed to select the best result of welding efficiency for simulation.
3. Checking the adequacy of the numerical simulation.
4. Conducting the conformity test runs and comparing the results.

FSW parameters used in this study were listed in Table 3. The rotating tool used in this study was made of X38 tool steel.

FSW parameters used in this study were listed in Table 3. The rotating tool used in this study was made of X38 tool steel.



**Fig. 4: FSW Tool (X38 tool steel)**

To determine the tensile strength of the stir zone, tensile test specimens were sectioned as per ASTM E8 in the transverse direction perpendicular to the weld line with CNC milling machine as shown in Fig.5. Transverse tensile tests were performed on PHYWE machine to evaluate the mechanical properties of the joints.

**Table 3: FSW work parameters**

Sample No.	Welding speed(mm/min)	Rotation speed(rpm)
F1	20	900
F2	30	900
F3	40	900
F4	20	710
F5	30	710
F6	40	710



**Fig. 5: Tensile specimens before test.  
Thermal Modeling of FSW**

FEM is most commonly used in numerical analysis for obtaining approximate solutions to wide variety of engineering problems. In the present study, a commercial general purpose finite element program ANSYS® 11.0 was used for numerical simulation of friction stir welding process. The ANSYS® program has many finite element analysis capabilities, ranging from simple, linear, static analysis to a complex nonlinear, transient dynamic analysis. The thermal and mechanical responses of the material during friction stir welding process are investigated by finite element simulations.

In this study, a thermal model is developed for analysis. First, brick element is SOLID70, Homogenous; a linear, transient three-dimensional heat transfer model is developed to determine the temperature fields, rate independent. The finite element models are parametrically built using APDL (ANSYS Parametric Design Language) provided by ANSYS® [18]. The model are then validate by comparing the results with established material data

### **Mathematical thermal model.**

Simple analytical solution to the heat flow problem can be found. Instead, a numerical solution is sought, based on a descretization of Fourier's 2nd Law:

$$\rho c \frac{\partial T}{\partial t} = \lambda \left( \frac{\partial^2 T}{\partial x^2} + \frac{\partial^2 T}{\partial y^2} + \frac{\partial^2 T}{\partial z^2} \right) + \frac{q_0}{V} \quad (1)$$

Where  $\rho c$  is the volume heat capacity,  $\lambda$  is thermal conductivity,  $x$ ,  $y$ , and  $z$  are the flow simulations space coordinates; and  $q_0 / V$  is the source term [19].

### **Assumptions.**

The following assumptions are made in developing the model;

- The heat generation is due to friction and Heat generated during penetration and extraction is also considered.
- The coefficient of friction is considered changed and dropped with increasing temperature.
- Material properties are uniform.
- Heat transfer from the workpiece to the clamp is negligible [18].

The important process characteristics which are required to be considered for the purpose of modeling are as follows:

- a) Moving heat source;
- b) Weld speed.
- c) Axial load to calculate heat generation.
- d) Material properties.

### **Elements Used**

In the present thermal analysis, the workpiece is meshed using a brick element called SOLID70. This element has a three-dimension thermal conduction capability and can be used for a three-dimensional, steady-state or transient thermal analysis. The element is defined by eight nodes with temperature as single degree of freedom at each node and by the orthotropic material properties. Heat fluxes or convectons can be input as surface loads at the element faces as shown on the two faces in Figure 8. An advantage of using this element is that, the element can be replaced by an equivalent structural element for the structural analysis.

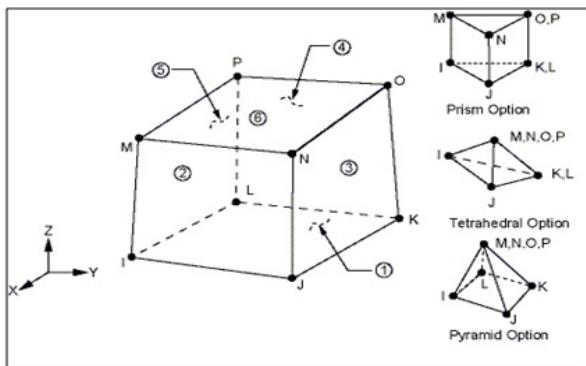


**Fig. 6: three dimensional thermal solid elements SOLID70 [18]**

As SOLID70 cannot apply heat flux and convection at the same time, a three-dimensional thermal-surface-effect element was used. For applying convection on the workpiece surface, SURF152 was used overlaying it onto faces of the base elements made by SOLID70. The convective were applied as a surface load by choosing KEYOPT. Figure 6 shows the geometry, node locations, and the coordinate system of the element, which is defined by four to nine nodes and the material properties [18].

### Mesh Development

Three dimensional SOLID70 elements were used to mesh the sheets. The workpiece was divided into small parts along the length and along the width as shown in figure below.

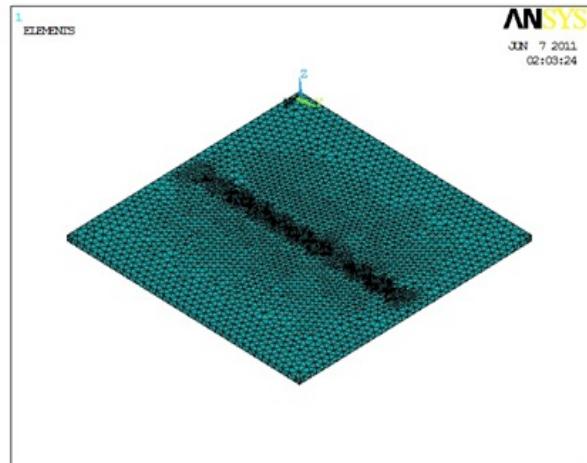


**Fig. 7: 3D mesh of modeled welded plates for aluminum alloy in ANSYS program**

### Material Properties

Thermal properties of the material such as thermal conductivity, specific heat, and density are temperature dependent. An accurate estimation of temperatures is critical in FSW process because the stresses and strains developed in the weld are temperature dependent. Therefore, temperature dependent thermal properties of 2024 Aluminum alloy are used in finite element model. The thermal material properties of 2024 Aluminum alloy are tabulated in Table 4. The thermal property values are obtained from ref. [20], and for higher temperatures the values are linearly extrapolated.

**Table 4 Thermal material properties of 2024 Aluminum alloy.[20]**

T°C	Density kg m⁻³	C <sub>p</sub> JK⁻¹ g⁻¹	H <sub>T</sub> -H <sub>25</sub> Jg⁻¹	λ Wm⁻¹ K⁻¹
25	2785	0.85	0	175
100	2770	0.90	66	185
200	2750	[0.95]⁰	159	193
300	2730	0.97	255	193
400	2707	1.00	353	190
500	2683	1.08	457	188
538⁰	2674	1.10	566	188
632	2500	1.14⁰	970	85.5
700	2480	1.14⁰	1048	85
800	2452	1.14⁰	1162	84

## Boundary Condition

Boundary condition for FSW thermal model were specified as surface loads through ANSYS® codes. Assumptions were made for various boundary conditions based on data collected from various published research papers.

Convective and radiative heat losses to the ambient occurs across all free surfaces of the workpiece and conduction losses occur from the workpiece bottom surface to the backing plate. To consider convection and radiation on all workpiece surfaces except for the bottom, the

heatloss  $q_s$  is calculated by equation (2). [18]

$$q_s = \beta(T - T_0) + \epsilon\sigma(T^4 - T_0^4) \quad (2)$$

where  $T$  is absolute temperature of the

workpiece,  $T_0$  is the ambient temperature,  $\beta$  is the

convection coefficient,  $\epsilon$  is the emissivity of the

plate surfaces, and  $\sigma = 5.67 \times 10^{-12} \text{ w/m}^2 \cdot ^\circ\text{C}$  is the Stefan-Boltzmann constant. In the current

model, a typical value of  $\beta$  was taken to be 10

$\text{w/m}^2 \cdot ^\circ\text{C}$  using an ambient temperature of  $25^\circ\text{C}$ .

In order to account for the conductive heat loss through the bottom surface of weld plates, a high overall heat transfer coefficient has been assumed. This assumption is based on the previous studies. The heat loss was modeled approximately by using heat flux loss by convection  $q_b$  given by equation (3). [18].

$$q_b = \beta_b(T - T_0) \quad (3)$$

where  $\beta_b$  is a fictitious convection coefficient.Due

to the complexity involved in estimating the contact condition between the sheet and the



backing plate, the value of  $\beta_b$  had to be estimated

by assuming different values through reverse analysis approach. In this study, the optimized

[18 w/m<sup>2</sup>.°C] value of  $\beta_b$  was found to be 100

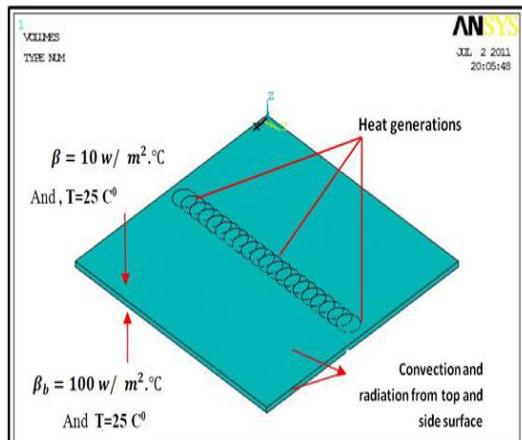


**Fig. 8: Schematic representation of boundary condition for thermal analysis.**

### Heat Generation input during FSW.

For the ideal case considered, the torque required to rotate a circular shaft relative to the plate surface under the action of an axial load is given by [19]:

$$q_o = \int_0^{M_R} dM = \int_0^R \mu P(r) 2\pi r^2 dr = \frac{2}{3} \mu \pi P R^3 \quad (4)$$

Where  $M$  is the interfacial torque,  $\mu$  is the friction coefficient,  $R$  is the surface radius, and  $P(r)$  is the pressure distribution across the interface (here assumed constant and equal to  $P$ ). If all the shearing work at the interface is converted into frictional heat, the average heat input per unit area and time becomes

$$q_o = \int_0^{M_R} \omega dM = \int_0^R \omega 2\pi \mu P r^2 dr \quad (5)$$

where  $q_o$  is the net power (in Watts) and  $\omega$  is the angular velocity (in rad/s). The next step is to express the angular velocity in terms of the rotational speed  $N$  (in rot/s). By substituting  $\omega = 2\pi N$  into Eq. (5), we get

$$q_o = \int_0^R 4\pi^2 \mu P N r^2 dr = \frac{4}{3} \pi^2 \mu P N R^3 \quad (6)$$

From Eq. (6), it is obvious that the heat input depends both on the applied rotational speed and the shoulder radius, leading to a nonuniform heat generation during welding. These parameters are the main process variables in FSW [19].

From equation (6) we can get the heat generation by divide the net power  $q_o$  on the volume of shoulder[19]:

$$Q_{sh} = \frac{q_o}{V_{sh}} \quad \text{watt/m}^3 \quad (7)$$

Where  $V_{sh} = A_{sh} * t$ , where  $V_{sh}$  is the shoulder volume,  $A_{sh}$  is the area of shoulder,  $t$  is the thickness.

$$A_{sh} = \pi * R_{sh}^2$$

Where the coefficient of friction of aluminum is 0.4 [19 , 21], this value is changed and dropped gradually in friction stir welding because the coefficient of friction  $\mu$  varies with temperature and reached to 0.3 [22].where The temperature measurement in FSW for the workpiece was reported that the maximum temperature developed during FSW process ranges from 80% to 90% from melting temperature of the welding material [20].

### Simulation

The thermal modeling was carried out. Transient thermal analysis is the stage. Figure 9 illustrates the flow diagram of the method used for the finite element analysis.

In order to simplify the moving tool on the sheet welded line in ANSYS program , all next steps (as shown in flow chart) was made to make it like moving tool along welded line in the ANSYS program.

To get a good accurate of results, more steps of shoulder area must make in the simulation of program as shown in figure 10

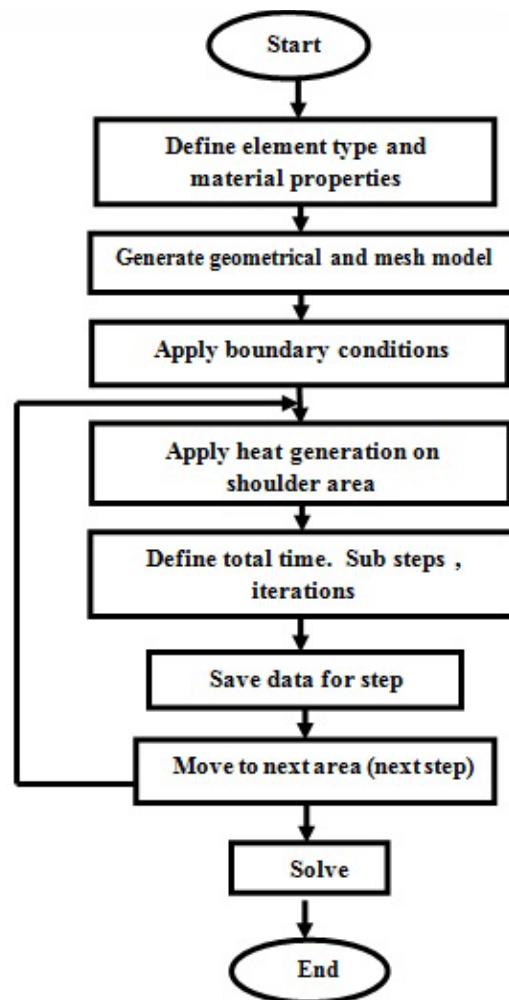


**Fig. 9: Flowchart of thermal modeling.**

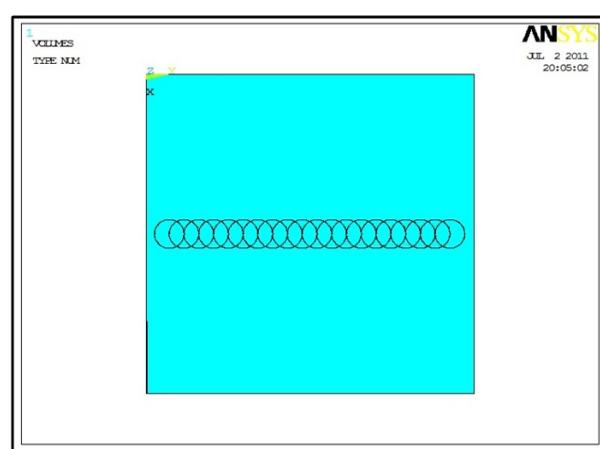


**Figure 10: steps of circular shoulder area along welded line.**

here each shoulder circle has heat generation and time step, also each circle represents one step.

Heat input (heat generation) is estimated by trial and error from ANSYS program because applied pressure  $P$  from equation 4 is unknown.

The method of heat input calculation by trial and error found by take the data (temperature and time) of thermocouple readings for one point (for example A in fig. 11) where in these data we depend on maximum temperature and make the following steps:

- 1- Assumed high value of heat generation where this value entered in program to make simulation for aluminum plate to get the maximum temperature at point A.
- 2- Assume low value of heat generation and examined it in program by make simulation for the aluminum plate at point A to get maximum temperature for these low value of heat generation.
- 3- Applying the interpolation on these (three values of temperature and two values of heat generation ) to get a good agreement heat for this work .

After get good agreement heat generation, applying it in other steps of program.

From the validation shows that the present work can be used for modeling thermal distribution.

Four K-type thermocouples at selected points of aluminum sheet as shown in figure 11 have been used for measuring the temperature distribution by using temperature recorder type BTM-4208SD which contains 12 channels as shown in figure 11 (a &b) when these four thermocouples have been embedded in selected positions to 1.5 mm on the aluminum sheet as shown in figure (12 left) where recorded data temperatures changed with time are saved as excel file in the RAM of temperature recorder as shown in figure (12. right).



**Fig. 11.a , Temperature recorder**

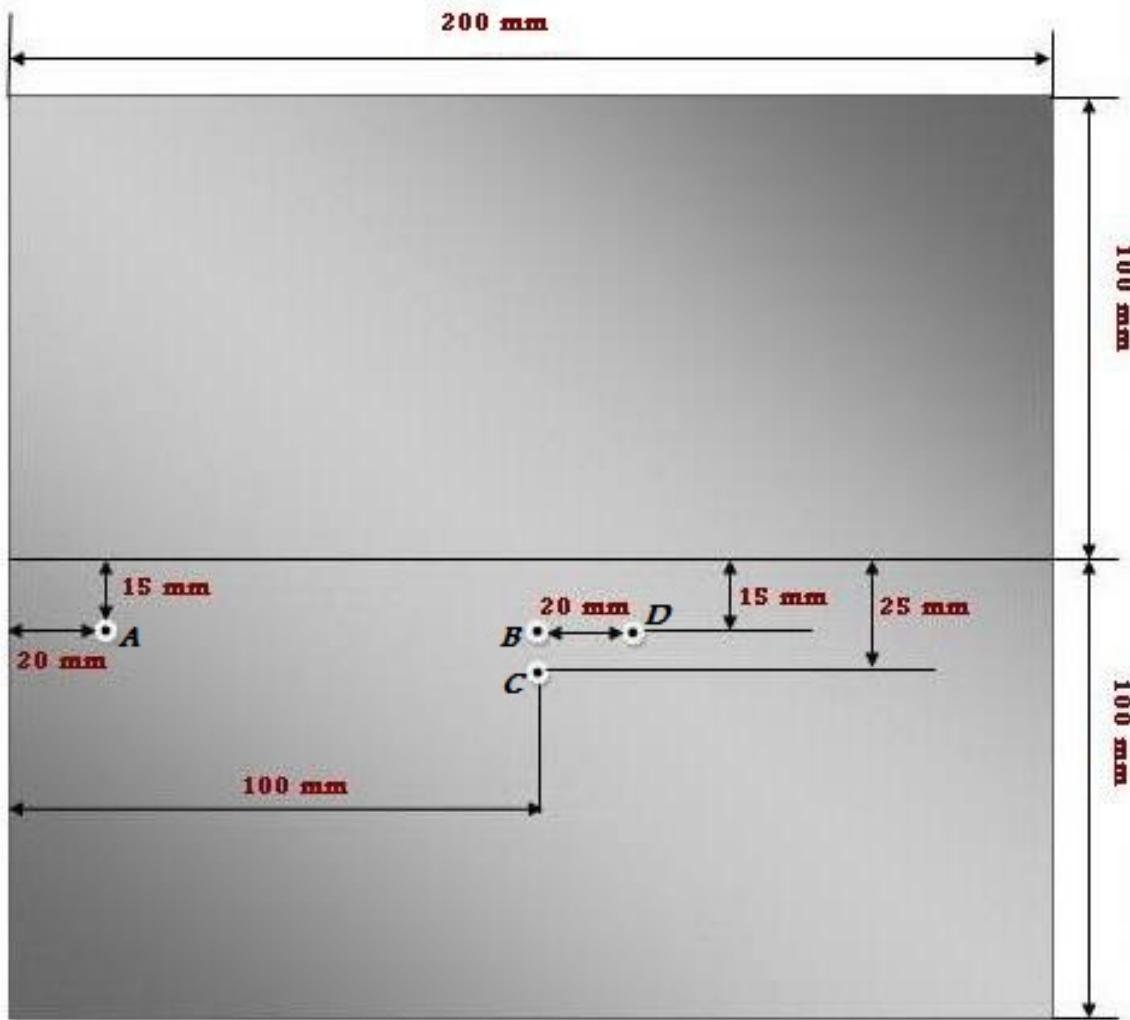
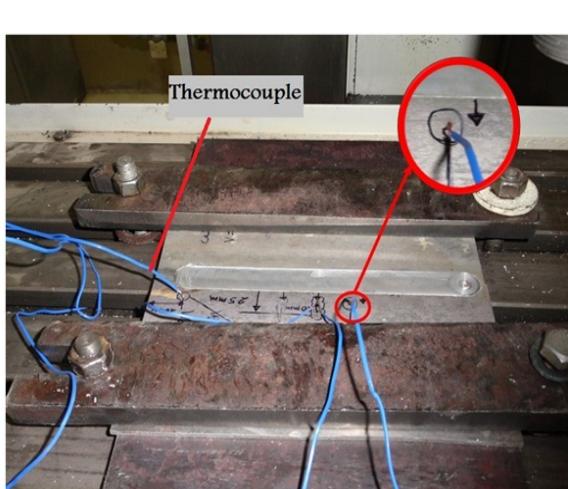


Fig. 11.b :Thermocouples location embedded on aluminum workpiece.



	A	B	C	D	E	F	G	H	I	J	K	L
	T4KTemp C											
550	1036 #####	23:07:39	72.1 T4KTemp i	71.5 T4KTemp i	83.7 T4KTemp i	73.6 T4KTemp C						
551	1037 #####	23:07:40	72.1 T4KTemp i	71.5 T4KTemp i	83.7 T4KTemp i	73.6 T4KTemp C						
552	1038 #####	23:07:41	72.1 T4KTemp i	69.8 T4KTemp i	83.7 T4KTemp i	72.6 T4KTemp C						
553	1039 #####	23:07:42	72.1 T4KTemp i	69.8 T4KTemp i	82.4 T4KTemp i	72.6 T4KTemp C						
554	1040 #####	23:07:43	71.1 T4KTemp i	69.8 T4KTemp i	82.4 T4KTemp i	71.4 T4KTemp C						
555	1041 #####	23:07:44	71.1 T4KTemp i	69 T4KTemp i	81.7 T4KTemp i	71.4 T4KTemp C						
556	1042 #####	23:07:45	71.1 T4KTemp i	69 T4KTemp i	81.7 T4KTemp i	70.8 T4KTemp C						
557	1043 #####	23:07:46	71.1 T4KTemp i	69 T4KTemp i	81 T4KTemp i	70.8 T4KTemp C						
558	1044 #####	23:07:47	71.1 T4KTemp i	69 T4KTemp i	81 T4KTemp i	70.8 T4KTemp C						
559	1045 #####	23:07:48	71.1 T4KTemp i	69 T4KTemp i	81 T4KTemp i	70.8 T4KTemp C						
560	1046 #####	23:07:49	71.1 T4KTemp i	69 T4KTemp i	81 T4KTemp i	70.8 T4KTemp C						
561	1047 #####	23:07:50	71.1 T4KTemp i	69 T4KTemp i	81 T4KTemp i	70.8 T4KTemp C						
562	1048 #####	23:07:51	71.1 T4KTemp i	70.1 T4KTemp i	80.3 T4KTemp i	70.8 T4KTemp C						
563	1049 #####	23:07:52	71 T4KTemp i	70.1 T4KTemp i	80.3 T4KTemp i	72.1 T4KTemp C						
564	1050 #####	23:07:53	71 T4KTemp i	70.1 T4KTemp i	80.3 T4KTemp i	72.1 T4KTemp C						
565	1051 #####	23:07:54	70.8 T4KTemp i	69.4 T4KTemp i	80.3 T4KTemp i	72.1 T4KTemp C						
566	1052 #####	23:07:55	70.8 T4KTemp i	69.4 T4KTemp i	80.3 T4KTemp i	72.1 T4KTemp C						
567	1053 #####	23:07:56	70.8 T4KTemp i	69.4 T4KTemp i	79.1 T4KTemp i	72.4 T4KTemp C						
568	1054 #####	23:07:57	70.8 T4KTemp i	69.4 T4KTemp i	79.1 T4KTemp i	70.0 T4KTemp C						
569	1055 #####	23:07:58	70.6 T4KTemp i	69.4 T4KTemp i	79.1 T4KTemp i	70.0 T4KTemp C						
570	1056 #####	23:07:59	70.3 T4KTemp i	69.4 T4KTemp i	79.1 T4KTemp i	70.3 T4KTemp C						
571	1057 #####	23:08:00	70.3 T4KTemp i	69.4 T4KTemp i	78.3 T4KTemp i	70.3 T4KTemp C						
572	1058 #####	23:08:01	70.3 T4KTemp i	69.4 T4KTemp i	78.3 T4KTemp i	70.3 T4KTemp C						
573	1059 #####	23:08:02	70 T4KTemp i	69.4 T4KTemp i	78.3 T4KTemp i	70.8 T4KTemp C						
574	1060 #####	23:08:03	70 T4KTemp i	69.4 T4KTemp i	78.3 T4KTemp i	70.8 T4KTemp C						
575	1061 #####	23:08:04	69.7 T4KTemp i	69.4 T4KTemp i	78.3 T4KTemp i	70.1 T4KTemp C						
576	1062 #####	23:08:05	69.7 T4KTemp i	69.3 T4KTemp i	77.2 T4KTemp i	70.1 T4KTemp C						

Fig. 12: Thermocouples embedded in the aluminum plate (left), Temperatures data as Excel file (right).



## Results and discussions

The employed model may be utilized to predict temperature distribution during FSW operations under working conditions. Figures (17 to 24) shows the temperature distributions in the workpiece welded with rotational speed 710 rpm and welding velocity 40mm/min ,which has the best tensile properties of the weldments are given in Table 3. The weld strength is about 86% of that of AA 2024 base metal strength in W condition. All the tensile testing specimens were fractured in the stir zones of the welds.

:

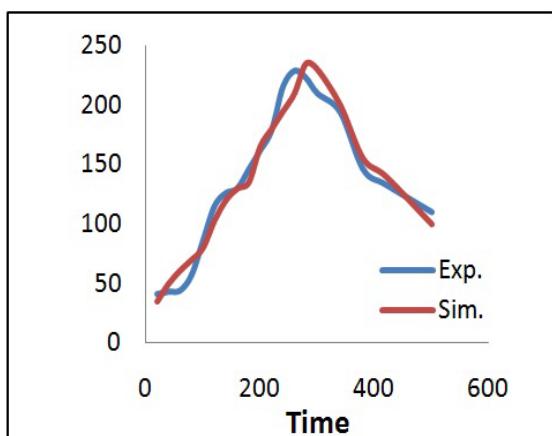


Fig. 13 : Temperature distribution in point  
 $\omega = 710 \text{ RPM}$ ,  $v = 40 \text{ mm/minA}$ .

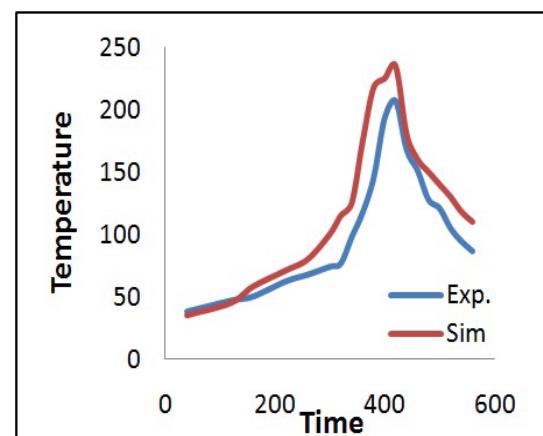
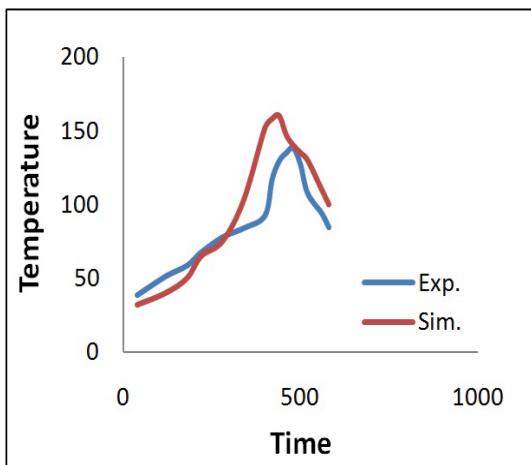


Fig. 14 : Temperature distribution in point  
 $\omega = 710 \text{ RPM}$ ,  $v = 40 \text{ mm/minB}$ .

Experimental results friction stir welding of material 2024 Al alloy were compared with simulation results of ANSYS program. The welded workpiece had dimensions  $200 \times 200 \times 3.5$  mm, the tool had a shoulder radius of 9 mm, pin radius of 3 mm and pin length of 3.3 mm. the rotation speed and translational speed that utilized in this comparison were 710 RPM and 40 mm/min respectively.

Figures below 13 to 16 show the results that calculated experimentally and simulation



**Fig. 15:** Temperature distribution in point  
 $\omega = 710 \text{ RPM}$ ,  $v = 40 \text{ mm/min}$ C.

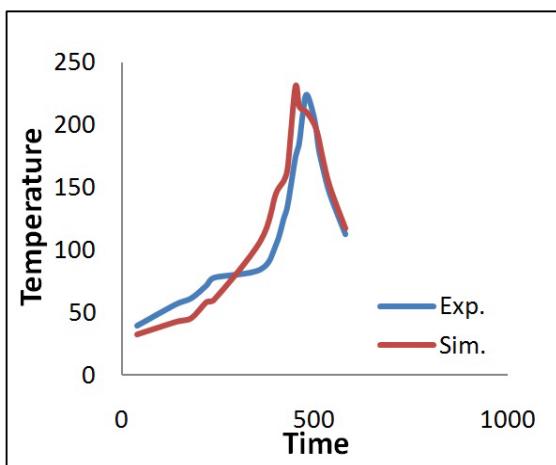


**Fig. 16 :** Temperature distribution in point  
 $\omega = 710 \text{ RPM}$ ,  $v = 40 \text{ mm/min}$ D.

The modeling of this work is solved and the temperature distribution obtained for the model and the result show that there is good agreement between present work and ANSYS result. The difference in results of temperature distribution

between experimental examination and modeling ranged between 5 – 14% which its acceptance.

Figures 17 to 24 show the maximum temperature of welding plate which has been reached at several time steps:

:

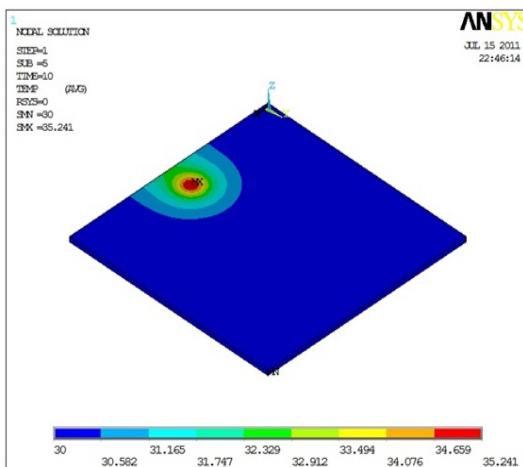


**Fig. 17:** Temperature distribution at 10 s, Max. Temp.  $35 \text{ C}^0$

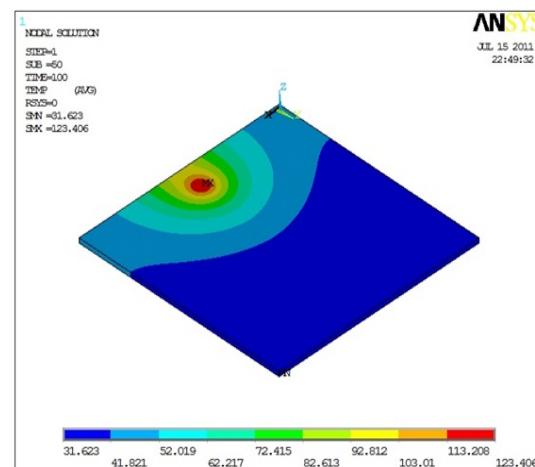


**Fig. 18 :**Temperature distribution at 100 s, Max. Temp.  $123 \text{ C}^0$

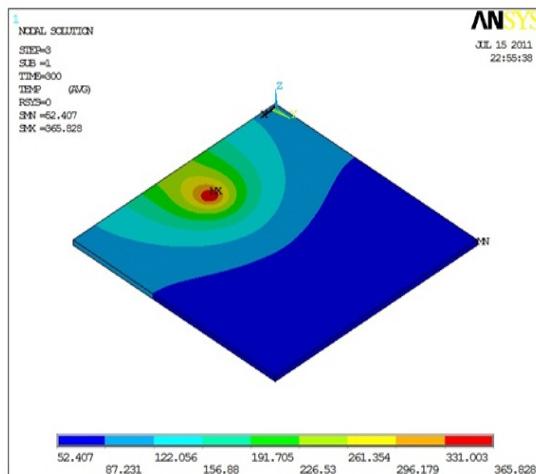


Fig. 19 :Temperature distribution at 300 s,  
Max. Temp. 365 C°

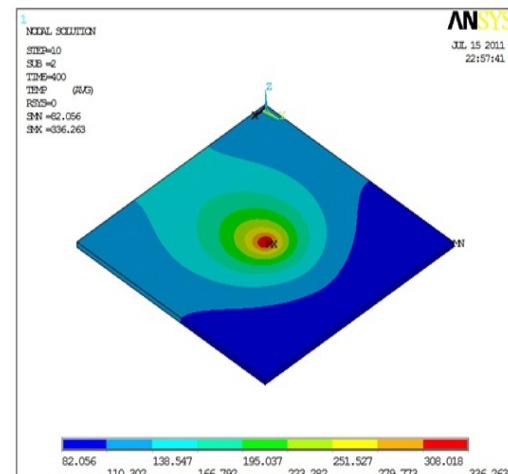


Fig. 20 :Temperature distribution at  
400 s, Max. Temp. 336 C°

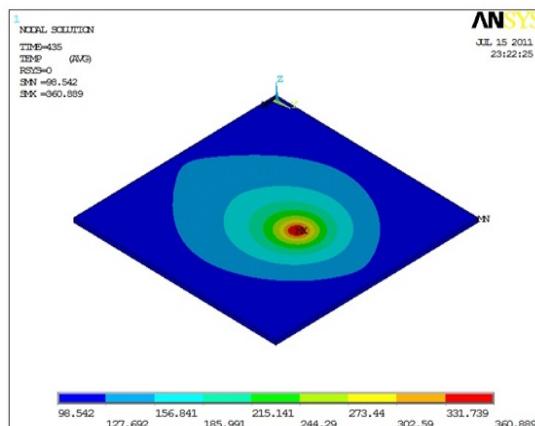


Fig. 21:Temperature distribution at  
435 s, Max. Temp. 360 C°

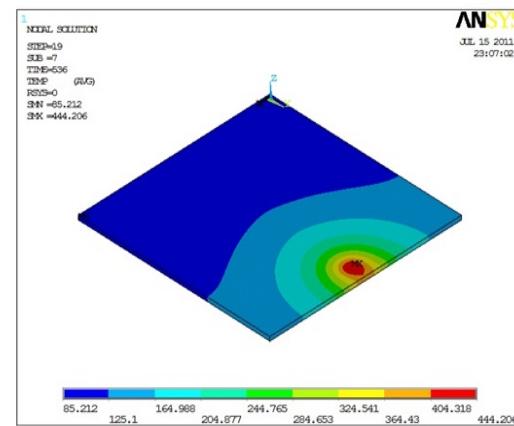


Fig. 22:Temperature distribution at  
536 s, Max. Temp. 444 C°

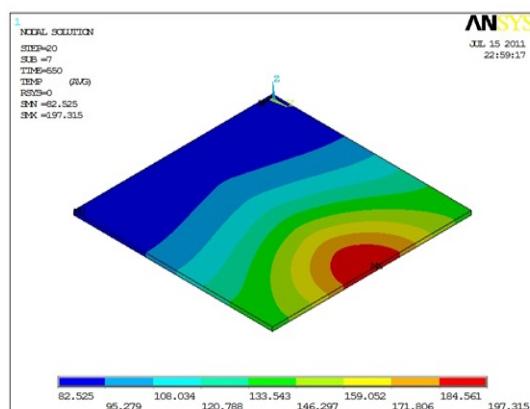


Fig. 23 : Temperature distribution at  
550 s, Max. Temp. 197 C°

731

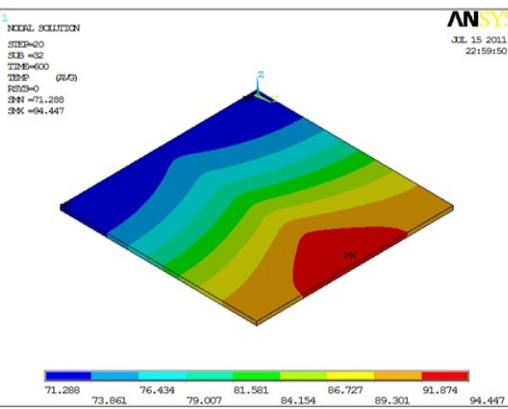


Fig. 24 : Temperature distribution at  
600 s, Max. Temp. 94 C°

As it is seen, temperature gradient increases in front of the tool comparing to its backside, i.e., the temperature profile extends further towards the welded region behind the moving tool.

Because of shoulder rotation, the material flow near the top surface is accelerated, and therefore, material deformation on the top surface next to the contact region is higher than the region at the bottom side. The material deformation has an important role on the formation of the weld zone profile in FSW operations [23].

The predicted maximum temperature is 444 C° in the region under the shoulder on the top surface. This temperature is about 58 C° below the solidus temperature of Al 2024 and is within accepted temperature range in FSW process.

Figures 13 to 16 shows the thermal cycles in the various points of sample No.6 at the depth of 1.5 mm. It can be seen that heating rate is higher than the corresponding cooling rate to room temperature.

As expected, the peak temperatures are higher at locations close to the weld line, and it decreases toward the HAZ.

### Conclusion

- 1- Variation of the nugget-zone temperature with respect to time.
- 2- The temperature decreases with distance perpendicular direction of the tool on the top surface.

3- The variation of peak temperature with respect to thermal conductivity, specific heat and density is obtained.

4- Comparison of temperature profile developed between simulation values and the experimental results showed the possibility of more accurate determination using present simulation.

### REFERENCES

1. **M. Awang, et. al.** "Experience on Friction Stir Welding and Friction Stir Spot Welding at Universiti teknologi petronas", journal of applied science 11(2011):pp.1959-1965.
2. **M. Vural, et. al.** "On the Friction Stir Welding of Aluminium alloys EN AW 2024-0 and EN AW 5754-H22", Archives of Materials Science and Engineering, Volume 28, Issue 1,(2007),pp.49-54.
3. **S. Rajakumar, et. al.** "Statistical Analysis to Predict Grain Size and Hardness of the Weld Nugget of Friction-Stir-Welded AA6061-T6 aluminium alloy joints", Int J Adv Manuf Technol (2011) 57:151–165, DOI 10.1007/s00170-011-3279-5.
4. **Kevin Deplus, et. al.** "Residual Stresses in Aluminium Alloy Friction Stir Weld", Int J Adv Manuf Technol (2011) 56: pp.493–504.



- 5. Ciro Bitondo, et. al.** "Friction-Stir Welding of AA 2198 butt joints: Mechanical Characterization of The Process and of The Welds Through DOE Analysis", Int J Adv Manuf Technol (2011) 53:pp.505–516.
- 6. Mohammad Riahi & Hamidreza Nazari** "Analysis of Transient Temperature and Residual Thermal Stresses in Friction Stir Welding of Aluminum Alloy 6061-T6 via Numerical Simulation", Int J Adv Manuf Technol (2011) 55:pp.143–152.
- 7. Dong-yang Yan, et. al.** "Predicting Residual Distortion of Aluminum Alloy Stiffened Sheet After Friction Stir Welding by Numerical Simulation", Materials and Design 32 (2011)pp. 2284–2291.
- 8. P. Prasanna, et. al.** "Experimental and Numerical Evaluation of Friction Stirs Welding of AA 6061 –T6 Aluminum alloy", ARPN Journal of Engineering and Applied Sciences, VOL. 5, NO. 6,(2010).
- 9. P. Prasanna, et. al.** "Finite Element Modeling for Maximum Temperature in Friction Stir Welding And Its Validation", Int J Adv Manuf Technol (2010) 51:pp.925–933.
- 10. S. Mandal, et. al.** "The Effect of The Alclad Layer on Material Flow and Defect Formation During Friction-stir Welding", Metallurgical and Materials Transactions, Volume 42, Issue 6,(2011),pp.1717-1726.
- 11. H. Jamshidi Aval, et. al.** "Experimental and Theoretical Valuations of Thermal Histories and Residual Stresses in Dissimilar Friction Stir Welding of AA5086-AA6061", Int J Adv Manuf Technol, (2011), DOI 10.1007/s00170-011-3713-8.
- 12. H. Jamshidi Aval, et. al.** "Evolution of Microstructures and Mechanical Properties in Similar and Dissimilar Friction Stir Welding of AA5086 and AA6061", Materials Science and Engineering, Volume 528, Issue 28, pp.8071- 8083 (2011).
- 13. Z. Zhang, et. al.** "Coupled Thermo-Mechanical Model Based Comparison of Friction Stir Welding Processes of AA2024-T3 in Different Thicknesses", J Mater Sci (2011) 46: pp5815–5821, DOI 10.1007/s10853-011-5537-1.
- 14. Mohamed Assidi and Lionel Fourment** "Accurate 3d friction stir Welding Simulation Tool Based on Friction Model Calibration", Int J Mater Form Vol. 2 (2009) 1:327–330.
- 15. G. Buffa, et. al.** "A new Friction Stir Welding Based Technique for Corner Fillet Joints: Experimental and Numerical Study", Int J Mater Form Vol. 3 (2010) 1:pp.1039 – 1042.

- 16.** **Z. Zhang & H. W. Zhang** "Material Behaviors and Mechanical Features in Friction Stir Welding Process", Int J Adv Manuf Technol (2007) 35:pp.86–100.
- 17.** **R. Palanivel, et. al.** "Development of Mathematical Model to Predict the Mechanical Properties of Friction Stir Welded AA6351 Aluminum Alloy", Journal of Engineering Science and Technology Review 4 (1) (2011)pp. 25–31.
- 18.** **Manthan Malde** " Thermomechanical Modeling and Optimization of Friction Stir Welding" , B.E., Osmania University, Hyderabad, India,( 2009).
- 19.** **Ø. FRIGAARD, et. Al.** "A Process Model for Friction Stir Welding of Age Hardening Aluminum Alloys", Metallurgical and Materials Transactions a volume 32a, (2001), 1189-1200.
- 20.** **Kenneth C Mills** "Recommended Values of Thermophysical Properties for Selected Commercial Alloys ", The Materials Information Society **ASM**, (2005).
- 21.** **Vijay Soundararajan, et. al.** " Thermo-Mechanical Model With Adaptive Boundary Conditions for Friction Stir Welding of Al 6061", International Journal of Machine Tools & Manufacture 45 (2005) pp.1577–1587.
- 22.** **R. Nandan, et. al.**"Three-dimensional Heat and Material Flow During Friction Stir Welding of Mild Steel ", Acta Materialia 55 (2007)pp. 883–895.
- 23.** **H. Jamshidi Aval, et. al.** "Theoretical and Experimental Investigation into Friction Stir Welding of AA 5086", Int J Adv Manuf Technol (2011) 52: pp.531–544.
- 24.** **Myer Kutz** "Mechanical Engineering Handbook", Third edition, Material and Mechanical design, (2006).
- 25.** **Hakan Aydin , et. al.**"Tensile Properties of Friction Stir Welded Joints of 2024 Alluminume Alloy in Different Heat Treated State", J Master design, doi:10.1016/j.matdes. (2008).08.034



## Effects Of Functionalized Polyethylene And Styrene Butadiene Styrene Polymers On Performance Grade Of Local Asphalt Binder

Dr. Alaa H. Abed

University of AL-Nahrain, Baghdad-Iraq

alaah29@yahoo.com, 07902185188

### Abstract

Rutting is one of the major distresses in pavement. The objective of this paper is to develop an improved asphalt binder grading system for Iraq based on the principle of Superpave system, and increasing performance grade of product asphalt binder in Iraq using polymers without raising the viscosity of the binder. Two types of polymers are used, Plastomers, Functionalized Polyethylene (PE) which is developed by asphalt research group in Wisconsin University in the USA, and Elastomers, Styrene Butadiene Styrene (SBS) with and without cross linker. Mastercurve are drawn for these modified binders, Rolling thin film aged, to show effects on rheological properties at high temperature for complex modulus ( $G^*$ ) and phase angle ( $\delta$ ). It concluded that 3.5% of Functionalized Polyethylene polymer (PE) is more effective than 4% of Styrene Butadiene Styrene (SBS) to shift up performance grade of local asphalt binder two grades to be PG (76-16). Furthermore, the viscosity of binders increasing about 200% when using 4 % SBS, while no significant effect on viscosity when using 3.5 % of PE, therefore, there is no need to increase temperature of mixing and compaction which may be effect on polymers In addition  $G^*/\sin\delta$  is increased by a ratio of 1.6 to 2.96 for 2%, 4% respectively of SBS-based modifier (RTFO aged) and 1.4 to 3 for 2%, 3.5% respectively of PE-based polymers modifier. It can be seen that PE reduce  $G^*\sin\delta$  about 10%, while SBS increase  $G^*\sin\delta$  about 30% and PE reduces the stiffness of asphalt binder about 15 % at low temperature which make PE more effective, there is no significant effects on m-value.

**KEYWORDS:** Superpave; Performance Grading; Modified Binder; Master curve, PE, SBS.

(PE)			
(SBS)			
PE	%3.5	. (δ)	( $G^*$ )
SBS		.PG(16-76)	
		PE	SBS %4
2.96	1.6	$G^*/\sin\delta$ .	(%200)
3	1.4		
PE	%10	$G^*\sin\delta$ .	SBS %4 %2
	PE	%15	PE %3.5 %2
	M		.SBS %30
			PE



## Introduction

Polymer-modified asphalt binders are frequently and effectively used in the paving industry to improve pavement performance and to increase pavement life. Polymer modification is reported to reduce pavement cracking due to thermal stresses and repetitive loads and, especially, decrease rutting due to plastic deformation.

Application of modified asphalt concrete is more expensive than traditional asphalt pavement. Therefore, it is important that the polymer-modified pavement is manufactured and constructed properly to assure that the improvement in pavement performance and pavement life is achieved.

The use of polymer modified asphalt cements in pavement construction is an important step in increasing the life and durability of asphalt roads. Polymer-modified asphalt is typically manufactured by adding Plastomers, "Functionalized Polyethylene (PE) polymer", Elastomers "Styrene Butadiene Styrene (SBS) with or without cross linker"

Modification of asphalt binders is usually performed to improve one or more of the basic asphalt properties that are related to one or more of the pavement distress modes, the basic properties that have been targeted include Rigidity, Elasticity, Brittleness, Storage stability and durability, resistance to accumulated damage (Bahia et al 1995).

## Objective

The objective of this paper is to analyze and select polymer-modified binders that may improve pavement performance without presenting extensive difficulties in mixing, when compared to traditional asphalt binders by considering influence of polymer types and concentration on the high temperature performance of polymer modified asphalt.

## Rheological Properties Of Local Asphalt Binder

Table 1 shows result of rheological properties measured for the Daurah asphalt binder. The testing included the rotational viscometer (RV), dynamic shear rheometer (DSR) and bending beam rheometer (BBR) for binders after different aging conditions, following the Superpave performance grading requirements, which are tested in Wisconsin University.

## Polymers

Polymer means multiple "mer" units, which can be linked together to form the polymers. Link is formed by breaking the double carbon/carbon bond and allowing it to link with others to form. The physical structure of the polymers chain has a large effect on the mechanical properties of plastics. The number of monomers in each chain defines the degree of polymerization. The source of synthetic polymers many are produced from processing crude oil. They are commonly referred to as plastics. Properties depend on the polymer chain lengths, extent of cross-linking, radial compounds, and the production process.

Daurah asphalt is used as base binder and two types of polymers are used in this study, Elastomers "Styrene Butadiene Styrene (SBS) with or without cross linker" and Plastomers, new type of polymer developed by highway research group in Wisconsin University called "Functionalized Polyethylene (PE)".

### **Polymers Concentration**

Initially, 2% polymer concentrations are selected for each polymer, and 0.123 % of cross linker is mixed with 2% of SBS polymer. Based upon results, further polymer concentrations are determined, 4% of SBS and 3.5% of PE, for raising performance grade of Daurah asphalt binder two grades.

### **Preparation Of Polymer-Asphalt Mixes**

To obtain SBS combination the initial mixing rate is about 250 rpm. Typically, the binder climbed the shaft of the mixer, and a spatula is used to prevent it from climbing into the mixer motor. The mixing rate is kept low enough to prevent the binder from climbing past the spatula. As the temperature of the binder raise, the mixing rate could be increased gradually. The mixing rate is increased every 10 minutes until the maximum rate of 1,000 rpm is reached for 4 to 4.5 hours and maintained the temperature of the sample at 180°C, which is necessary to obtain a uniform mixture, therefore, need to put heavy gas to prevent oxidation of binder. The polymers are added into the asphalt gradually for 0.5 hour. The temperature of the mixture is dropped immediately when the polymer are added, therefore, need to raise the temperature to 180°C. Mixing is completed when the modified asphalt no longer climbed the mixer shaft. a small spatula is dipped in the mix and smeared on clean, white paper. If the polymer grains are visible, the mixing process is incomplete. When the grains disappeared, the process is considered complete.

For obtaining modifying asphalt binder with Functionalized Polyethylene (PE) polymer is easier than asphalt modifying with SBS because the temperature of mixing is 145°C for 1.5 hour, therefore, there is no problem with oxidation.

### **Modification Of Asphalt Binder**

The rheological properties listed in Table (1) of Daurah asphalt binder does not meet climate, traffic, and pavement structure requirements in Iraqi, therefore, it is very necessary to shift up the performance grade of local asphalt binder by adding modifier as one of the attractive approach to improve the asphalt binder properties that are related to one or more of the pavement distress modes. The basic properties that have been targeted include rigidity (total resistance to deformation which can be measured by complex modulus like  $G^*$  under dynamic loading or by creep stiffness,  $S(t)$ ,under quasi-static loading), Elasticity (recovery of deformation using stored energy applied, it can be measured either by phase angle( $\delta$ ) or by logarithmic creep rate ( $m$ )), brittleness (failure at low strains is the best definition of brittleness), storage stability and durability (oxidative aging, physical hardening and volatilization are key durability properties, resistance to accumulated damage (rutting and fatigue damage) (Bahia, 2009). The superpave binder specification contains criteria based on simply assumption test to match critical pavement performance, Anderson et al. 1994; Bahia et al. 1999 reported the most important assumption for neat and modification binders and concluded that stability of modified asphalt. It is noticed that effect of different polymers on failure properties is depend largely on the type of interaction between the asphalt and polymer, the molecular nature of the polymer additive, and the way of dispersion in the asphalt.



## Result And Analysis

The superpave performance grading (PG) system is developed to evaluate binder properties at specific temperature with specific testing system. One of the main objectives of Strategic Highway Research Program (SHRP) was to develop test methods for characterization of asphalts that are equally applicable to unmodified or modified asphalt cements, collectively called asphalt binders (Anderson et al. 1994). A modifier can be selected to improve one or more of the main performance related properties of asphalts. Table 1 shows SHRP parameters obtained from superpave tests under various temperature for different types of modified binders at different concentration, it can be seen although PE modifier shifting up performance grade with same jump of SBS modifier but not significant effects on viscosity, therefore, there is no need to increase temperature of mixing and compaction which may be effect on polymers, Furthermore, 3.5 % of PE is used for shifting up the performance two grade while 4% of SBS is needed to achieve PG(76-16). Figure 1 depicts a bar chart of the ratios of the SHRP parameters for asphalt after modification with different concentration of the based polymer. The Figure indicates that there is a favorable trend in changes of all the performance parameter,  $G^*/\sin\delta$  is increased by a ratios of 1.6 to 2.96 for SBS-based modifier (RTFO aged) and 1.4 to 3 for PE-based polymers modifier. It can be seen that PE would be reduced  $G^*\sin\delta$  about 10%, while increase 30% if SBS is added. PE reduces the stiffness of asphalt binder about 15 percent at low temperature which makes PE more effective, while there is no significant effects on m-value could be seen.

## Master Curve Fof Modified Binders

Rheological properties can be represented either by the variation of  $G^*$  and  $\delta$  as a function of frequency at a constant temperature (commonly referred to as master curve) or by the variation of  $G^*$  and  $\delta$  with temperature at a selected frequency or loading time, commonly called isochronal curve (Bahia, 2009). To show the effect of modifiers type on  $G^*$  and  $\delta$ , master curves are drawn in Figure 2 using dynamic shear rheometer for rolling thin film oven aged binder at 64°C. It can be seen that  $G^*$  increases while  $\delta$  decreases. This indicates that an increase in rigidity and elasticity, which results better resistance to permanent deformation.

## Conclusions

Two types of polymers are used in this study Plastomers “Functionalized Polyethylene (PE) polymer”, Elastomers “Styrene Butadiene Styrene (SBS) with or without cross linker”.

Table 1 shows SHRP parameters “performance grade” for Daurah asphalt binder which not much the requirements of climate and traffic for Iraq, therefore, it is very necessary to add polymer to the local asphalt binder.

It is noticed that 3.5% of Functionalized Polyethylene (PE) polymer is more effective than 4% of Styrene Butadiene Styrene (SBS) to shift up performance grade of local asphalt binder two grades PG (76-16). The viscosity of binders increasing about 200% when using 4 % SBS while no significant effect on viscosity when using 3.5% of PE, therefore, there is no need to increase temperature of mixing and compaction which may be effect on polymers.  $G^*/\sin\delta$  is increased by a ratios of 1.6 to 2.96 for 2%, 4% respectively of SBS-based

modifier RTFO aged and 1.4 to 3 for 2%, 3.5% respectively of PE-based polymers modifier. It can be seen that PE reduce  $G^* \cdot \sin \delta$  about 10%, while SBS increase  $G^* \cdot \sin \delta$  about 30% and PE reduces the stiffness of asphalt binder about 15 % at low temperature which make PE more effective. Furthermore, there is no significant effect on m-value. Master curve shows that using 2% of SBS,  $G^*$  is increased by 12% than  $G^*$  of asphalt binder modified with 2% of PE at 19.35 Hz frequency, and there is no significant change in  $\delta$ .

### References

- Anderson, D., D. Christensen, H. Bahia, R. Dongre, Sharma M., and J. Button,(1994) "Binder characterization and evaluation", Volume 3:"Physical characterization," Report No. SHRP-A- 369, the Strategic Highway Research Program, national Research Council, Washington, D.C.
- Bahia, H.U., and D.A. Anderson, (1995), "The New Proposed Rheological Properties of Asphalt Binders: Why are They Required and How Do They Compare to The Conventional Properties," Physical Properties of Asphalt Binders, ASTM, STP 1241, pp. 1-27
- Bahia H., Zhai H., Kose S., and Bonnetti K., "Non-linear Viscoelastic and Fatigue Properties Of Asphalt Binder", Journal of Association of Asphalt Paving Technologists, Vol.68, 1999, pp. 1-34.
- Bahia, H.U., (2009), "Modeling of Asphalt Binder Rheology and Its Application to Modified Binders", Chapter 2, Modeling of Asphalt Concrete, by the American Society of Civil Engineering, pp.,11-56

Bahia, H.U, D. Hanson, M. Zeng, H. Zhai, and A. Khatri, NCHRP Report 459, "Characterization of Modified Asphalt Binders in Superpave Mix Design," National Academy Press, Washington, D.C., 2001.

**Table (1) Rheological Properties of Daurah Asphalt Binder**

Type of Asphalt	Daurah 40-50 Pen.	
Aging	Original	
Rotational Viscosity Pa.sec	@135 °C	0.516
$G^*/\sin \delta$ , kPa	@64 °C @70 °C	2.37 0.958
True Grade	69.83 °C	1
Penetration	@25°C	45
Softening Point	48 °C	
Aging	RTFO	
$G^*/\sin \delta$ , kPa	@64 °C @70 °C	4.05 1.887
True Grade	69.13 °C	2.2
Loss (%)	0.73	< 1
Penetration	@25°C	29
Softening Point	52 °C	
Aging	PAV	
$\delta$	@25 °C @28 °C	53° 59°
m-value	@25 °C @28 °C	0.525 0.578
$G^*\cdot \sin \delta$ , kPa	@25 °C @28 °C	7320 4700
Creep Stiffness, MPa	@-16 °C @-22 °C	182 426
True Grade	-18.9 °C	300
Slop m-value	@-16 °C @-22 °C	0.399 0.289
True Grade	-21.4 °C	0.3
Penetration	@25°C	20
Softening Point	57°C	



Table 2 Effect of Modification Binder on SHRP Parameters

Type of Asphalt	Daurah 64-16	Daurah 70-16	Daurah 76-16	Daurah 70-16	Daurah 70-16	Daurah 76-16
Aging	Original	Original	Original	Original	Original	Original
R.V@13 5 °C Pa.sec	0.516	0.84	1.56	1.04	0.547	0.563
G*/sin δ, kPa	@64 °C 2.37	@70 °C 1.4	@76 °C 1.15	@70 °C 1.88	@70 °C 1.983	@76 °C 2.2
	@70 °C 0.958	@76 °C 0.696	@82 °C 0.621	@76 °C 0.991	@76 °C 1.054	@82 °C 1.725
Aging	RTFO	RTFO	RTFO	RTFO	RTFO	RTFO
G*/sin δ, kPa	@64 °C 4.05	@70 °C 3.03	@76°C 2.35	@70 °C 2.79	@70 °C 2.646	@76 °C 2.391
	@70 °C 1.887	@76 °C 1.47	@82 °C 1.23	@76 °C 1.51	@76 °C 1.329	@82°C 1.329
Loss (%)	< 1	< 1	< 1	< 1	< 1	< 1
Aging	PAV	PAV	PAV	PAV	PAV	PAV
δ	@25 °C 53°	@25 °C 52°	@28 °C 52°	@25 °C 54°	@25 °C 55°	@25 °C 52°
	@28 °C 59°	@28 °C 56°	@31 °C 55°	@28 °C 62°	@28 °C 59°	@28 °C 56°
G*.sin δ, kPa	@25 °C 7320	@25 °C 7540	@28°C 6060	@25 °C 7445	@25 °C 7363	@25 °C 6993
	@28 °C 4700	@28 °C 4760	@31 °C 4140	@28 °C 2790	@28 °C 4560	@28 °C 4444
Creep Stiffness	@-16 °C 182	@-16 °C 206	@-16 °C 215	@-16 °C 225	@-16 °C 181	@-16 °C 158
, MPa	@-22 °C 426	@-22 °C 454	@-22 °C 471	@-22 °C 480	@-22 °C 419	@-22 °C 380
Slop m-value	@-16 °C 0.399	@-16 °C 0.363	@-16 °C 0.329	@-16 °C 0.372	@-16 °C 0.396	@-16 °C 0.372
	@-22 °C 0.289	@-22 °C 0.269	@-22 °C 0.278	@-22 °C 0.281	@-22 °C 0.289	@-22 °C 0.266

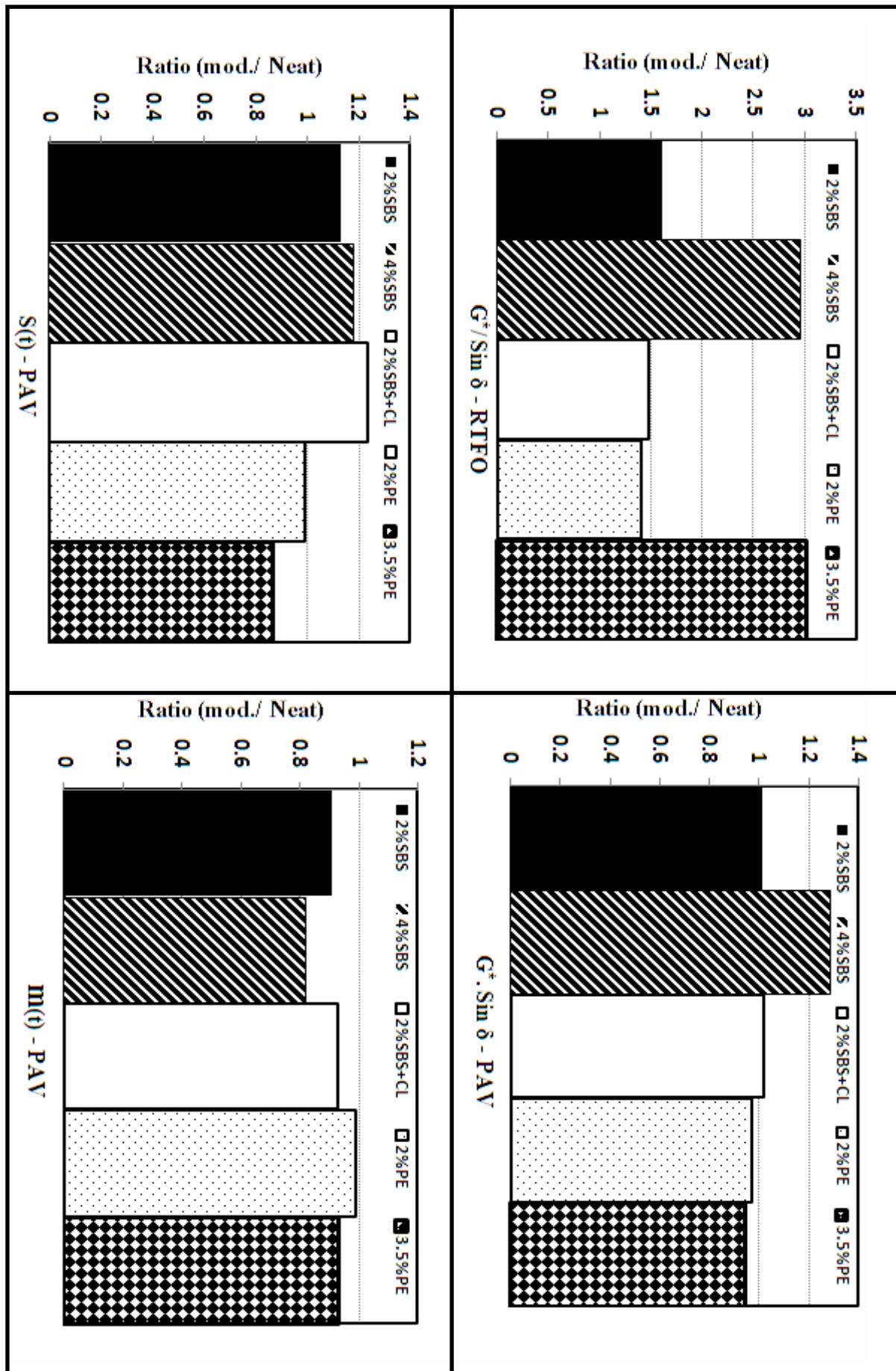


Fig. 1 Change in Performance Grade Parameter

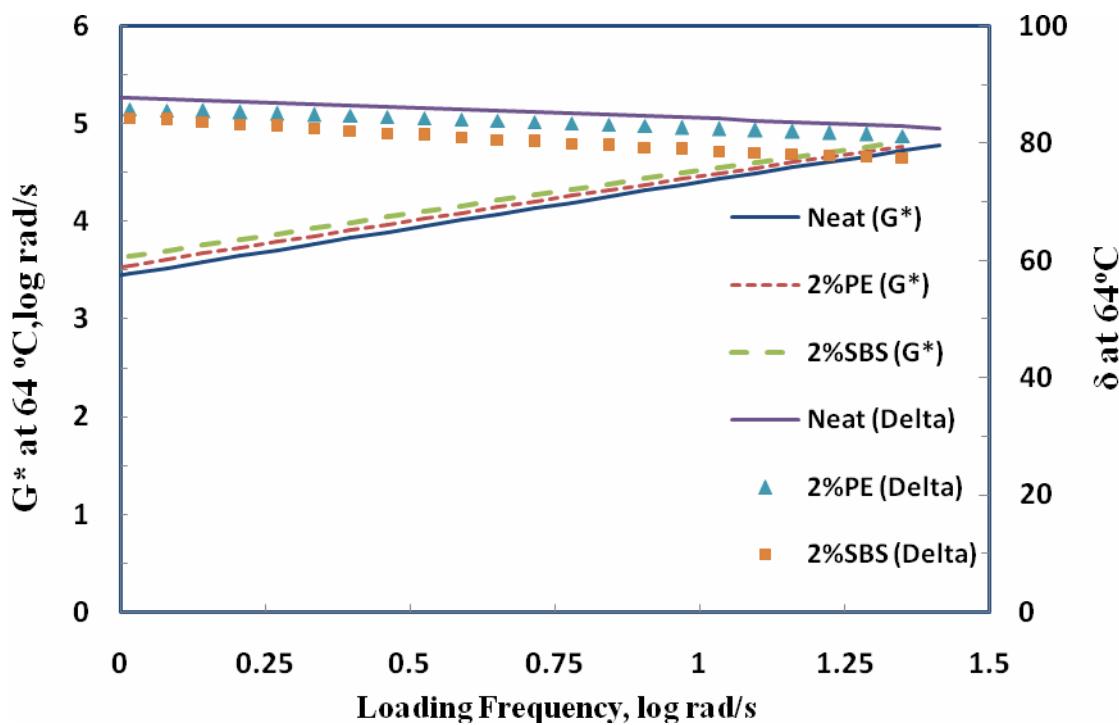


Fig. 2 Master Curve of Neat and Modified Asphalt at 64°C.



## New Correlation To Calculate Absolute Permeability From Gas Permeameter

Ass. Lecture Dhorgham S. Ibrahim

Ass. Lecture Hussein H. Hussein

University of Baghdad  
College of Engineering  
Petroleum Engineering Department

### Abstract

In this study, two correlations are developed to calculate absolute rocks permeability from core samples tested by Gas Permeameter Apparatus. The first correlation can be applied if  $K_g \leq 100$ , the second correlation can be applied if  $K_g > 100$ . Sixty core samples having different permeabilities to give a wide range of values that necessary to achieve a correlation.

The developed correlation is easily applied and a quick method to avoid repeating the test at different pressure values. Only one pressure test is required to reach absolute permeability which is equivalent liquid permeability.

The final results show, after comparison between the values of permeability from the correlations and the value of absolute permeability by liquid permeameter, good agreement between the values.

### علاقة جديدة لحساب النفاذية المطلقة باستعمال جهاز نفاذية الغاز

المدرس المساعد ضر غام سكبان إبراهيم

المدرس المساعد ضر غام سكبان إبراهيم

جامعة بغداد- كلية الهندسة

قسم هندسة النفط

### الخلاصة:

تم في هذه الدراسة تطوير علائقى ترابط لحساب النفاذية المطلقة للصخور من العينات التي يتم فحصها بجهاز قياس النفاذية باستخدام الغاز. العلاقة الأولى يمكن تطبيقها إذا كانت النفاذية للغاز  $\geq 100$  ، العلاقة الثانية يمكن تطبيقها إذا كانت النفاذية للغاز  $< 100$  . تم إعداد 60 عينة صخرية مختلفة النفاذيات لتغطية مدى واسع من القيم اللازمة لعمل العلاقتين . إن العلاقتين المطورة سهلة التطبيق وتعتبر طريقة سريعة تجنبنا لتجرار الفحص لمختلف الضغوط والاكتفاء بالفحص عند ضغط واحد ونتمكن من خلالها إلى التوصل لقيمة النفاذية المطلقة المكافئة لنفاذية السائل.

وقد أظهرت النتائج النهائية بعد اجراء المقارنة بين النفاذية المستخرجة من العلاقتين مع قيم النفاذية المطلقة المستخرجة من جهاز قياس النفاذية باستخدام السائل وجود تطابق كبير بين القيم.

## Introduction

Laboratory measurement of permeability usually uses air as the flowing fluid and thus the value obtained is permeability to air (Kair).

Cole, frank (1969) said dry gas is usually used (air, N<sub>2</sub>, He) in permeability determination because of its convenience, availability, and to minimize fluid-rock reaction.

The low pressure air permeability of core often differs from its permeability to liquid by 30 to 100 percent due to the Klinkenberg effect. These errors are avoided if the permeability to gas was measured at two or three pressures and plotted against the reciprocal of the mean pressure, and then extrapolating to infinite pressure to obtain the equivalent liquid permeability. This method is generally reliable, but has two drawbacks-it requires tedious measurements, and requires longer time to reach steady state. New correlation is developed to calculate equivalent liquid permeability from a single run on core sample by Ruska Gas Permeameter.

## THEORY OF OPERATION

The measurement of the permeability should be restricted to the low (laminar/viscous) flow rate region, where the pressure remains proportional to flow rate within the experimental error. For high flow rates, Darcy's equation as expressed by equation (1) is inappropriate to describe the relationship of flow rate and pressure drop. [Ali Hussein 1988]

$$q = \frac{KA(p_1 - p_2)}{\mu L} \quad (1)$$

In using dry gas in measuring the permeability, the gas volumetric flow rate q varies with pressure because the gas is a highly compressible fluid. Therefore, the value of q at the average pressure in the core must be used in equation (1). Assuming the used gases follow the ideal gas behavior (at low pressures), the following equation (2) is applied:

$$K(Darcy) = \frac{Q_{av}\mu L}{A(p_2 - p_1)} \quad (2)$$

## KLINKENBERG EFFECT

Klinkenberg (1941) discovered that permeability measurements made with air showed different results from permeability measurements made with a liquid. The permeability of a core sample measured by flowing air is always greater than the permeability obtained when a liquid is the flowing fluid. Klinkenberg postulated, on the basis of his laboratory experiments, that the gases exhibited slippage at the sand grain surface.

The magnitude of the Klinkenberg effect varies with the core permeability and the type of the gas used in the experiment as shown in figure (1). The resulting straight-line relationship can be expressed as: [Klinkenberg (1941)]

$$k_g = k_L + c \left[ \frac{1}{p_m} \right] \quad (3)$$

Where:

K<sub>g</sub>=measured gas permeability

P<sub>m</sub>=mean pressure

K<sub>L</sub>=equivalent liquid permeability, i.e., absolute permeability, K

C=slope of the line

Klinkenberg expressed the slope C by the following relationship:

$$C = b k_L \quad (4)$$

b=constant that depends on the size of the pore openings and is inversely proportional to radius of capillary.

Jones (1972) studied the gas slip phenomena for a group of cores for which porosity, liquid permeability k<sub>L</sub> and air permeability were determined. He correlated the parameter b with the liquid permeability by the following expression:

$$b = 6.9 k_L - 0.36 \quad (5)$$

Equations 3, 4 and 5 can be combined and arranged to give:



$$6.9K_L^{0.64} + p_m K_L - p_m K_g = 0$$

Equation (6) can be used to calculate the absolute permeability when only one gas permeability measurement ( $k_g$ ) of a core sample is made at  $p_m$ . This nonlinear equation can be solved iteratively by using the Newton-Raphson iterative methods.

## Experimental Work

The experimental work was performed in Pet. Eng. Dept./Univ. of Baghdad. The device used to determine (Kair) is shown Fig. (2).

The materials used for carrying out the experimental work are :

- 1.Core Sample: About (60) plugs are prepared and their dimensions are measured.
- 2.Gas Oil: Gas oil is used as a saturation liquid to test liquid permeability, does not volatile at room temperature.
- The properties of gas oil are given in table (1).
- 3.Air: Air is used as a gas to test absolute permeability by gas permeameter.

The experiments were carried out as follows:

- 1.The absolute permeability is measured by Ruska Liquid Permeameter with gas oil.
- 2.The gas permeability is measured by Ruska Gas Permeameter with air at different pressure drop to get equivalent liquid permeability through drawing the permeability to gas at two or three pressures drop versus the reciprocal of the mean pressure, and then extrapolating to infinite pressure.
- 3.Two correlations are built by statistical program to get equivalent liquid permeability by single test with Ruska Gas Permeameter. The correlations are:

$$K_L = f(K_g, P) \quad (7)$$

$$K_L = A_1 \times K_g^2 + A_3 \times P^A_4 \quad (8)$$

where :

$K_g$  = gas permeability ( md )

P = mean pressure (atm)

Table (2) shows the values of the constants ( $A_1, A_2, A_3$  and  $A_4$ ).

## Results

Several experiments have been carried out in this work to study the possibility of getting equation that has good agreement with equivalent liquid permeability from a single test by Ruska Gas Permeameter.

The correlations are built on about 75% of data point that covered different ranges of permeability as shown in Table (3) and use 25% of data point to check the correlations. After several trials in form of the correlations we get the final form that give acceptable agreement, as shown in Figure(3) and (4). The correlations take the Klinkenberg effect implicitly and take the effect of mean pressure explicitly, as shown in equation (8).

## Conclusions

Simple, rapid and easily applied equation is developed to calculate equivalent liquid permeability that equation needs only single measurement of gas permeability .

## References

- Ali Hussien Jawad , "Evaluation of the Engineering Properties of the Reservoir Rocks by Direct and Indirect Methods", M. Sc. thesis, Pet. Eng. Dept., University of Baghdad (1988).
- Cole, Frank, "Reservoir Engineering Manual" Houston: Gulf Publishing Company, 1969.
- Jones, S. C., "A Rapid Accurate Unsteady State Klinkenberg Parameter" SPEJ, 1972, Vol. 12, No. 5, pp. 383–397.
- Klinkenberg, L. J., "The Permeability of Porous Media to Liquids and Gases," API

*Drilling and Production Practice*, 1941, p. 200.

- Tarek Ahmed., "Reservoir Engineering Hand Book" Third Edition, Elsevier Inc. (2006).

### Symbols And Abbreviations

Symbol	Description	Unit
A	Area	[cm <sup>2</sup> ]
A <sub>1</sub> , A <sub>2</sub> , A <sub>3</sub> , A <sub>4</sub>	Correlation constants	-
b	Constant	-
c	Slope	-
C.P	centi poise	
K	Absolute permeability	[Darcy]
K <sub>g</sub>	Gas permeability	[Darcy]
K <sub>L</sub>	Liquid permeability	[Darcy]
K <sub>o</sub>	effective permeability for oil	[Darcy]
L	Length	[cm]
P <sub>1</sub>	Inlet pressure	[atm]
P <sub>2</sub>	Outlet pressure	[atm]
P <sub>m</sub>	Mean pressure	[atm]
q	Discharge	[cc/sec]
Q <sub>av</sub>	Average discharge	[cc/sec]
R	Correlation coefficient	-
V%	Variance	-

Abbreviations	Definition
He	Helium
N2	Nitrogen

### Greek symbols

Symbols	Description	Unit
$\mu$	Kinematic viscosity	[csc]

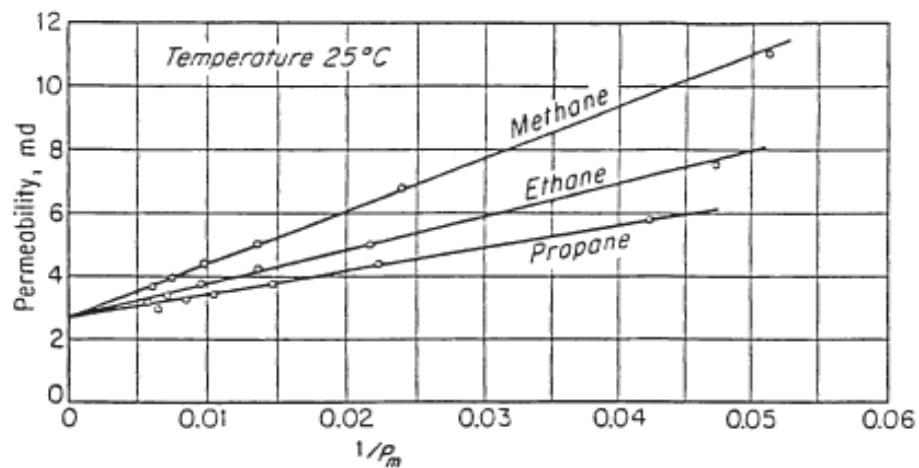
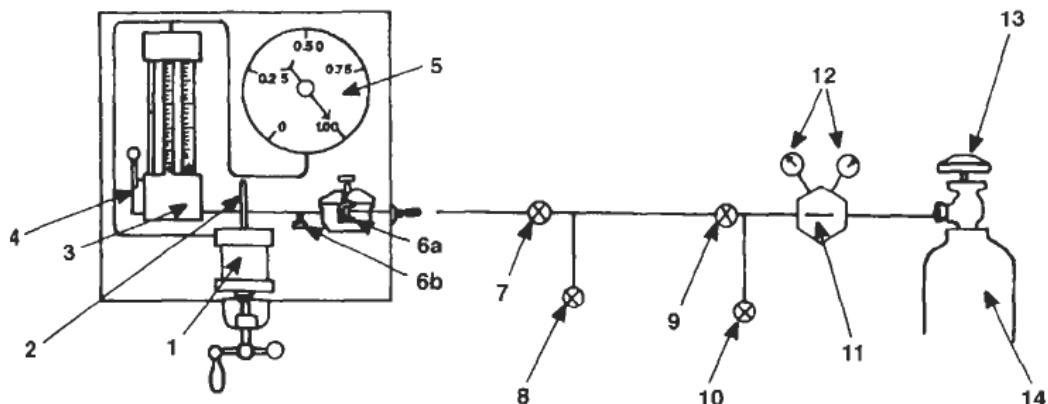


Figure (1) effect of gas pressure on measured permeability for various gases  
[Klinkenberg (1941)]



1. Core holder, 2. Thermometer, 3. Three flow meters, Small, medium, Large, 4. Flow meter selector switch, 5. Pressure gauge, 6. Pressure regulator, 7. Second flow line valve, 8. Bleed off valve, 9. First flow line valve, 10. Bleed off valve, 11. Flow line regulator, 12. Air pressure gauge, 13. Air tank valve, 14. Air.

Figure (2) Ruska gas permeameter

**Table (1). Properties of Gas oil.**

Property	Value
Sp. gr. at 24° C	0.825
Viscosity at 19 ° C (C.P.)	4.39
Viscosity at 24 ° C (C.P.)	3.7
Viscosity at 30 ° C (C.P)	3.3

**Table (2) values of the correlations coefficients**

Constants				Variance (V %)	Correlation coefficient (R)	Application range
A <sub>1</sub>	A <sub>2</sub>	A <sub>3</sub>	A <sub>4</sub>			
0.477104	1.110739	-9.4060	7.309868	93.61	0.9623	K <sub>g</sub> ≤100
1.18921	0.931348	-105.314	248.0285	98.54	0.9926	K <sub>g</sub> >100

**Table (3) values of the results calculation**

Core No.	L(mm)	D(mm)	Area(Cm <sup>2</sup> )	Pavg(atm)	ΔP(atm)	Kg(md)	KL(md)	K <sub>O</sub> (md)
1	33.96	25.19	4.98564	1.125	0.25	17.35586	2.740399	1.708781
				1.25	0.5	13.88469		
				1.5	1	13.63675		
2	26.31	25.3	5.02928	1.125	0.25	118.0615	102.7526	93.31896
				1.25	0.5	117.1094		
				1.5	1	114.253		
3	26.82	25.03	4.92251	1.125	0.25	83.2958	71.63126	62.66466
				1.25	0.5	80.32095		
				1.5	1	80.32095		
4	27.4	25.22	4.99752	1.125	0.25	374.2347	310.4828	316.2579
				1.25	0.5	368.2629		
				1.5	1	358.3098		
5	17.96	25.35	5.04918	1.125	0.25	186.4445	165.967	158.4175
				1.25	0.5	182.5603		



				1.5	1	181.2655		
6	23.21	24.94	4.88717	1.125	0.25	124.4662	110.9096	101.5286
				1.25	0.5	121.0088		
				1.5	1	121.0088		
7	37.82	25.45	5.08909	1.125	0.25	16.23058	10.89157	7.836816
				1.25	0.5	15.14854		
				1.5	1	14.87803		
8	34.51	25.42	5.0771	1.125	0.25	40.57649	0.299506	0.148432
				1.25	0.5	30.43237		
				1.5	1	30.30866		
9	26.24	25.02	4.91857	1.125	0.25	14.75841	10.2665	7.341897
				1.25	0.5	13.78746		
				1.5	1	13.59327		
10	33.63	25.45	5.08909	1.125	0.25	14	6.128824	4.154491
				1.25	0.5	13.03729		
				1.5	1	12.02702		
11	30.85	25.44	5.08509	1.125	0.25	31.79949	2.068827	1.252938
				1.25	0.5	26.49958		
				1.5	1	24.29128		
12	40.89	25.29	5.0253	1.125	0.25	829.3049	651.207	716.3055
				1.25	0.5	814.4959		
				1.5	1	784.8778		
13	40.65	25.62	5.15731	1.125	0.25	12	2.501802	1.545329
				1.25	0.5	10.61551		
				1.5	1	9.611338		
14	23.82	25.19	4.98564	1.125	0.25	79.99816	73.06468	64.05019
				1.25	0.5	79.12861		
				1.5	1	78.25907		
15	34.49	25.33	5.04121	1.125	0.25	74.71036	41.17465	39.9756
				1.25	0.5	70.97484		
				1.5	1	68.23546		
16	30.42	25.23	5.00149	1.125	0.25	270.0979	207.8752	203.109
				1.25	0.5	265.6701		
				1.5	1	254.6005		
17	29.61	25.01	4.91464	1.125	0.25	964.9403	591.7179	644.4324
				1.25	0.5	877.2184		
				1.5	1	870		
18	21.58	25.1	4.95008	1.125	0.25	117.4282	82.61604	87.83428
				1.25	0.5	115.0638		
				1.5	1	111.0807		
19	20.44	25.35	5.04918	1.125	0.25	114.9361	70.18097	73.78142
				1.25	0.5	106.0948		
				1.5	1	105.8738		
20	26.82	25.37	5.05715	1.125	0.25	162.1563	142.852	134.2486
				1.25	0.5	160.2259		
				1.5	1	157.3302		
21	31.38	25.4	5.06911	1.125	0.25	65.34619	45.39247	37.87465
				1.25	0.5	60.83955		
				1.5	1	60.27622		
22	22.21	25.01	4.91464	1.125	0.25	57.57394	24.67455	19.32622
				1.25	0.5	54.284		
				1.5	1	49.34909		

23	29.29	25.51	5.11312	1.125	0.25	143.8746	131.4736	122.496
				1.25	0.5	141.7895		
				1.5	1	140.7469		
24	25.03	25.44	5.08509	1.125	0.25	11.46683	8.656702	6.082099
				1.25	0.5	10.75015		
				1.5	1	10.75015		
25	36.19	25.42	5.0771	1.125	0.25	86.6604	72.24659	63.25908
				1.25	0.5	84.32524		
				1.5	1	83.02793		
26	41.23	24.56	4.73938	1.125	0.25	13.93304	9.566468	6.79134
				1.25	0.5	12.98306		
				1.5	1	12.82473		
27	23.16	25.34	5.04519	1.125	0.25	314.1376	227.8641	224.7705
				1.25	0.5	300.77		
				1.5	1	292.4153		
28	33.09	25.49	5.1051	1.125	0.25	7.549945	6.146748	4.167904
				1.25	0.5	7.31401		
				1.5	1	7.196042		
29	27.85	25.38	5.06113	1.125	0.25	66.09866	54.18614	46.05025
				1.25	0.5	64.09567		
				1.5	1	63.09417		
30	22.79	24.97	4.89894	1.125	0.25	677.3357	508	544.5687
				1.25	0.5	660.4023		
31	30.59	25.54	5.12515	1.25	0.5	11.29738	8.6903	6.108159
				1.5	1	10.86287		
32	16.47	25	4.91071	1.125	0.25	292.9959	220.3895	216.6464
				1.25	0.5	280.7877		
				1.5	1	274.6837		
33	23.83	25.6	5.14926	1.125	0.25	7.3	2.321914	1.423154
				1.25	0.5	7.07506		
				1.5	1	6.064337		
34	27.33	25.25	5.00942	1.125	0.25	714.9178	516.33	554.4331
				1.25	0.5	695.059		
35	21.95	25.18	4.98168	1.125	0.25	237.3676	170.8085	163.5259
				1.25	0.5	224.537		
				1.5	1	220.5274		
36	33.44	25.4	5.06911	1.125	0.25	86.44464	67.61386	58.797
				1.25	0.5	81.64216		
				1.5	1	81.64216		
37	29.04	25.2	4.9896	1.125	0.25	699.1111	487.26	520.0816
				1.25	0.5	677.9259		
38	27.35	24.66	4.77805	1.125	0.25	895.9347	636.9497	699.0156
				1.25	0.5	833.4277		
				1.5	1	830		
39	19.66	25.33	5.04121	1.125	0.25	93.69012	75.55354	66.46256
				1.25	0.5	89.43148		
				1.5	1	89.07659		
40	26.24	25.42	5.0771	1.125	0.25	808.943	620.82	679.5035
				1.25	0.5	790.1304		
41	31.59	25.16	4.97377	1.125	0.25	1017.227	750.861	838.214
				1.25	0.5	970.9891		



				1.5	1	950		
42	29.33	25.52	5.11712	1.125	0.25	12.51811	9.624668	6.836958
				1.25	0.5	12.01738		
				1.5	1	11.78789		
43	31.4	25.53	5.12114	1.125	0.25	214.2575	183.1878	176.6552
				1.25	0.5	209.7938		
				1.5	1	206.446		
44	36.33	25.73	5.20169	1.125	0.25	73.72598	63.59033	54.94726
				1.25	0.5	72.45484		
				1.5	1	71.18371		
45	30.7	25.5	5.10911	1.125	0.25	126.8594	100.5551	91.11862
				1.25	0.5	124.6722		
				1.5	1	120.2977		
46	30.22	24.9	4.87151	1.125	0.25	677.4134	498.8496	533.752
				1.25	0.5	643.5427		
				1.5	1	632.2525		
47	42.63	25.32	5.03723	1.125	0.25	147.8652	117.5869	108.296
				1.25	0.5	140.78		
				1.5	1	140.1639		
48	30.94	25	4.91071	1.125	0.25	110.0825	83.10504	73.83157
				1.25	0.5	103.2023		
				1.5	1	103.2023		
49	36.28	24.91	4.87542	1.125	0.25	1164.729	844.2025	953.9414
				1.25	0.5	1083.469		
				1.5	1	1083		
50	27.13	25.28	5.02133	1.125	0.25	62.93357	55.19626	46.99869
				1.25	0.5	61.16356		
				1.5	1	60.9669		
51	19.18	25.33	5.04121	1.125	0.25	285.2871	224.6436	221.2667
				1.25	0.5	276.9778		
				1.5	1	270.0533		
52	42.9	25.36	5.05316	1.125	0.25	129.7911	105.5569	96.13401
				1.25	0.5	123.6105		
				1.5	1	123.6105		
53	22.41	25.48	5.1011	1.125	0.25	9.594691	6.312297	4.291975
				1.25	0.5	9.914514		
				1.5	1	8.795133		
54	31.82	25.44	5.08509	1.125	0.25	9.11093	5.985042	4.047046
				1.25	0.5	8.313723		
				1.5	1	8.313723		
55	38.12	25.51	5.11312	1.125	0.25	16.5	8.71269	6.125532
				1.25	0.5	14.65421		
				1.5	1	14.51852		
56	29.41	24.62	4.76256	1.125	0.25	71.92927	54.30187	46.15882
				1.25	0.5	67.43369		
				1.5	1	67.43369		

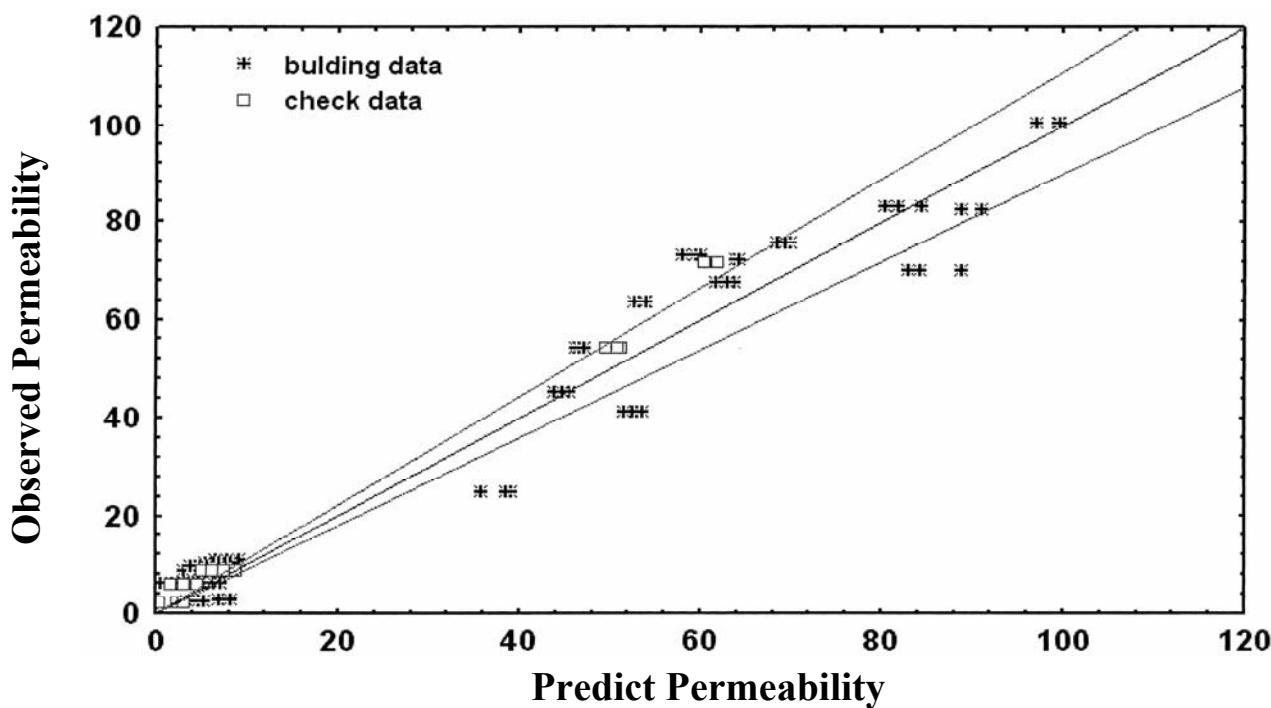


Figure (3) predict versus observed values of  $K_L, K_g \leq 100$

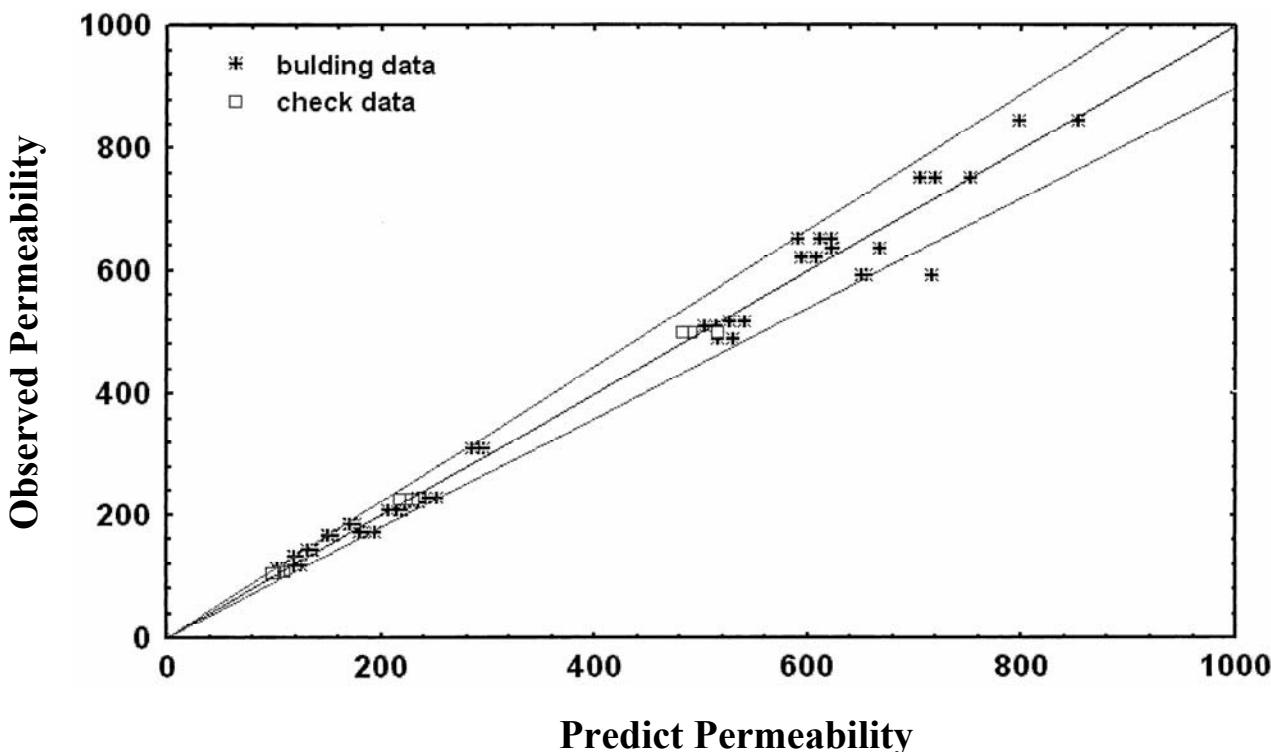


Figure (3) predict versus observed values of  $K_L, K_g > 100$



## Adsorption Of Phenol And P-Nitro Phenol Onto Date Stones: Equilibrium Isotherms, Kineticsand Thermodynamics Studies

Muthanna J. Ahmed, Samar K. Theydan, Abdul-Halim A.K. Mohammed

Chemical Engineering Department - Engineering College - Baghdad University -Iraq.

### Abstract

Adsorption capacity of a waste biomass, date stones, for phenolic compounds such as phenol (Ph) and p-nitro phenol (PNPh) was investigated. The characteristics of such waste biomass were determined and found to have a surface area and iodine number of  $495.71 \text{ m}^2/\text{g}$  and  $475.88 \text{ mg/g}$ , respectively. The effects of temperature, initial sorbate concentration, and contact time on the adsorption process were studied. Experimental equilibrium data for adsorption of Ph and PNPh on date stones were analyzed by the Langmuir, Freundlich and Sips isotherm models. The results show that the best fit was achieved with the Sips isotherm equation with maximum adsorption capacities of 147.09 and  $179.62 \text{ mg/g}$  for Ph and PNPh, respectively. The kinetic data were fitted to pseudo-first order, pseudo-second order and intraparticle diffusion models, and was found to follow closely the pseudo-second order model for both Ph and PNPh. The calculated thermodynamic parameters, namely  $\Delta G$ ,  $\Delta H$ , and  $\Delta S$  showed that adsorption of Ph and PNPh onto date stones was spontaneous and endothermic under examined conditions.

### الخلاصة

يهدف البحث إلى دراسه استخدام نوى التمر لازاله الملوثات الفينوليه مثل الفينول والبارا نايتروفينول من مخلفات المياه. تم تحديد المساحه السطحية والرقم الايديني لنوى التمر وهي  $495.71 \text{ m}^2/\text{gram}$  و  $475.88 \text{ mg/g}$  على التوالي. تم دراسة تأثير درجه الحراره ، التركيز الاولى للماده الملوشه ، وزمن الامتاز على سعه امتاز نوى التمر. تم تمثيل نتائج امتاز الفينول والبارانايتروفينول على نوى التمر يشكل جيد جدا بواسطه معادله سيس، حيث تم الحصول على اعلى سعه امتاز للفينول (147.09 ملي غرام/غرام) والبارانايتروفينول (179.62 ملي غرام/غرام). ايضا تم دراسه حركيه عمليه الامتاز وبينت النتائج ان معادله الدرجه الثانيه مثلت النتائج التجربيه لعمليه الامتاز بشكل جيد لكل من الفينول والبارانايتروفينول. بينت نتائج دراسه ثرموديناميكيه العمليه ان الامتاز من النوع الماصل للحراره لكل من الفينول والبارانايتروفينول .

**Keywords:** Date stones, phenol, p-nitro phenol, adsorption isotherms, kinetics.

## Introduction

Wastewaters from paint, pesticide, coal conversion, polymeric resin, gasoline, rubber proofing, steel, petroleum, and petrochemical industries contain considerable amounts of phenols. These pollutants are known to be toxic, carcinogenic, and posing serious hazards to aquatic living organisms. Phenol (Ph) and p-nitro phenol (PNPh) are the most hazardous polluting phenols to the environment. The presence of Ph even at low concentrations can cause unpleasant taste and odor of drinking water. PNPh can enter the human body through all routes and reacts easily in the blood to convert hemoglobin to methemoglobin, thereby preventing oxygen uptake. Indeed, it is necessary to remove these pollutants from wastewaters before discharge into the environment (Zhu et al., 2000).

Various processes have been employed for the removal of phenols from aqueous media including chemical oxidation (He et al., 2009), membrane filtration (Kujawski et al., 2004), biodegradation (El-Naas et al., 2009), electro coagulation (Ugurlu et al., 2008), photo degradation (Gomez et al., 2011), solvent extraction (Xu et al., 2006), and adsorption (Yang et al., 2008). Among these methods adsorption is still the most popular and widely used technique for phenols removal, because of its simple design, easy operation, and relatively simple regeneration (Nevskaja et al., 2004).

In the design and optimization of adsorption processes the adsorption isotherms and kinetics are of utmost importance to study. Adsorption isotherms are important for the description of how adsorbate will interact with adsorbent and are critical in optimizing the use of adsorbent. Thus, the correlation of experimental equilibrium data using either a theoretical or empirical equation is essential for adsorption data prediction. Adsorption kinetics involves the study of the rate at which pollutants are removed from aqueous

solution onto adsorbent surface, which in turn controls the residence time of the adsorbate uptake at the solid-solution interface (Altenor et al., 2009).

Currently adsorption on activated carbon is widely used for removal of phenols, but it is still considered expensive material (Sulaymon and Ahmed, 2008). Recently agricultural waste biomass, have been investigated intensively as adsorbents for removal of pollutants from aqueous solutions. Because these materials are cheaper, renewable and abundantly available; also constitute an environmental problem (Adiuata et al., 2007). Date stones can be considered as one of the best candidate among the agricultural wastes because it is cheap and quite abundant, especially in Mediterranean countries. Carbohydrates are the major components of date stones; they are composed of 42% cellulose, 18% hemi cellulose, 25% sugar and other compounds, 11% lignin and 4% ash. This lignocellulosic composition promotes the use of date stones as adsorbents for removal of pollutants. Date stones as a waste stream have been a problem to the palm oil and palm syrup factories. Therefore, its recycling or reutilization is useful (Hameed et al., 2009).

Many studies have been done on adsorption isotherms and kinetics of phenols on various agricultural wastes and natural materials such as red mud (Gupta et al., 2004), soil (Subramanyam and Das, 2009), chitin (Durmus and Kalayci, 2005), clinoptilolite rock (Sprynsky et al., 2009), lignite (Polat et al., 2006), olive pomace (Stasinakis et al., 2008), deoiled soya (Mittal et al., 2009), wood fly ash (Daifullah and Gad, 1998), mauritanian clay (Ely et al., 2011), mansonia wood sawdust (Ofomaja, 2011), rice husk (Ahmaruzzaman and Sharma, 2005), chitosan (Li et al., 2009), and alignate (Peretz and Cintea, 2008). Though date stones-based activated carbon has been widely used to remove phenols



from wastewaters (Alhamed, 2009; El-Naas et al., 2010; Alhamed, 2008), literature is scant where raw date stones were employed directly for phenols adsorption.

Therefore, the main objective of the present work is to study experimentally and theoretically the equilibrium isotherms, kinetics, and thermodynamics of Ph and PNPh adsorption onto raw date stones.

## Materails And Methods

### Materials

Date stones were used as adsorbent. Stones as received were first washed with water to get rid of impurities, dried at 110 °C for 24 h, crushed using disk mill, and sieved. Fraction of average particle size of 250 µm was selected for the study. The properties of chemicals used are listed in Table 1.

### Adsorbent characteristics

Date stones were characterized by selected physical properties including bulk density and surface area, chemical properties including ash and moisture contents, and adsorption properties including iodine number. The details of characterization methods are illustrated as follows.

### Bulk density

Bulk or apparent density was determined according to procedure followed by Ahmedna et al. (1997). 10 ml cylinder was filled to a specified volume with date stones that had been dried in an oven at 80 °C for 24 h (Ahmedna et al., 1997). The bulk density was then calculated as follows:

$$\text{bulk density} = \frac{W_c}{V_c} \quad (1)$$

Where  $W_c$  is the weight of dried adsorbent (g) and  $V_c$  is cylinder volume packed with dried adsorbent (ml).

### Ash content

The ash content of date stones was determined by standard methods (ASTM standard, 2000). 0.5 g of date stones with average particle size of 0.250 mm was dried at 80 °C for 24 h and placed into weighted ceramic crucibles. The samples were heated in an electrical furnace at 650 °C for 3 h. Then the crucibles were cooled to ambient temperature and weighed. The percent of ash was calculated as follows:

$$\text{ash (\%)} = \frac{W_{s3} - W_{s2}}{W_{s1}} \times 100 \quad (2)$$

Where  $W_{s3}$  is the weight of crucible containing ash (g),  $W_{s2}$  is the weight of crucible (g), and  $W_{s1}$  is the weight of original adsorbent used (g).

### Moisture content

The moisture content of date stones was determined using oven drying method (Adekola and Adegoke, 2005). 0.5 g of adsorbent with average particle size of 250 mm was placed into weighed ceramic crucible. The samples were dried at 110 °C to constant weight. Then the samples were cooled to ambient temperature and weighed. The moisture content was calculated by the following equation:

$$\text{moisture (\%)} = \frac{W_{m3} - W_{m2}}{W_{m1}} \times 100 \quad (3)$$

Where  $W_{m3}$  is the weight of crucible containing original sample (g),  $W_{m2}$  is the weight of crucible containing dried sample (g), and  $W_{m1}$  is the weight of original sample used (g).

### Iodine number

Iodine number which is a measure of the micropore content of structure (0 to 20 Å) was determined as follows: 10 ml of 0.1 N iodine solution in a conical flask is titrate

with 0.1 N sodium thiosulfate solution in the presence of 2 drops of 1 wt% starch solution as an indicator, till it becomes colourless. The burette reading is corresponding to  $V_b$ . Then weigh very accurately 0.05 g of date stones and add it to conical flask containing 15 ml of 0.1 N iodine solution, shake the flask for 4 min and filter it, then titrate 10 ml of filtrate with standard sodium thiosulfate solution using 2 drops of starch solution as indicator, now the burette reading is corresponding to  $V_s$ . The iodine number was then calculated by using the following equation (Lubrizol, 2007):

$$IN = \frac{(V_b - V_s) \cdot N \cdot (126.9) \cdot (15/10)}{M} \quad (4)$$

Where IN is iodine number (mg/g),  $V_b$  and  $V_s$  are volumes of sodium thiosulfate solution required for blank and sample titrations (ml), respectively, N is the normality of sodium thiosulfate solution (mole/l), 126.9 is atomic weight of iodine, and M is the mass of adsorbent used (g).

### Surface area

The surface area of the date stones was estimated through a calibration curve which has a correlation coefficient of 0.997 between the iodine numbers and BET surface area from the literature (Fadhil and Deyab, 2008) as shown in Fig. 1.

### Adsorption isotherms

The equilibrium isotherms of Ph and PNPh adsorption on date stones were determined by performing adsorption tests in 100 ml Erlenmeyer flasks where 40 ml of Ph or PNPh solutions with different initial concentrations (50-250 mg/l) was placed in each flask. The pH of the solutions was gradually adjusted to 7 by adding small amounts of 0.1 M HCl or NaOH solution. 0.02 g of date stones, with particle size of 250  $\mu\text{m}$ , was added to each flask and kept in

a shaker of 120 rpm at different temperatures (303-323 K) for 90 min to reach equilibrium. Then the samples were filtered and the residual concentrations of Ph or PNPh in the filtrate were analyzed by a UV-Visible Spectrophotometer (Shimadzu UV-160A) at maximum wave lengths of 269 and 400 nm for Ph and PNPh, respectively. The uptake of Ph or PNPh at equilibrium,  $q_e$  (mg/g) was calculated by the following expression:

$$q_e = \frac{(C_o - C_e)V}{W} \quad (5)$$

Where  $C_o$  and  $C_e$  (mg/L) are the initial and equilibrium concentrations of Ph or PNPh solution, respectively, V (L) is the volume of solution, and W (g) is the weight of date stones.

Three famous isotherm equations, namely the Langmuir (1916), Freundlich (1906), and Sips (1948) were applied to fit the experimental isotherm data of Ph and PNPh adsorption on date stones. These equations can be written as:

Langmuir isotherm

$$q_e = \frac{q_L K_L C_e}{1 + K_L C_e} \quad (6)$$

Freundlich isotherm

$$q_e = K_F C_e^{1/n} \quad (7)$$

Sips isotherm

$$q_e = \frac{q_S K_S C_e^{1/m}}{1 + K_S C_e^{1/m}} \quad (8)$$

Where  $q_L$  (mg/g) is the Langmuir maximum uptake of Ph or PNPh per unit mass of date stones,  $K_L$  (L/mg) is the Langmuir constant related to rate of adsorption,  $K_F$  ((mg/g).(L/mg) $^{1/n}$ ) and n are Freundlich constants which give a measure of adsorption capacity and adsorption intensity, respectively,  $q_S$  (mg/g) is the Sips maximum uptake of Ph or PNPh per unit mass of date stones,  $K_S$  (L/mg) $^{1/m}$  is Sips constant related



to energy of adsorption, and parameter m could be regarded as the Sips parameter characterizing the system heterogeneity. Least-squares regression program based on Hooke-Jeeves and Gauss-Newton method was used to analyze experimental data. This program gave the parameters of each equation and the agreement between experimental and calculated data in terms of correlation coefficient  $R^2$ .

### Adsorption kinetics

The procedure used for kinetic tests was identical to that used for equilibrium experiments. The aqueous samples were taken at present time intervals, and the concentrations of Ph or PNPh were similarly measured. The uptake of Ph or PNPh at time t,  $q_t$  (mg/g), was calculated by:

$$q_t = \frac{(C_o - C_t) V}{W} \quad (9)$$

Where,  $C_t$  (mg/L) is the liquid-phase concentration of Ph or PNPh solution at time t (min). Pseudo-first order model (Langeren and Svenska, 1898), pseudo-second order model (Ho and Mckay, 1999), and intraparticle diffusion model (Weber and Morris, 1963) were used to analyze the kinetic data. These models can be expressed as:

#### Pseudo-first order model

$$\ln(q_t - q_e) = \ln(q_e) - K_1 t \quad (10)$$

#### Pseudo-second order model

$$\frac{t}{q_t} = \frac{1}{K_2 q_e} + \frac{t}{q_e} \quad (11)$$

#### Intraparticle diffusion model

$$q_t = K_3 t^{1/2} + C \quad (12)$$

Where  $q_e$  and  $q_t$  (mg/g) are the uptake of Ph or PNPh at equilibrium and at time t (min), respectively,  $K_1$  (1/min) is the adsorption rate constant,  $K_2$  (g/mg.min) is the rate constant of second-order equation,  $K_3$

(mg/g.min<sup>1/2</sup>) is the intraparticle diffusion rate constant, and C (mg/g) is a constant that gives an idea about the thickness of the boundary layer..

### Adsorption thermodynamics

Thermodynamic behavior of the adsorption of Ph and PNPh on date stones was evaluated by the thermodynamic parameters including the change in free energy ( $\Delta G$ ), enthalpy ( $\Delta H$ ), and entropy ( $\Delta S$ ). These parameters are calculated from the following equations:

$$\ln(K_d) = \frac{\Delta S}{R} - \frac{\Delta H}{RT} \quad (13)$$

$$\Delta G = -RT \ln(K_d) \quad (14)$$

$$K_d = \frac{q_e \cdot (W/V)}{C_e} \quad (15)$$

Where, R is the universal gas constant (8.314 J/mole.K), T is temperature (K), and  $K_d$  is the distribution coefficient for the adsorption.

## RESULTS AND DISCUSSION

### Adsorbent characteristics

The characteristics of date stones were determined and summarized in Table 2. The most important characteristics are surface area and iodine number, and the results showed that their values are 495.71 m<sup>2</sup>/g and 475.88 mg/g, respectively. This high surface area for an agricultural waste biomass enables date stones to be used successively for removal of dyes from aqueous solutions, as explained by Belala et al. (2011) and Banat et al. (2003). Also this high iodine number which is a measure of micropore content (0 to 20 Å), can be a good indication

for the capability of date stones to remove most of phenols which have molecular sizes in the range of micropores content (Lu and Sorial, 2007).

### Effect of contact time

The effect of contact time on uptakes of Ph and PNPh onto date stones is shown in Fig. 2. This figure shows that the uptake of both adsorbate increases with the increase of contact time, and the adsorption reached equilibrium in about 90 min. Maximum uptakes of 59.77 and 65.79 mg/g for Ph and PNPh, respectively, are reported at 90 min contact time, 50 mg/L initial concentration, 7 pH, and 0.5 g/L adsorbent dose. Fig. 2 also shows that rapid increase in uptakes of Ph and PNPh is observed during the first 15 min. The fast adsorption at the initial stage may be due to the higher driving force making fast transfer of Ph and PNPh ions to the surface of date stone particles and the availability of the uncovered surface area and the remaining active sites on the adsorbent (Aroua et al., 2008).

### Adsorption isotherms

The experimental equilibrium data for Ph and PNPh adsorption on date stones, calculated from Eq. (5), are fitted with Langmuir, Freundlich and Sips isotherms, Eqs.(6)-(8). The calculated constants of the three isotherm equations along with  $R^2$  values are presented in Table 3. This table shows that the Sips isotherm correlates experimental data with highest  $R^2$  values for both Ph and PNPh at three different temperatures. Also this table shows that the Sips isotherm gave maximum adsorption capacities of 147.09 and 179.62 mg/g for Ph and PNPh, respectively. The equilibrium data for Ph and PNPh correlated with Sips isotherm are shown in Figs. 3 and 4,

respectively. It can be seen from these figures that the uptake of PNPh is higher than that of Ph; this may be due the smaller molecular size of Ph as compared with that of PNPh. This implies that only a small part of the micropores is filled in Ph adsorption, and the micropore phenomenon is more evident for PNPh, as explained by Liu et al. (2010). Also these figures show that the adsorption capacities of Ph and PNPh increases with increasing temperature, which indicate the endothermic nature of adsorption on date stones. Table 4 lists a comparison of Ph and PNPh adsorption capacities for the date stones with those for different agricultural and natural adsorbents. It can be seen that date stones can be classified as one of the effective adsorbents for this purpose.

### Effect of temperature

Fig. 5 shows the maximum adsorption capacities of date stones for Ph and PNPh, calculated from sips isotherm, versus temperature. It can be seen that the increase in temperature from 303 to 323 K leads to an increase in adsorption capacity from 125.26 to 147.09 mg/g for Ph and from 152.66 to 179 .62 mg/g for PNPh. This is an indication for endothermic nature of the adsorption of Ph and PNPh on date stones. Similar trend was reported by Al-Mutairi (2010) for adsorption of 2, 4-dinitrophenol on date stones. It was explained that as temperature increased, the surface activity and kinetic energy of 2, 4-dinirphenol also increased which caused the interaction forces between the solute and adsorbent to become stronger than solute and solvent.

### Adsorption kinetics

The experimental kinetic data for Ph and PNPh adsorption on date stones, calculated from Eq. (9), are fitted with pseudo-first order, pseudo-second order and intraparticle diffusion models, Eqs. (10)- (12), and



presented in Figs. 6, 7 and 8, respectively. The calculated constants of the three isotherm equations along with  $R^2$  values at 50 mg/L initial adsorbate concentration are presented in Table 5. The linear plot of  $\ln(q_e - q_t)$  versus  $t$  (Fig. 6) for pseudo-first order equation is of low  $R^2$  values for both Ph and PNPh, as shown in Table 5. Also, there is a large difference between the experimental and calculated adsorption capacity for both adsorbates, indicating a poor pseudo-first order fit to the experimental data. High  $R^2$  values are obtained for the linear plot of  $t/q_t$  versus  $t$  (Fig. 7) for pseudo-second order equation, as shown in Table 5. It can be seen that the pseudo-second order kinetic model better represented the adsorption kinetics and the calculated  $q_e$  values agree well with the experimental  $q_e$  values for both Ph and PNPh (Table 5). This suggests that the adsorption of Ph and PNPh on date stones follows second-order kinetics. A similar result was reported by Ofomaja (2011) for the adsorption of PNPh on mansonia wood sawdust. From Table 5, the value of rate constant  $K_2$  for PNPh is lower than that for Ph, this probably due to the low adsorption capacity of Ph as compared to that of PNPh. On the other hand, for the intraparticle diffusion model, the low values of  $R^2$  (Table 5) for the linear plot of  $q_t$  versus  $t^{1/2}$  (Fig. 8) indicate that this model could not fit properly the experimental kinetic data.

### Adsorption thermodynamics

According to Eqs.(13)-(15), the  $\Delta H$  and  $\Delta S$  parameters for Ph and PNPh can be calculated from the slope and intercepts of the plot of  $\ln(K_d)$  versus  $1/T$  (Fig. 9). The calculated values of  $\Delta H$ ,  $\Delta S$ , and  $\Delta G$  are listed in Table 6.

The obtained values for Gibbs free energy change ( $\Delta G$ ) are -1090.79, -1347.98, and -1860.99 J/mole for Ph and -1770.96, -2443.52, and -3227.88 J/mole for PNPh adsorption on date stones at 303, 313, and 323 K, respectively. The negative  $\Delta G$  values indicate thermodynamically spontaneous

nature of the adsorption. The increase in  $\Delta G$  values with increasing temperature shows an increase in feasibility of adsorption at higher temperatures. The  $\Delta H$  parameters are 10535.30 and 20277.34 J/mole for Ph and PNPh adsorption on date stones, respectively. The positive  $\Delta H$  is an indicator of endothermic nature of the adsorption and also its magnitude gives information on the type of adsorption, which can be either physical or chemical. The enthalpy of adsorption, ranging from 2.1 to 20.9 kJ/mole corresponds to a physical sorption. The adsorption heat of Ph and PNPh is in range of physisorption. Therefore, the  $\Delta H$  values show that the adsorption of Ph and PNPh on adsorbent was taken place via physisorption.

The  $\Delta S$  values are 38.24 and 72.71 J/mole for Ph and PNPh, respectively. The positive  $\Delta S$  value suggests an increase in the randomness at sorbate-solution interface during the adsorption process.

### Acknowledgement

We gratefully acknowledge university of Baghdad for assist and support of this work.

### NOMENCLATURE

C	: Intraparticle diffusion kinetic model constant (mg/g)
$C_e$	: Equilibrium concentrations of Ph or PNPh solution (mg/L)
$C_o$	: Initial concentrations of Ph or PNPh solution (mg/L)
$C_t$	: Concentration of Ph or PNPh at time $t$ (mg/L)
IN	: Iodine number (mg/g)
$K_1$	: First order kinetic model constant (1/min)
$K_2$	: Second order kinetic model constant (g/mg.min)
$K_3$	: Intraparticle diffusion rate constant (mg/g.min <sup>1/2</sup> )
$K_d$	: Adsorption distribution Coefficient
$K_F$	: Freundlich isotherm equation constant ((mg/g).(L/mg) <sup>1/n</sup> )
$K_L$	: Langmuir isotherm equation

$K_S$	constant (L/mg)
	: Sips isotherm equation constant (L/mg) <sup>1/m</sup>
$m$	: Sips isotherm equation parameter
$M$	: Mass of adsorbent used (g).
$n$	: Freundlich isotherm equation constant
$N$	: Normality of sodium thiosulfate solution (mole/l)
$Ph$	: Phenol
$PNPh$	: P-nitro phenol
$q_e$	: Uptake of Ph or PNPh at equilibrium (mg/g)
$q_L$	: Langmuir maximum uptake of Ph or PNPh per unit mass of date stones (mg/g)
$q_s$	: Sips maximum uptake of Ph or PNPh per unit mass of date Stone (mg/g)
$q_t$	: Uptake of Ph or PNPh at time t (mg/g)
$R$	: Universal gas constant (8.314 J/mole.K)
$R^2$	: Correlation coefficient
$T$	: Temperature (K)
$V$	: Volume of solution (L)
$V_b$	: Volume of sodium thiosulfate solution required for blank titration (ml)
$V_c$	: Cylinder volume packed with dried adsorbent (ml).
$V_s$	: Volume of sodium thiosulfate solution required for sample titration (ml)
$W$	: Weight of date stones (g)
$W_c$	: Weight of dried adsorbent (g)
$W_{m1}$	: Weight of original sample used (g).
$W_{m2}$	: Weight of crucible containing dried sample (g).
$W_{m3}$	: Weight of crucible containing original sample (g).
$W_{s1}$	: Weight of original adsorbent used (g).
$W_{s2}$	: Weight of crucible (g)
$W_{s3}$	: Weight of crucible containing ash (g)
$\Delta H$	: Change in enthalpy (J/mole)

$\Delta G$  : Change in free energy (J/mole)  
 $\Delta S$  : Change in entropy (J/mole.K)

## References

- Adekola F.A. and Adegoke H.I., (2005), Adsorption of blue-dye on activated carbons produced from Rice Husk, Coconut Shell and Coconut Coir pitch, Ife J. Sci., 7(1), 151-157.
- Adiuata D., Wan Daud W.M.A., and Aroua M.K., (2007), Preparation and characterization of activated carbon from palm shell by chemical activation with  $K_2CO_3$ , Bioresour. Technol., 98, 145-149
- Ahmedna M., Marshall W.E., Rao R.M., and Clarke S.J., (1997), Use of filtration and buffers in raw sugar color measurement, J. Sci. Food Agric., 75(1), 109-116.
- Alhamed Y.A., (2008), Phenol removal using granular activated carbon from date stones, Bulg. Chem. Comm., 40 (1), 26-35.
- Alhamed Y.A., (2009), Adsorption kinetics and performance of packed bed adsorber for phenol removal using activated carbon from dates stones, J. Hazard. Mater., 170, 763-770.
- Al-Mutairi N.Z., (2010), 2,4-Dinitro phenol adsorption by date seeds: Effect of phsico-chemical environment and regeneration study, Desalination, 250, 892-901.
- Altenor S., Carene B., Emmanuel E., Lambert J., and Gaspard S., (2009), Adsorption studies of methylene blue and phenol onto vetiver roots activated carbon prepared by chemical activation, J. Hazard. Mater., 165, 1029-1039.
- Ahmaruzzaman M., Sharma D.K., (2005), Adsorption of phenols from wastewater, J. Colloid & Interf. Sci., 287 (2005) 14-24.



Aroua M.K., Leong S.P.P., Teo L.Y., and Daud W.M.A.W., (2008), Real time determination of kinetics of adsorption of lead (II) onto shell based activated carbon using ion selection electrode, *Bioresou. Technol.*, 99, 5786-5792.

ASTM standard, (2000), Standard test method for total ash content of activated carbon, Designation D2866-94.

Banat F., Al-Asheh S., and Al-Makhadmeh L., (2003), Evaluation of the use of raw and activated date pits as potential adsorbents for dye containing waters, *Process Biochem.*, 39, 193-202.

Belala Z., Jeguirim M., Belhachemi M., Addoun F., and Trouve G., (2011), Biosorption of basic dye from aqueous solutions by date stones and palm-trees waste: kinetics, equilibrium, and thermodynamic studies, *Desalination*, 271, 80-87.

Daifullah A.E.H., Gad H., (1998), Sorption of semi-volatile organic compounds by bottom and fly ashes using HPLC Adsorp. *Sci. Technol.*, 16, 273-283.

Dursun A.Y., Kalayci C.S., (2005), Equilibrium, kinetic, and thermodynamic studies on the adsorption f phenol onto chitin, *J. Hazard. Mater.*, B123, 151-157.

El-Naas M.H., Al-Muhtaseb S.A. and Makhlouf S., (2009), Biodegradation of phenol by pseudomonas putida immobilized in polyvinyl alcohol (PVA) gel, *J. Hazard. Mater.*, 164, 720-725.

El-Naas M.H., Al-Zuhair S., and Abu Alhaija M., (2010), Removal of phenol from petroleum refinery wastewaters through adsorption on date-pit activated carbon, *Chem. Eng. J.*, 162, 997-1005.

Ely A., Baudu M., Ould Kankou M.O.S.A., Basly J.P., (2011), Copper and nitro phenol removal by low cost alginato-mauritanian clay composite beads, *Chem. Eng. J.*, 178, 168-174.

Fadhil A.B. and Deyab M.M., (2008), Conversion of some fruit stones and shells into activated carbons, *The Arabain Journal for Science and Engineering*, 33(2A), 175-184.

Freundlich H.M.F., (1906), Über die adsorption in lösungen, *Z. Phys. Chem.*, 57, 385-470.

Gomez M., Murcia M.D., Gomez E., Gomez J.L., and Christofi N., (2011), Degradation of phenolic pollutants using KrCl and XeBr excilamps in the presence of dye: A comparative study, *Desalination*, 274, 156-163.

Gupta V.K., Ali I., Saini V.K., (2004), Removal of chloro phenols from wastewaters using red mud: an aluminum industry waste, *Environ. Sci. Technol.*, 38, 4012-4018

Hameed B.H., Salman J.M., and Ahmad A.L., (2009), Adsorption isotherm and kinetic modeling of 2,4-D pesticide on activated carbon derived from date stones, *J. Hazard. Mater.*, 163, 121-126.

He D., Guan X., Ma J., Yu M., (2009), Influence of different nominal molecular weight fractions of humic acids on phenol oxidation by permanganate, *Environ. Sci. Technol.*, 43(21), 8332-8337.

Ho Y.S. and Mckay G., (1999), Pseudo-second order model for sorption processes, *Process Biochem.*, 34, 451-465.

Lubrizol standard test method, (2006), Iodine value, test procedure AATM 1112-01, October 16.

- Langeren S. and Svenska B.K., (1898), Zur theorie der sogenannten adsorption geloester stoffe, Veteruskapsakad Handlingar, 24(4), 1-39.
- Langmuir I., (1916), The constitution and fundamental properties of solids and liquids, *J. Am. Chem. Soc.*, 38, 2221-2295.
- Li J.M., Meng X.G., Hu G.W., Du J., (2009), Adsorption of phenol, p-chloro phenol and p-nitro phenol onto functional chitosan, *Bioresour. Technol.*, 100, 1168-1173.
- Liu Q.S., Zheng T., Wang P., Jiang J.P., and Li N., (2010), Adsorption isotherm, kinetic and mechanism studies of some substituted phenols on activated carbon fibers, *Chem. Eng. J.*, 157, 348-356.
- Lu Q. and Sorial G.A., (2007), The effect of functional groups on oligomerization of phenolics on activated carbon, *J. Hazard. Mater.*, 148, 436-445.
- Kujawski W., Warszawski A., Ratajczak W., and Capala W., (2004), Removal of phenol from waste water by different separation techniques, *Desalination*, 163, 287-296.
- Mittal A., Kaur D., Malviya A., Mittal J., and Gupta V.K., (2009), Adsorption studies on the removal of coloring agent phenol red from wastewaters using waste materials s adsorbents, *J. Colloid and Interf. Sci.*, 337, 345-354.
- Nevskaya D.M., Castillejos-Lopez E., Munoz V., Guerrero-Ruiz A., (2004), Adsorption of aromatic compounds from water by treated carbon materials, *Environ. Sci. Technol.*, 38(21), 5786-5796.
- Ofomaja A.E., (2011), Kinetics and pseudo-isotherm studies of 4-nitrophenol adsorption onto mansonia wood sawdust, *Ind. Crops and Products*, 33, 418-428.
- Peretz S., Cinteza O., (2008), Removal of some nitro phenol contaminants using aligate gel beads, *Colloid & Surfaces A: Physicochem. Eng. Aspects*, 319, 165-172.
- Polat H., Molva M., and Polat M., (2006), Capacity and mechanism of phenol adsorption on lignite, *Int. J. Miner. Process.*, 79, 264-273.
- Sips R., (1948), Combined form of Langmuir and Freundlich equations, *J. Chem. Phys.*, 16, 490-495.
- Sprynskyy M., Ligor T., Lebedynets M., and Buszewski B., (2009), Kinetics and equilibrium studies of phenol adsorption by natural and modified forms of clinoptilolite, *J. Hazard. Mater.*, 169, 847-854.
- Stasinakis A.S., Elia I., Petalas A.V., Halvadakis C.P., (2008), Removal of total phenols from olive-mill waste water using an agricultural-byproduct olive pomace, *J. Hazard. Mater.*, 160, 408-413.
- Subramanyam B. and Das A., (2009), Study of the adsorption of phenol by two soil based on kinetic and equilibrium modeling analysis, *Desalination*, 249, 914-921.
- Sulaymon A.H., Ahmed K.W., (2008), Competitive adsorption of furfural and phenolic compounds onto activated carbon in fixed bed column, *Environ. Sci. Technol.*, 42(2), 392-397.
- Ugurlu M., Gurses A., Dogar C. and Yalcin M., (2008), The removal of lignin and phenol from paper mill effluents by electro coagulation, *J. Env. Manage.*, 87, 420-428.
- Weber W.J. and Morris J.C., (1963), Kinetics of adsorption on carbon from



solution, J. Saint. Eng. Div. Am. Soc. Civil Eng., 89, 31-60.

Xu J.Q., Duan W.H., Zhou X.Z. and Zhou J.Z., (2006), Extraction of phenol in wastewaters with annular centrifugal contactors, J. Hazard. Mater., 131, 98-102.

Yang K., Wu W., Jing Q., Zhu L., (2008), Aqueous adsorption of aniline, phenol, and

their substitutes by multi-walled carbon nanotubes, Environ. Sci. Technol., 42(21), 7931-7936.

Zhu L., Chen B., Shen X., (2000), Sorption of phenol, p-nitrophenol, and aniline to dual-cation organobentonites from water, Environ. Sci. Technol., 34(3), 468-475.

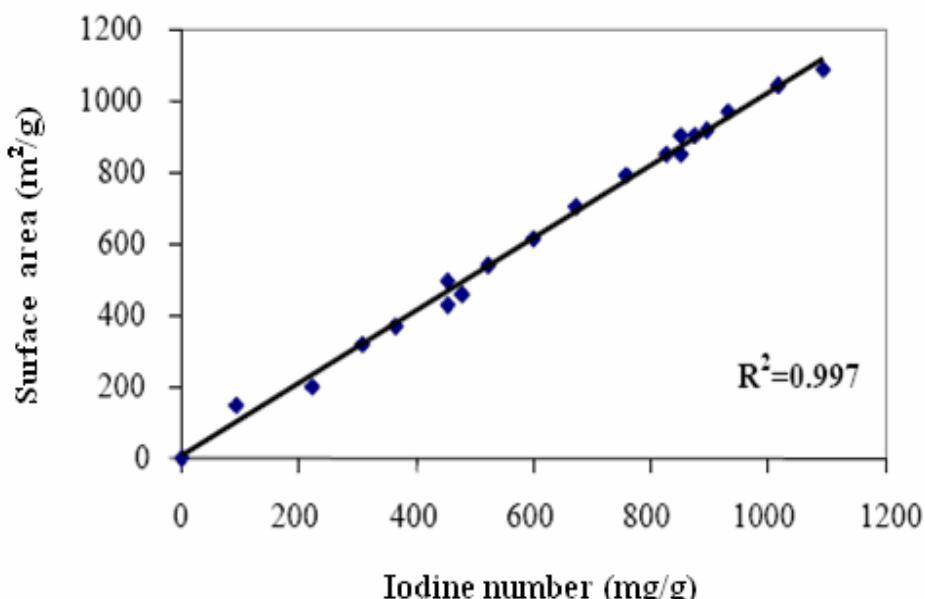
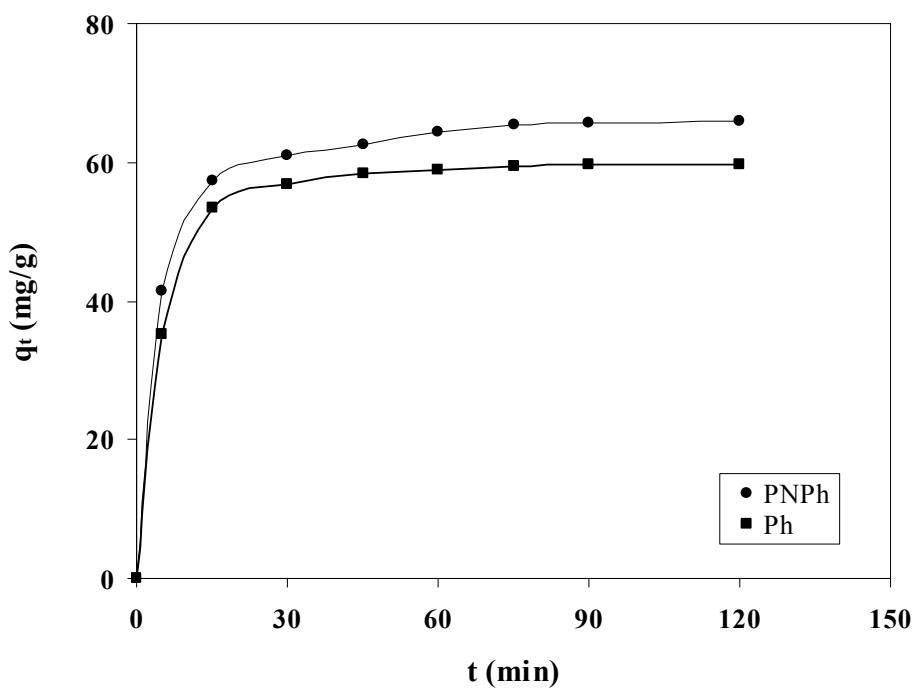
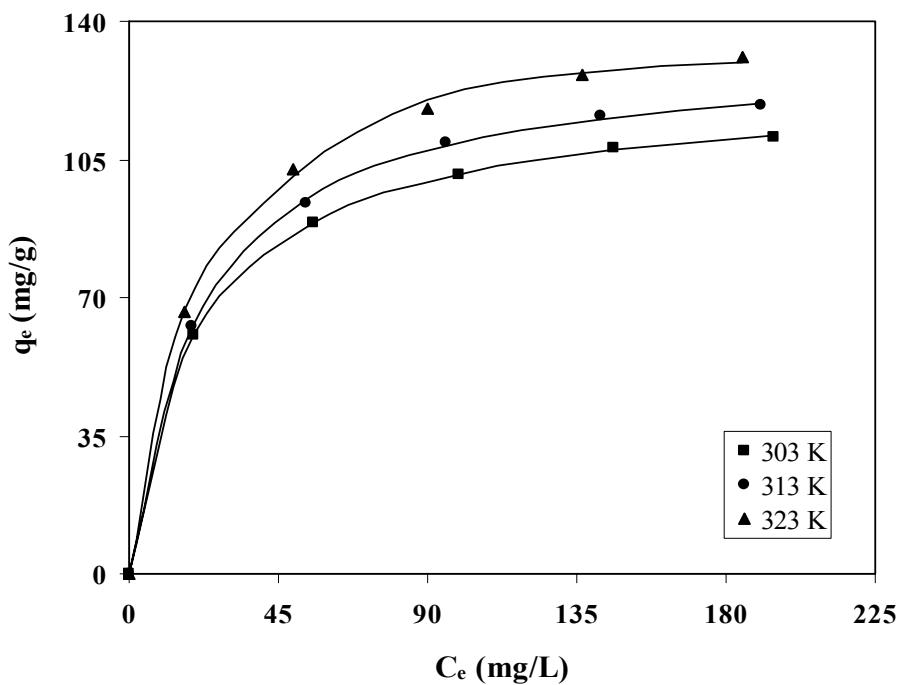


Fig. 1 Estimated surface area calibration curve



**Fig. 2 Effect of contact time on adsorbed amounts of Ph and PNPh on date stones at 303 K**



**Fig. 3 Adsorption isotherm of Ph on date stones correlated**

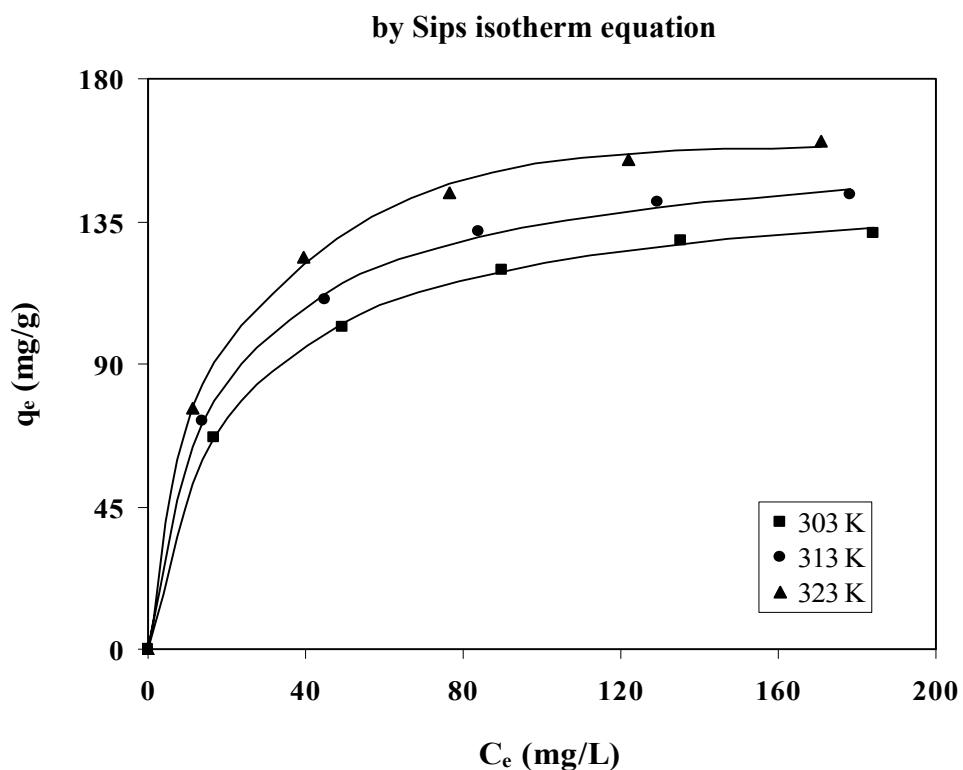


**Fig. 4** Adsorption isotherm of PNPh on date stones correlated by Sips isotherm equation

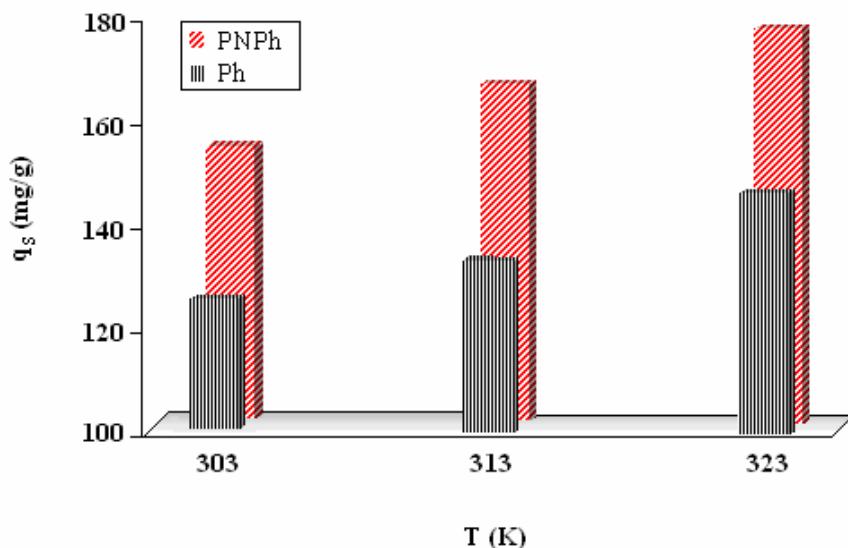


**Fig. 5** Effect of temperature on maximum adsorbed amounts of Ph and PNPh on date stones calculated from Sips isotherm

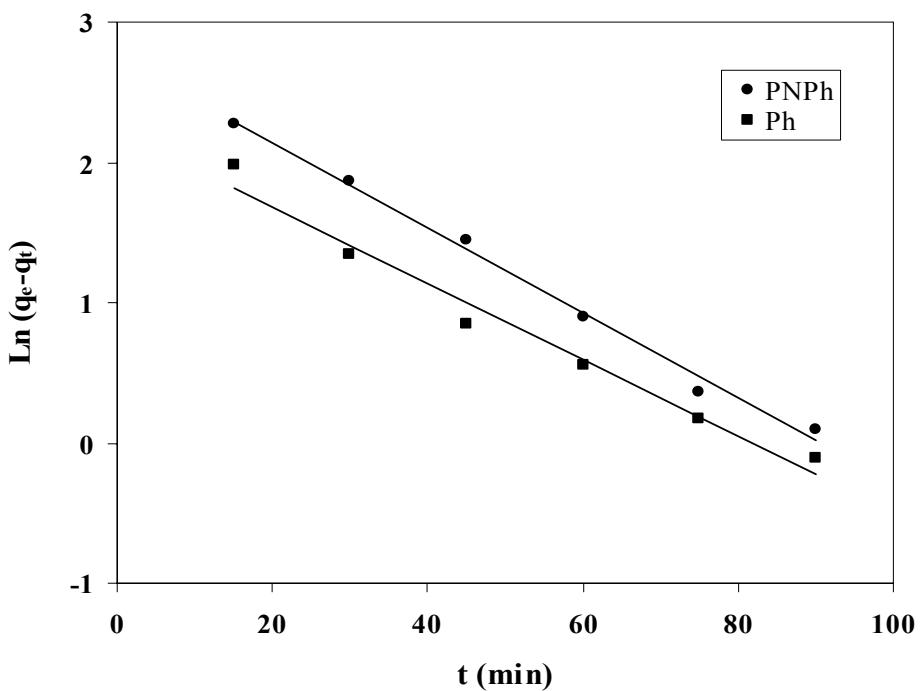


**Fig. 6 Pseudo-first order kinetic for adsorption of Ph and PNPh  
on date stones at 303 K**

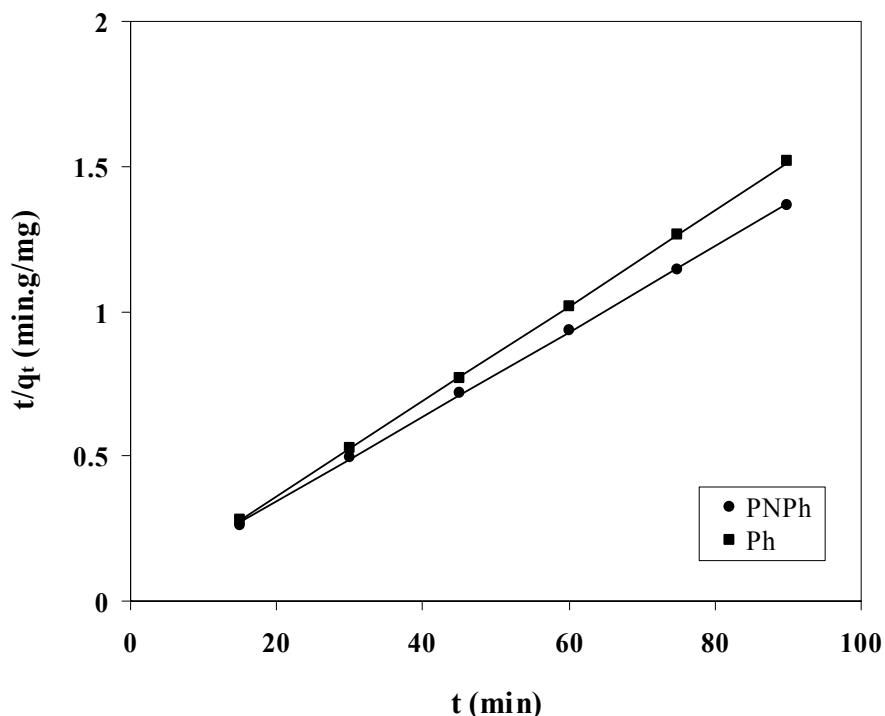


**Fig. 7 Pseudo-second order kinetic for adsorption of Ph and PNPh on date stones at 303 K**

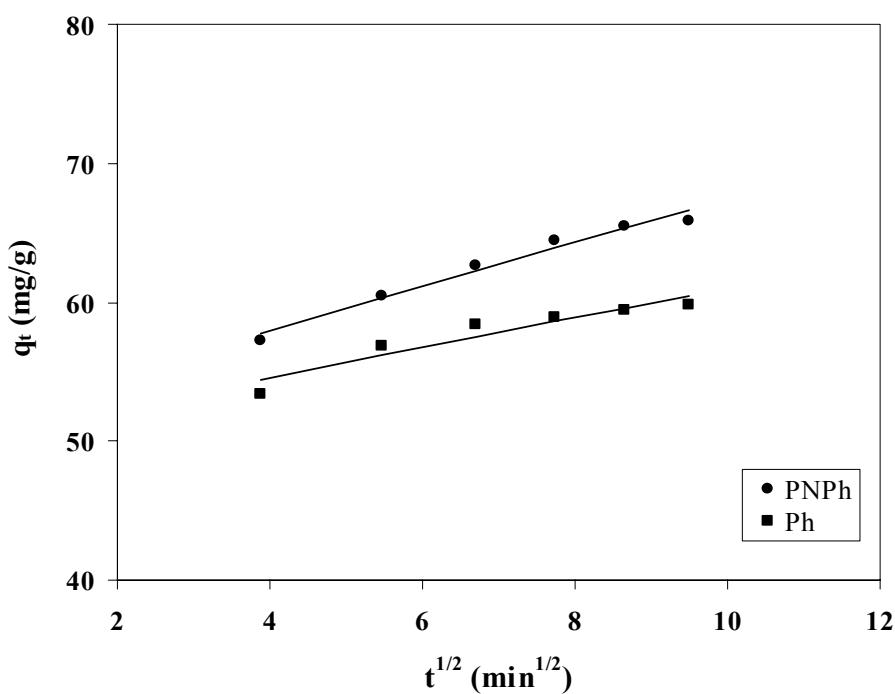


**Fig. 8 Intraparticle diffusion plot for adsorption of Ph and PNPh on date stones at 303 K**

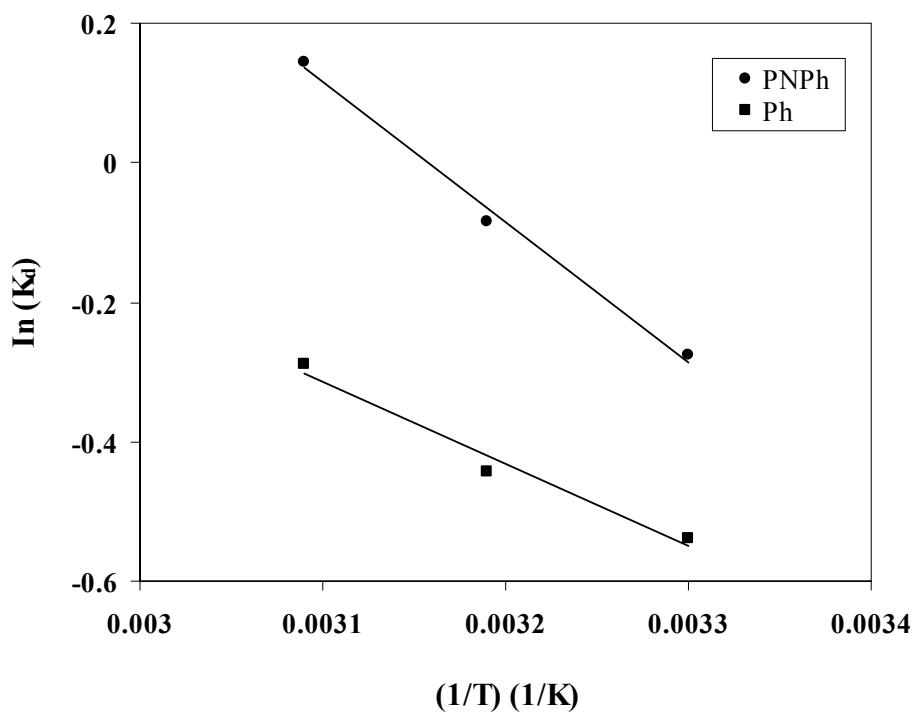


**Fig. 9 Plot of In Kd versus 1/T for 50 mg/L initial Ph and PNPh Concentration**

**Table 1, Properties of chemicals**

Compound	Molecular formula	Purity (%)	Source
Phenol	C <sub>6</sub> H <sub>5</sub> OH	>99	BDH chemicals Ltd company
P-nitro phenol	C <sub>6</sub> H <sub>5</sub> NO <sub>3</sub>	>99	BDH chemicals Ltd company
Hydrochloric Acid	HCl	35-38	Poch S.A. Company
Sodium Thiosulfate	Na <sub>2</sub> O <sub>3</sub> S <sub>2</sub> .5H <sub>2</sub> O	>99	Fluka Chemie AG Company
Iodine	I <sub>2</sub>	99.9	Sigma Aldrich Company

**Table 2, Characteristics of date stones**

Characteristic	Value
Bulk density (g/ml)	0.393
Surface area (m <sup>2</sup> /g)	495.71
Ash content (%)	1.66
Moisture content (%)	7.80
Iodine number (mg/g)	475.88

**Table 3, Adsorption isotherm parameters of Ph and PNPh on date stones**

adsorbate	Temperature (K)	Langmuir isotherm		
		q <sub>m</sub> (mg/g)	K <sub>L</sub> (L/mg)	R <sup>2</sup>
PNPh	303	146.64	0.0489	0.9993
	313	158.36	0.0567	0.9989
	323	173.60	0.0660	0.9987
Ph	303	122.17	0.0494	0.9998
	313	132.37	0.0476	0.9997
	323	144.65	0.0501	0.9991
Freundlich isotherm				
PNPh		K <sub>F</sub> ((mg/g)(L/mg) <sup>1/n</sup> )	n	
		34.865	3.7975	0.9899
		40.290	3.9285	0.9884
Ph		46.773	4.0331	0.9852
		31.539	4.0764	0.9916
		32.402	3.9134	0.9893
		35.422	3.8804	0.9878
Sips isotherm				
PNPh		q <sub>m</sub> (mg/g)	K <sub>S</sub> ((L/mg) <sup>1/m</sup> )	m
		152.66	0.0626	1.1167
		165.50	0.0739	1.1347
Ph		179.62	0.0812	1.1087
		125.26	0.0595	1.0805
		133.43	0.0506	1.0249
		147.09	0.0564	1.0515
				0.9991

**Table 4, Comparison of Ph and PNPh maximum capacity onto various adsorbents**

adsorbate	adsorbent	maximum capacity (mg/g)	Ref.
Ph	date stones	147.09	This study
	red mud	59.20	(Gupta et al., 2004)
	soil	34.27-51.83	(Subramanyam and Das, 2009)
	chitin	25.06	(Dursun and Kalayci, 2005)
	clinoptilolite rock	11.70	(Sprynskyy et al., 2009)
	lignite	10.00	(Polat et al., 2006)
	olive pomace	4-5	(Stasinakis et al., 2008)
PNPh	deoiled soya	1.59	(Mittal et al., 2009)
	date stones	179.62	This study
	wood fly ash	134.90	(Daifullah and Gad, 1998)
	mauritanian clay	43.7 ± 9.8	(Ely et al., 2011)
	mansonia sawdust	21.28	(Ofomaja, 2011)
	Rice husk	15.3	(Ahmaruzzaman and Shama, 2005)
	chitosan	1.98	(Li et al., 2009)
	aliginate	0.69	(Peretz and Cinteza, 2008)



Number 6

Volume 18 June 2012

Journal of Engineering

**Table 5, Kinetic adsorption parameters of Ph and PNPh at 50 mg/L and 303 K**

adsorbate	Pseudo-first order model			
	q <sub>e, exp</sub> (mg/g)	q <sub>e, cal</sub> (mg/g)	K <sub>1</sub> (1/min)	R <sup>2</sup>
PNPh	66.89	3.292	0.0303	0.9935
Ph	60.67	2.624	0.0271	0.9749
Pseudo-second order model				
	q <sub>e, exp</sub> (mg/g)	q <sub>e, cal</sub> (mg/g)	K <sub>2</sub> (g/mg.min)	
PNPh	66.89	68.27	0.0042	0.9998
Ph	60.67	60.89	0.0080	0.9999
Intraparticle diffusion model				
	q <sub>e, exp</sub> (mg/g)	C (mg/g)	K <sub>3</sub> (mg/g.min <sup>1/2</sup> )	
PNPh	66.89	51.68	1.572	0.9722
Ph	60.67	50.18	1.089	0.8969

**Table 6, Thermodynamics adsorption parameters of Ph and PNPh at 50 mg/L**

adsorbate	ΔH (J/mole)	ΔS (J/mole)	-ΔG (J/mole)		
			303 K	313 K	323 K
Ph	10535.30	38.24	1090.79	1347.98	1860.99
PNPh	20277.34	72.71	1770.96	2443.52	3227.88



# مجلة الهندسة

ISSN 1726-4073



مجلة علمية محكمة تصدرها  
كلية الهندسة - جامعة بغداد

حزيران

2012

6

18



# Journal of Engineering

ISSN 1726-4073



A Scientific Refereed Journal  
Published by College of  
Engineering University of  
Baghdad

JUNE  
2012

Number 6  
Volume 18

# ENGINEERING

College of Engineering

Baghdad University

Baghdad

## List of Contents

### English Section:

	Page
<b>Theoretical and Experimental Investigation of Transient Temperature Distribution in Friction Stir Welding of AA 7020-T53</b>  <i>Dr. Muhsin Jaber Jweeg Dr. Moneer Hameed Tolephih Muhammed Abdul-Sattar</i>	<b>693 - 709</b>
<b>Comparative Biosorption Of Pb(II), Cr(III) And Cd(II) Ions In Single Component System By Live And Dead Anaerobic Biomass, Batch Study</b>  <i>Abbas H. Sulaymon Shahlaa E. Ebrahim Mohanad J. Mohammed Ridha</i>	<b>710 - 716</b>
<b>Experimental and numerical evaluation of friction stirs welding of AA 2024-W aluminum alloy</b>  <i>Dr.Ayad M. Takhakh Hamzah N. Shakir</i>	<b>717 - 734</b>
<b>Effects Of Functionalized Polyethylene And Styrene Butadiene Styrene Polymers On Performance Grade Of Local Asphalt Binder</b>  <i>Dr. Alaa H. Abed</i>	<b>735 - 738</b>
<b>Adsorption Of Phenol And P-Nitro Phenol Onto Date Stones: Equilibrium Isotherms, Kinetics and Thermodynamics Studies</b>  <i>Muthanna J. Ahmed, Samar K. Theydan, Abdul-Halim A.K. Mohammed</i>	<b>739 - 757</b>
<b>New Correlation To Calculate Absolute Permeability From Gas Permeameter</b>  <i>Ass. Lecture Dhorgham S. Ibrahim Ass. Lecture Hussein H. Hussein</i>	<b>758 - 767</b>

## قائمة المحتويات

:

**134 - 114**

.

**150 - 135**